Accretion topics in astrophysics

Iván Zalamea

Submitted in partial fulfillment of the
requirements for the degree
of Doctor of Philosophy
in the Graduate School of Arts and Sciences

COLUMBIA UNIVERSITY

2011

ABSTRACT

Accretion topics in astrophysics

Iván Zalamea

Accretion theory is essential for understanding a multitude of varied astronomical observations such as X-ray binaries, active galactic nuclei and gamma-ray bursts. In this document three works on accretion will be presented. The first one is on the structure of an inviscid accretion disc with small angular momentum around a rotating black hole. This regime of accretion may occur in X-ray binaries and GRBs. The second work is on neutrino antineutrino annihilation in the vicinity of a hyper-accreting black hole. This work is relevant for the study of GRBs, in particular it singles out when neutrinos may be responsible for powering GRBs. The third work studies the tidal stripping of a white dwarf spiraling into a massive black hole. The stripped matter accretes onto the black hole producing a transient emission, presumably periodic, observable with X-ray and optical telescopes. At the same time the white dwarf emits gravitational waves as it spirals into the black hole.

Table of Contents

1 Introduction **1**

1.1 Accretion in context 1

1.2 Outline 4

1.3 Basics of accretion 6

1.3.1 Motion of the accreting matter 7

1.3.2 Minimum specific angular momentum for disc accretion 7

1.3.3 Standard viscous accretion disc 9

1.3.4 Emission from the accretion disc 13

1.3.5 Further considerations 16

1.4 Gamma-ray bursts 17

1.4.1 Observations 17

1.4.2 Central engine 21

1.5 Gravitational waves 22

1.5.1 Gravitational radiation from point masses 23

1.5.2 Detection of gravitational waves 23

2 Mini-discs around spinning black holes **27**

2.1 Introduction 27

2.2 Supersonic infall with angular momentum 29

2.2.1 Collision Radius 30

2.2.2 Non-intersection of streamlines above the equatorial plane . . 32

2.3 Disc Dynamics 32
2.4 Disc luminosity 40
2.5 Conclusions 46

3 Neutrino heating near hyper-accreting black holes 47
3.1 Introduction 47
3.2 Model description 49
3.2.1 Neutrino source: disc model 49
3.2.2 Neutrino transport 52
3.2.3 Local rates of $e^{\pm}$ creation 53
3.2.4 Integration of the energy deposition rate over volume 55
3.2.5 Numerical Method 57
3.2.6 Comparison with previous works 58
3.3 Results 59
3.3.1 Energy deposition from $\nu\bar{\nu} \rightarrow e^{+}e^{-}$ 59
3.3.2 Energy deposition from $\nu \rightarrow \nu e^{+}e^{-}$ in a strong magnetic field 62
3.3.3 Scaling of $\dot{E}_{\nu\bar{\nu}}$ and $\dot{E}_{\nu B}$ with $\dot{M}$, M and $r_{\rm ms}$ 66
3.4 Conclusions 70

4 White dwarfs stripped by massive black holes 72
4.1 Introduction 72
4.2 Tidal stripping 75
4.2.1 Onset of mass loss 75
4.2.2 Estimate for mass loss in one orbital period 78
4.2.3 Evolution of mass loss over many orbits 80
4.2.4 Periodic mass-loss rate 81
4.3 Discussion: electromagnetic counterpart 83

Bibliography 87

A Kerr metric and some useful expressions **103**

A.1 Kerr metric 103

A.2 Radial equation of motion for the mini-disc 104

B Calculation of the escaping luminosity **106**

B.1 Angular distribution of emission in the local ZAMO frame 106

B.2 Escape cones 108

C Structure of a cold and non-rotating white dwarf **111**

List of Figures

1.1 Angular momentum distribution in the interior of a pre-supernova. The black curve shows the specific angular momentum as a function of the mass from the center. The initial mass of the star is $16M_{\odot}$ and the equatorial velocity before the collapse was chosen to 390 km s^{-1}. The other three curves show the show angular momentum of the last stable circular orbit for a Schwarzschild black hole, a maximally rotating Kerr black hole, and a black hole with the mass and angular momentum inside a given radius of the massive star (from [Woosley and Heger, 2006]). 10

1.2 Sky distribution of GRBs. The figure shows about a thousand bursts detected by BATSE before 1997 (from [Meegan *et al.*, 1996]). 17

1.3 Distribution of GRB durations. T_{90} is the time in which the detector receives 90% of the total burst energy (from [Meegan *et al.*, 1996]). . 18

1.4 Typical light curve showing the prompt and afterglow emission from GRB 050315 (from [Panaitescu, 2006]). 19

1.5 Shape of the spectrum of the prompt emission from GRBs. The peak of the spectrum is typically in between 0.1 and 1 Mev (from [Briggs *et al.*, 1999]). 20

1.6 The figure shows the cumulative shift of periastron time for pulsar PSR 1913+16 since October 1974. Figure from [Weisberg et al., 2010]. . . 25

1.7 The figure shows the gravitational wave amplitude for which LISA and LIGO are sensitive as a function of the gravitational wave frequency. The shaded regions show different sources that would produce detectable signals. Adapted from http://imagine.gsfc.nasa.gov/ . . . 26

2.1 Fractional difference between the exact $r_\star$ and its approximation (eq. 2.11) as a function of l. The curves start at $l_0 = l_\star$ that corresponds to $r_\star$ at the horizon of the black hole. All curves are plotted for maximally rotating black holes ($a_\star = 1$), when eq. (2.11) is least accurate. 31

2.2 *Upper panel:* solutions for the radial velocity measured by ZAMO (in units of c) of the parabolic infall above the disc and the matter inside the disc. Two cases are shown: $a_\star = 0.6$, $l_0 = 2.1 r_g c$ and $a_\star = 0.95$, $l_0 = 1.56 r_g c$. *Lower panel:* the corresponding azimuthal velocities of the infall and the disc, measured by ZAMO. 37

2.3 Trajectory of disc matter in the critical case $l_0 = 2.14 r_g c$ for a black hole with $a_\star = 0.6$. The insert shows the radial and azimuthal velocities of the disc measured by ZAMO. x and y are the coordinates in the equatorial plane defined by $x = r\cos\phi$, $y = r\sin\phi$. 38

2.4 *Bottom panel:* the range of angular momenta $l_\star(a_\star) < l_0 < l_{\rm cr}(a_\star)$ that lead to the inviscid mini-disc regime (shaded region). Accretion with $l_0 < l_\star$ is quasi-spherical all the way into the black hole; it does not form a caustic outside the horizon. Accretion with $l_0 > l_{\rm cr}$ must proceed through a viscous, centrifugally supported disc. *Top panel:* maximum radius of the mini-disc ($l_0 = l_{\rm cr}$) as a function of the black-hole spin parameter $a_\star$ (solid curve). The radius of the black hole $r_h(a_\star)$ (eq. 2.36) is shown by the dotted curve. 39

2.5 Maximum mass fraction accreted through the inviscid mini-disc. This maximum corresponds to $l_0 = l_{\rm cr}$ and depends on the black-hole spin $a_\star$ (see the text). 40

2.6 Radial distribution of escaping luminosity for discs with $l_0/r_g c = 0.8$, 1.1, and 1.5 around a black hole with spin parameter $a_\star = 0.9$. The luminosity is normalized by the rate of rest-mass accretion through the disc, $\dot{M}(r_h)c^2$. 42

2.7 Radiative efficiency as a function of l_0, ignoring the light capture into the black hole. Seven curves are plotted for black holes with different spin parameters $a_\star$. Solid curves are used for $a_\star \geqslant 0$ and broken curves for $a_\star < 0$. 44

2.8 Same as Fig. 2.7 but taking into account the suppression of radiative efficiency due to light capture into the black hole. 45

3.1 Projection of the sky for three different observers receiving neutrinos from a disc of radius $140r_h$. The colour codes the ratio of the energy at reception to the energy at emission for neutrinos, as measured in the local ZAMO frames (Section 2.4). All three observers are located at 3.1 horizon radii r_h around a black hole of spin $a = 0.95$. Their θ positions are approximately 0, $\pi/4$ and $\pi/2$. The observer sky is parameterized with two angles $\alpha \in (0, \pi)$ and $\beta \in (0, 2\pi)$ in the ZAMO frame. The axis $\alpha = 0$ points into the black hole and $\alpha = \pi$ points away from the black hole. The x and y coordinates in the figure are $(x, y) = (\frac{\alpha}{\pi} \sin\beta, \frac{\alpha}{\pi} \cos\beta)$. 54

3.2 Color-coded and contour plot for $\log_{10} Q^t_{\nu\bar{\nu}}$ around an accretion disc with $\dot{M} = 1M_\odot/s$. The black hole has mass $M = 3M_\odot$ and spin parameter $a = 0.95$. The horizon sphere (black) has the radius $r_h \approx 1.3GM/c^2$, and the inner edge of the disc (the marginally stable orbit) is at $r_{\rm ms} \approx r_g = 2GM/c^2$. Arrows show the projection of $Q^i_{\nu\bar{\nu}}/Q^t_{\nu\bar{\nu}}$ on the plane of the figure. The white curve is where the radial component of injected momentum $Q^r_{\nu\bar{\nu}}$ changes sign. It roughly indicates the region where the deposited energy may be lost into the black hole rather than escape in an outflow. Disc Model A with viscosity parameter $\alpha = 0.1$ (Section 2.1) was used in the calculation. Practically the same $Q^t_{\nu\bar{\nu}}$ is found for Models B and C, and for different α (e.g. $\alpha = 0.01$). 60

3.3 Same as Fig. 3.2 but for a non-rotating black hole, $a = 0$. 61

3.4 $\dot{E}_{\nu\bar{\nu}}$ as a function of $\dot{M}$ for a non-rotating black hole ($a = 0$) and for a rotating black hole ($a = 0.95$) of mass $M = 3M_\odot$. Open symbols show Model A and filled symbols show Model B (Section 2.1). The results of both models are well approximated by simple Model C, which is shown in the figure by lines; the line is dotted at low $\dot{M}$ where the disc is transparent to neutrinos. 63

3.5 Radius of the marginally stable orbit, $r_{\rm ms}$, as a function of the black-hole spin parameter a. 64

3.6 $\dot{E}_{\nu\bar{\nu}}$ and $\dot{E}_{\nu B}$ as functions of $r_{\rm ms}$ for fixed accretion rate, $\dot{M} = 1M_\odot/s$. 65

3.7 Ratio $\dot{E}_{\nu B}/\dot{E}_{\nu\bar{\nu}}$ as a function of $\dot{M}$ for $a = 0$ and $a = 0.95$. The accretion disc is assumed to have viscosity parameter $\alpha = 0.1$. 67

3.8 Same as Fig. 3.4 but now including the contribution of reaction $\nu \to \nu e^+ e^-$. This contribution $\dot{E}_{\nu B}$ is shown only at $\dot{M} < \dot{M}_{\rm ign}$, where it is important; $\dot{E}_{\nu B}$ is small compared with $\dot{E}_{\nu\bar{\nu}}$ at $\dot{M} > \dot{M}_{\rm ign}$ (cf. Fig. 3.7). 68

4.1 Radius r_0 where tidal stripping begins, in units of the Schwarzschild radius $r_g \equiv 2GM_{\rm BH}/c^2 \approx 3{\times}10^{10}(M_{\rm BH}/10^5 M_\odot)$ cm, is shown as a function of the WD mass. The three curves correspond to $M_{\rm BH}/10^5 M_\odot = 0.5$, 1 and 5. The value of r_0 was estimated using the simplified equation (4.6), which is non-relativistic and neglects the effect of the black-hole spin a_s on the tidal force. The shaded region shows radii $r < r_{\rm min}$ where no stable bound orbits exist. $r_{\rm min}$ depends on a_s and orbital eccentricity e, in particular $r_{\rm min} = 3r_g$ for $\{a_s = 0, e = 0\}$, $r_{\rm min} = 2r_g$ for $\{a_s = 0, e = 1\}$ and $r_{\rm min} = r_g/2$ for $\{a_s = 1, e = 1\}$. 77

4.2 Lost mass fraction $x = (M_0 - M)/M_0$ after N orbits since the onset of tidal stripping. The WD has initial mass $M_0 = 0.6M_\odot$. Different curves correspond to different eccentricities of the orbit; $M_{\rm BH} = 10^5 M_\odot$ is assumed for all cases. The insert shows $\log x$ plotted against $\log N$. 82

4.3 Instantaneous mass-loss rate $\dot{M} = |dM/dt|$ during the last 35 orbits before disruption. The WD with initial mass $M_0 = 0.6M_\odot$ is orbiting a black hole with $M_{\rm BH} = 10^5 M_\odot$; the orbit has eccentricity $e = 0.9$. The horizontal axis shows 'time during mass transfer', which increases only when $\dot{M} \neq 0$. The area under each peak is the mass lost per pericenter passage; it follows a power law with the number of orbits left to complete disruption, $\delta M \propto (N_\star - N)^{-1.8}$, close to the results of Section 2.3. 84

B.1 Escape cones $S_{\rm esc}$ on the ZAMO sky. The photon direction $\bar{\mathbf{\Omega}}$ is specified by two angles α and φ (eqs. B.8-B.10). The figure uses polar coordinates (ρ, ϕ) with $\rho = \alpha/\pi$ to represent all possible photon directions. The origin of the diagram $\rho = 0$ corresponds to the radial direction away from the black hole (such photons always escape) and the unit circle $\rho = 1$ (thick black curve) corresponds to the radial direction into the black hole (such photons are captured). The colour curves show the boundary of the escape cone for five emission radii; the emission radius is indicated next to the curves, in units of the horizon radius r_h. The figure presents four such diagrams calculated for black holes with spin parameter $a_\star = 0$, 0.6, 0.9, and 0.998. 110

C.1 Mass-radius relationship for cold white dwarf. 112

List of Tables

3.1 Fractional change of the energy deposition rate when the grid resolution is reduced from 500 to 240 points (left column), and when the number of geodesics is increased from 5×10^3 to 10^4 (right column). 58

Acknowledgments

The work here presented would not have reached its state if it was not for the unprecedented guidance I received from Andrei M. Beloborodov. I am grateful to him for all the long hours he dutifully devoted to my training. I am greatly indebted to Kristen Menou for his unparalleled advice which transcends the domain of instruction.

I thank the Physics and Astronomy departments at Columbia University for all the support received. I am grateful to all staff members of the Physics and Astronomy departments for the unmeasurable help they provided. In particular I thank Lalla Grimes for her always kind and efficient help involving administrative matters.

I thank Fabio Dominguez for carefully reading part of this manuscript and providing comments that helped improve it.

I thank Ximena Fernández for her constant encouragement and support which made the last years of my graduate studies much more enjoyable. I also thank her for providing comments on the manuscript that helped improve it.

I feel exceptional gratitude for Ethna, Eduardo, Camilo, Maria Eugenia, Gerardo, Ricardo and Susan, who kept me on firm land at times when I saw swamp around me.

To my parents

Chapter 1

Introduction

1.1 Accretion in context

Accretion, understood as agglomeration of matter under the action of gravity, takes a central role in the history of the universe. Under the cohesive action of gravity, primordial density perturbations, in an initially quasi-homogeneous and hot universe, gave rise to the granular appearance of the visible cosmos [Peebles, 1993]. The occurrence of accretion did not stop after the universe got its hierarchical structure of stars assembled in galaxies and galaxies assembled in groups of galaxies. Accretion through a disc onto a massive central object is an essential aspect in the present understanding of protoplanetary discs (e.g. see [Armitage, 2010]), close binaries (see [Done *et al.*, 2007] for a review on X-ray binaries, and [Kato *et al.*, 2008] for a discussion on cataclysmic variables), gamma-ray bursts (GRBs; see [Piran, 1999], [Piran, 2004] and [Mészáros, 2006] for reviews) and active galactic nuclei (e.g. see [Krolik, 1999]).

Most of the astrophysical applications of accretion theory involve accretion discs around a central massive object. A large number of different models have been constructed over the years (see the book [Kato *et al.*, 2008] for an extensive review). Most of the initial development was based on two types of discs, one optically thick and slim ([Shakura and Sunyaev, 1973]), and the other optically thin and geometri-

cally thick ([Thorne and Price, 1975], [Shapiro and Lightman, 1976]). The optically thin model predicts a much higher temperature in the inner region of the disc than the one predicted by the optically thick model, and it is able to explain observation of hard X-rays from sources like Cygnus X-1. Later theory developments came from relaxing two assumptions made in the initial models. One assumption was to require Keplerian rotation of the disc in its inner region. The second assumption was to ignore advection of energy by the disc. The transonic motion of the disc in its inner regions impedes Keplerian rotation, this was first recognized by [Liang and Thompson, 1980] and [Abramowicz and Zurek, 1981]. In the seminal work of [Abramowicz *et al.*, 1988], an optically thick advection dominated disc model was introduced. These discs are characterized by accretion rates close to the Eddington accretion rate, and their pressure is dominated by radiation. An influential model of an advection dominated optically thin disc was introduced by [Narayan and Yi, 1994]. The model was later applied to explain the spectrum of Sagittarius A* [Narayan *et al.*, 1995]. Two-temperature advection dominated models have been also constructed (see[Narayan and Yi, 1995], [Nakamura *et al.*, 1996], [Nakamura *et al.*, 1997], [Manmoto *et al.*, 1997]). As in the case of [Shapiro and Lightman, 1976], two-temperature advection dominated discs were constructed to explain the high energy part of the spectra observed in active galactic nuclei. Later theory developments included reprocessing of the X-ray emission from the inner region of an accretion disc by its outer regions. See [Beloborodov, 1999] for a review of several disc models including ones with feedback from X-ray reprocessing.

Boundary conditions at the inner edge of the disc is an issue usually debated. In particular, how much torque is applied to the disc at its inner edge, has recently attracted attention (see [Agol and Krolik, 2000], [Afshordi and Paczyński, 2003], [Shafee *et al.*, 2008]). In recent years the debate has concentrated on finding the importance, on the overall structure of the disc, of magnetic stress at the inner edge of the disc. In the past the debate focused on the existence or not of a hard surface

at the inner edge of the disc. The adequate fit of observations by accretion models with black holes as the accretor, is an indirect proof of the existence of black holes ([Narayan *et al.*, 1996]).

Accretion discs models are known to have several instabilities. Pioneering work by [Lightman and Eardley, 1974] showed that the standard accretion discs are prone to fragment in their inner regions, where the pressure is dominated by radiation (see also [Shakura and Sunyaev, 1976]). This instability to density perturbations is known as the secular instability or viscous instability. The inner regions of a standard accretion disc are also unstable to temperature perturbations [Pringle, 1976]. The existence of these instabilities have been proposed as explanations for the time variability observed X-ray stars and AGN (see [Kato *et al.*, 2008] for a general review of accretion disc instabilities). The role of disc instabilities on the transition between different accretion disc models (different spectral states) is an interesting open question.

Quasi-periodic oscillations, QPOs, are flickerings on the X-ray flux emitted by an astronomical object. QPOs with frequencies centered around a few Hz were discovered by [Middleditch and Priedhorsky, 1986] and [van der Klis *et al.*, 1985]. QPOs with frequencies centered around kHz have been also observed [van der Klis *et al.*, 1996]. The relation between accretion discs and QPOs is a topic of current research (see [Abramowicz, 2005]). There have been attempts to link QPOs with waves propagating on an accretion disc [Kato, 2001]. Recently, emission from the hot spots of an accreting magnetized neutron star has been proposed as a mechanism for kHz QPOs [Bachetti *et al.*, 2010].

The study of astrophysical jets is an area of current research where accretion theory takes a leading role (see [Belloni, 2010] for a compilation of recent review articles). Active galactic nuclei exhibit jets usually observed in radio (e.g. see [Bridle and Perley, 1984]) although emission in frequencies up to gamma-rays is also observed. The jets originate from a very small region compared to the size of the host galaxy. This is implied by a time variability of a few minutes (see [Begelman *et al.*, 1984]

for a review). Jets are also observed around black-hole X-ray binaries (see [Mirabel and Rodríguez, 1999] and [Fender *et al.*, 2004]). Despite the very different scales associated with AGN jets and X-ray binary jets, they are currently understood as the result of accretion onto a black hole. Accretion onto a supermassive black hole in the case of AGNs, and accretion onto a solar mass black hole in the case of X-ray binaries. Another astrophysical situation were jets take an important role are GRBs. In these case the existence of an ultra-relativistic jet is required by theory (e.g. [Piran, 2004]). The formation and stability of the jets in all these astrophysical processes are topics of current research. The importance of magnetic fields in the formation and stability of jets has been recognized as essential (see [Blandford and Payne, 1982] for a seminal work. [McKinney and Blandford, 2009] deals on the stability of magnetized jets).

1.2 Outline

In chapters 2, 3 and 4 of this document I present three works that, although are independent of each other, all involve astrophysical processes in the vicinity of a black hole with accretion as a common feature. A summary for each one of those works follows.

Some of the most luminous astrophysical objects are associated with accreting black holes [Shakura and Sunyaev, 1973]. The amount of angular momentum of the in-falling matter determines if the accretion occurs radially or through a disc. The two extreme cases, classically known as Bondi accretion and Shakura-Sunyaev accretion, have been extensively studied. The first of the three works I will present is a scenario in between these two classical regimes. We studied inviscid accretion with just enough angular momentum to marginally form a disc around a rotating black hole ([Zalamea and Beloborodov, 2009], this work is presented in chapter 2). This regime may occur in X-ray binaries [Beloborodov and Illarionov, 2001] or in collapsing stars [Beloborodov, 2008]. We find that a small-scale disc forms for in-falls

with specific angular momentum of the order of $l_0 \approx r_g c$, where $r_g = 2GM/c^2$ is the Schwarzschild radius of the black hole. These discs are radiatively efficient, they emit up to a 10% of the rest-mass energy of the accreting matter. Interestingly, a hydrodynamical analog of the Penrose process occurs when the in-fall accretes with angular momentum opposite to the angular momentum of the black hole.

The second work, presented in chapter 3, considers a hyper-accreting disc around a black hole formed after the merger of binary neutron stars or the collapse of a rotating massive star (collapsar) [Woosley, 1993]. Such a disc emits vast numbers of neutrinos and antineutrinos (see [Narayan *et al.*, 1992], [Popham *et al.*, 1999], [Chen and Beloborodov, 2007], and references therein). Some of them annihilate into relativistic electrons and positrons that may ultimately be responsible for creating an outflow of matter and radiation from the disc. Additionally, neutrinos can create electron-positron pairs by scattering off a strong magnetic field, this channel is important at low mass accretion rates. Including important general relativistic effects, such as geodesic propagation of neutrinos and the structure of the accretion disc in Kerr space-time, I calculated $\dot{E}_{\nu\bar{\nu}}$, the energy per unit time that neutrino annihilation deposits into the electron-positron plasma [Zalamea and Beloborodov, 2011]. $\dot{E}_{\nu\bar{\nu}}$ turned out to be a strong function of the mass accretion rate through the disc, the angular momentum of the black hole and the mass of the black hole. Neutrinos deposit more than 10^{51} erg s^{-1} around the disc, for certain range of mass accretion rates and angular momenta of the black hole. This power is comparable to the luminosities observed from gamma-ray burst explosions.

In the third work, presented in chapter 4, it is found that a white dwarf spiraling into a massive black hole gets its outer layers peeled off like the layers of an onion [Zalamea *et al.*, 2010]. Contrary to the usual tidal disruption of a star, a white dwarf that spirals into a black hole due to gravitational radiation approaches the tidal disruption radius very gently. The fractional change in periastron per orbit is of the order of $\Delta r_p/r_p \approx 10^{-5}$. The white dwarf loses first its outer layers where the matter

density is much smaller than its average density. This combination of small numbers ensures that the white dwarf goes around the black hole loosing mass for thousands of orbits before it gets disrupted. Before and while the peeling is happening, this system radiates gravitational waves detectable with the Laser Interferometer Space Antenna (LISA). We predict that the mass lost by the white dwarf accretes into the black hole and emits a transient electromagnetic signal, presumably periodic, observable with X-ray and optical telescopes. The Large Synoptic Survey Telescope (LSST) will be able to resolve the time variability of the expected optical signal. The estimated X-ray luminosities are detectable by present day X-ray telescopes.

The remainder of this chapter gives an introduction to the general subjects on which the previous three works stand.

1.3 Basics of accretion

An outstanding problem for physicists has been to explain the large power emitted by some astronomical objects. It was not until the discovery of nuclear fusion that we understood how the Sun is able to shine at a rate of a few times 10^{33} erg s^{-1} for billions of years. In this context, understanding the huge luminosity of X-ray binaries ($\simeq 10^{36}$ erg s^{-1}), active galactic nuclei ($\simeq 10^{45}$ erg s^{-1}) or gamma-ray bursts ($\simeq 10^{52}$ erg s^{-1}) poses a serious challenge. Flow of matter into the deep gravitational well of a black hole or a compact star may be a source of extremely large luminosities. A body of mass m that approaches a black hole of mass M_{BH} from far away experiences a gravitational energy change of about

$$\Delta E \simeq \frac{GM_{BH}m}{r} = \frac{mc^2}{2}\frac{r_g}{r}. \tag{1.1}$$

This energy change is comparable to the body's rest-mass if the approaching radius r is a few Schwarzschild radii, $r_g \equiv 2GM_{BH}/c^2$. As will be described next, accretion of matter into a compact star or a black hole is an efficient mechanism for tapping gravitational energy into light or neutrinos.

1.3.1 Motion of the accreting matter

The dynamics of fluid in a gravitational field of metric $g^{\mu\nu}$ is determined by (e.g.[Landau and Lifshitz, 1971])

$$\frac{1}{\sqrt{-g}}\partial_\mu(\sqrt{-g}\rho u^\mu) = 0, \tag{1.2}$$

$$\frac{1}{\sqrt{-g}}\partial_\mu(\sqrt{-g}T^\mu_\nu) = \frac{1}{2}\frac{\partial g_{\alpha\beta}}{\partial x^\nu}T^{\alpha\beta}. \tag{1.3}$$

where ρ and u^μ are the fluid density and 4-velocity. $T^{\mu\nu}$ is the relevant energy momentum tensor. The determinant of the metric is $g \equiv \det[g_{\mu\nu}]$. Equations 1.2 and 1.3 state conservation of baryonic mass and conservation of energy and momentum.

For a classical viscous fluid, in the limit of Newtonian gravity for a central mass M_{BH}, the hydrodynamical equations (corresponding to equations 1.2 and 1.3) are

$$\frac{\partial \rho}{\partial t} + \nabla \cdot (\rho \mathbf{u}) = 0, \tag{1.4}$$

$$\frac{\partial \mathbf{u}}{\partial t} + (\mathbf{u}\cdot\nabla)\mathbf{u} = -\frac{GM_{BH}}{r^2} - \frac{1}{\rho}\nabla p + \nu\nabla^2\mathbf{u}, \tag{1.5}$$

$$\rho\frac{\partial \epsilon}{\partial t} + \rho(\mathbf{u}\cdot\nabla)\epsilon + p\nabla\cdot\mathbf{u} = \dot{\mathcal{Q}}, \tag{1.6}$$

where $\mathbf{u}$ is the velocity field, p is the pressure, ν is the coefficient of kinematic viscosity (treated as cosntant), ϵ is the internal energy of the fluid per unit mass, and $\dot{\mathcal{Q}}$ is the power per unit volume either gained or lost by the fluid. Equations 1.4, 1.5 and 1.6 express conservation of mass, momentum, and energy.

1.3.2 Minimum specific angular momentum for disc accretion

For an accretion disc to form, the accreting matter is required to have a minimum amount of specific angular momentum, estimated by $l_{\min} \approx r_* u_*$, where r_* is the radius of inner boundary of the accretion flow and u_* is the required velocity for a circular orbit at that radius. If the accreting object is a star, r_* is typically the radius of the star and $u_* = \sqrt{GM/r_*}$, where M is the mass of the central object. If the

accreting object is a black hole, r_* is comparable to the gravitational radius of the black hole $r_g \equiv 2GM/c^2$, and u_* is comparable to the speed of light c.

In the case of wind-fed X-ray binaries and collapsars the specific angular momentum of the accreting flow may be comparable to $l_{\min}$. These cases are of special interest for us in view of the work presented in chapter 2.

1.3.2.1 Wind-fed X-ray binaries

In this section we follow closely the discussion in [Frank *et al.*, 1992]. Early type (O or B) stars expel fast stellar winds with velocities of the order of their escape velocity, i.e.,

$$v_W \sim \lambda \left(\frac{2GM_E}{R_E} \right)^{1/2}. \tag{1.7}$$

where M_E is the mass of the early type star, R_E its radius and λ a factor of order unity. A compact object orbiting around an early type star accretes from the wind of the early type star. This systems are known as wind-fed X-ray binaries. The compact object, either a neutron star or a black hole, will only capture wind material that is inside a cylinder around the star and with axis along the direction of motion of the wind as seen from the compact object. The condition for the wind to be captured is that the gravitational potential energy should be smaller than kinetic energy of the wind. The radius of the cylinder is then

$$r_{\rm acc} \approx \frac{2GM}{v_W^2}, \tag{1.8}$$

where M is the mass of the compact object. The average angular momentum of the accreting matter is $l = r_{\rm acc}^2 \Omega/4$ [Illarionov and Sunyaev, 1975], where Ω is the angular velocity of the compact object around the early type star.

For typical values, $v_W \approx 10^8$ cm s^{-1}, $r_{\rm acc} \approx 10^{11}$ cm and $P = 2\pi/\Omega \approx$ 1–5 days [Beloborodov and Illarionov, 2001], the ratio

$$\frac{l}{r_g c} = 1.5 \left(\frac{1 \text{ day}}{P} \right) \left(\frac{M}{M_\odot} \right) \left(\frac{10^8 \text{cm s}^{-1}}{v_W} \right)^4 \tag{1.9}$$

is close to unity. In chapter 2 we present an accretion disc with angular momentum comparable to $r_g c$.

Numerical studies have shown that compact objects accreting from a wind, present flows that change with time the sign of the average angular momentum of the accreting matter (e.g. see [Ishii *et al.*, 1993] and [Livio *et al.*, 1991]). These phenomena, known as the flip-flop instability, is another example of accretion flows with just marginal angular momentum to form a disc.

1.3.2.2 Collapsar model

The collapsar model [Woosley, 1993] proposes the collapse of a massive star as the initial scenario for GRBs and supernovae. The formation or not of an accretion disc strongly depends on the distribution of angular momentum in the interior of the collapsing star. Figure 1.1 (from [Woosley and Heger, 2006]) shows the distribution of angular momentum in the interior of a massive star. The black curve presents the result of their calculations. The red curve shows the angular momentum of the inner most stable circular orbit around a black hole with the mass and angular momentum inside a given radius of the massive star. The point where the red and black curves cross, marks the transition from almost spherical accretion to disc accretion. For the model showed in Figure 1.1 this happens at about $3.5 M_{\odot}$. A short lived mini-disc may form around the transition from spherical to disc accretion.

1.3.3 Standard viscous accretion disc

A canonical solution for equations 1.4, 1.5 and 1.6 is the case of a steady, axisymmetric accretion disc [Shakura and Sunyaev, 1973]. The rotation of the disc material is almost Keplerian with $l \gg l_{\rm min}$. The radial velocity of the matter in the disc is proportional to the kinematic viscosity, and it is assumed to be much smaller than the azimuthal velocity. There is almost no motion in the direction perpendicular to the disc, and hydrostatic balance between the gravitational tidal field of the central object and the

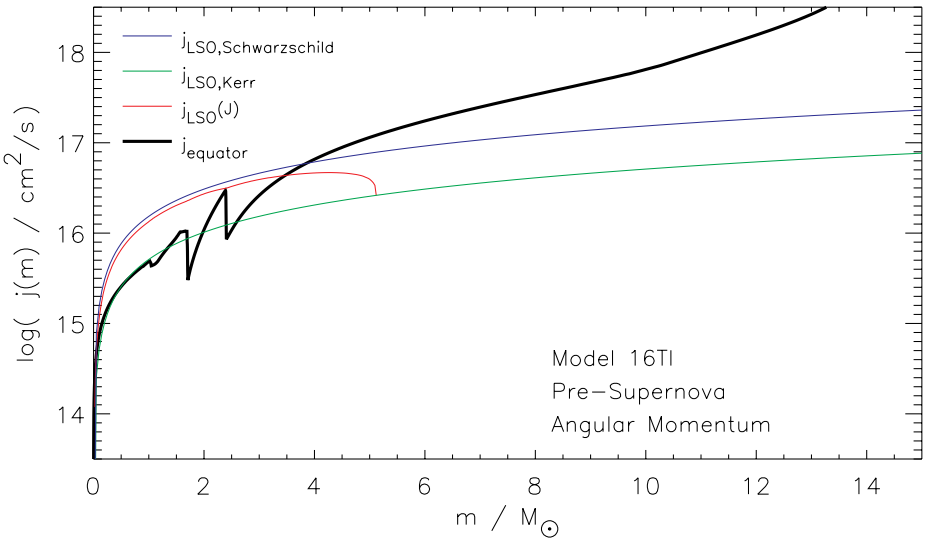

Figure 1.1: Angular momentum distribution in the interior of a pre-supernova. The black curve shows the specific angular momentum as a function of the mass from the center. The initial mass of the star is $16M_{\odot}$ and the equatorial velocity before the collapse was chosen to 390 km s^{-1}. The other three curves show the show angular momentum of the last stable circular orbit for a Schwarzschild black hole, a maximally rotating Kerr black hole, and a black hole with the mass and angular momentum inside a given radius of the massive star (from [Woosley and Heger, 2006]).

pressure in the disc is established.

1.3.3.1 Viscosity and its origin

Viscosity is needed for this accretion picture to work. Keplerian motion of concentric rings implies that the accreting matter steadily loses angular momentum as it makes its way inwards. Angular momentum transport by microscopic collisions of particles (molecular viscosity) is too small to drive the accretion. Two other mechanisms can transport angular momentum more efficiently, turbulent motion and magnetic stresses [Shakura and Sunyaev, 1973].

The origin of turbulent motions in the context of weakly magnetized accretion discs was first developed in [Balbus and Hawley, 1991] (see [Balbus and Hawley, 1998] for a review). These authors recognized that for a differentially rotating disc, linear perturbations grow at a rate of the order of Ω, the angular velocity of the flow. This instability, known as magnetorotational instability (MRI), occurs if

$$\frac{d\Omega^2}{d\ln r} < 0. \tag{1.10}$$

This condition is satisfied by a disc in Keplerian rotation, and independent of the smallness of the initial seed magnetic field. Linear perturbations grow by a factor of $\exp(\Omega T) = 535.5$ per orbit. Numerical simulations have shown that electrical resistivity, η, can hinder the ability of MRI to transport angular momentum [Fleming *et al.*, 2000]. These authors found that MRI effectively transports angular momentum across the radial direction of the disc if

$$\eta \lesssim 10^{-4} c_s H \tag{1.11}$$

where H and c_s are the scale height of the disc, and the sound speed on the disc.

The kinematic viscosity from turbulence is $\nu = v_t \times l$, where v_t and l are the typical velocity and length scales of the largest turbulent structures, eddies. It is expected that $l \leq H$, where H is the scale-height of the disc. Hydrostatic balance

implies $H/r \simeq v_s/u_\phi$, where r is the radial position on the disc and v_s is the sound speed. The rate of angular momentum transfer from neighboring rings is then

$$w_{r\phi} \sim \rho v_t l r \frac{d}{dr}\left(\frac{u_\phi}{r}\right) \sim \rho v_s^2 \frac{v_t}{v_s}, \tag{1.12}$$

where Keplerian rotation is assumed. The turbulent velocity is expected to be subsonic, i.e. $v_t/v_s \leqslant 1$. Magnetic transport of angular momentum along the radial direction is estimated as

$$w_{r\phi} \sim \frac{B_r \times B_\phi}{4\pi} \sim \rho v_s^2 \frac{E_B}{E_{th}}, \tag{1.13}$$

where E_B/E_{th} is the ratio of magnetic energy density to thermal energy density. From the equipartition principle, this ratio is expected to be smaller than one. Following this line of thought, [Shakura and Sunyaev, 1973] parametrized kinematic viscosity as

$$\nu = \alpha v_s H \qquad \text{with} \quad \alpha \leqslant 1. \tag{1.14}$$

1.3.3.2 Energetics of the disc

The standard accretion disc theory predicts that due to the viscosity, the accreting matter receives heat per unit area at a rate of (see [Pringle, 1981] for a review)

$$\dot{q} = \frac{3GM_{BH}\dot{M}}{4\pi r^3}\left(1 - \sqrt{\frac{r_\star}{r}}\right), \tag{1.15}$$

where $\dot{M}$ is the steady (and hence radius independent) mass flow rate through the disc. The radius $r_\star$ denotes the inner edge of the disc. In the case of an accreting black hole, $r_\star$ would be the innermost stable circular orbit (ISCO). The total power transferred to the accreting matter (assuming Newtonian gravity) is

$$\dot{Q} = \int_{r_\star}^{\infty} 2\pi r \dot{q} dr = \frac{1}{2}\frac{GM_{BH}\dot{M}}{r_\star}. \tag{1.16}$$

One can push this result to get an estimate of how much heat is given to the accreting matter if the central object is a black hole. For a Schwarzschild black hole, $r_\star =$

$6GM_{BH}/c^2$. For a maximally rotating Kerr black hole the ISCO extends down to its horizon, $r_\star = GM_{BH}/c^2$. In this two cases we get,

$$\dot{Q} = \frac{1}{12}\dot{M}c^2 \qquad \text{and} \qquad \dot{Q} = \frac{1}{2}\dot{M}c^2. \tag{1.17}$$

These powers are comparable to the rest-mass energy per unit time accreted by the black hole. Instead of 1/12 and 1/2, the exact coefficients in equation 1.17 are 0.057 and 0.42, respectively.

1.3.4 Emission from the accretion disc

Accretion discs efficiently tap gravitational energy into thermal energy. The spectrum of the radiation emitted by the disc is determined by the momentum distribution functions of the emitting particles, mainly electrons but also ions, and by the diffusion of photons along the perpendicular direction of the disc.

1.3.4.1 Blackbody emission

A simple case one can imagine is a steady, optically thick and geometrically thin disc where different species of particles achieve thermal equilibrium, and the disc radiates as much power as heat is viscously dissipated per unit time. In such a case the disc emits a blackbody spectrum[1]. We can find the temperature of the blackbody radiation by equating Stefan-Boltzman formula to $\dot{q}/2$ (assuming the disc emits symmetrically on both sides),

$$T_s = \left[\frac{3GM_{BH}\dot{M}}{8\pi\sigma r^3}\left(1 - \sqrt{\frac{r_\star}{r}}\right)\right]^{1/4} \tag{1.18}$$

where σ is Stefan-Boltzman constant. For $M_{BH} = 10M_\odot$ and $\dot{M} = 10^{18}$ g s^{-1}, the disc's surface temperature T_s peaks at about 4×10^6 K, which corresponds to soft X-ray emission.

[1]See [Shimura and Takahara, 1993] and [Davis and Hubeny, 2006] for more accurate spectral models.

1.3.4.2 Two temperature disc models

A famous X-ray source where accretion theory has been successfully applied is Cygnus X-1. The spectrum of the emitted radiation involves detailed microphysics. One of the many papers on Cygnus X-1 that illustrates the complexities of the spectrum formation is [Shapiro *et al.*, 1976]. In this work the authors present a steady state disc model where the inner region of the disc is optically thin to radiation. In this region, electrons and ions do not share the same temperature. The outer part of the disc is in thermal equilibrium and emits as a blackbody with temperature given by 1.18. Hot electrons in the inner part of the disc Compton scatter the photons emitted by the colder outer region of the disc. These up-scattered photons form the X-ray part of the observed spectrum.

Although the work [Shapiro *et al.*, 1976] was ground breaking, it was found thermally unstable [Piran, 1978] and was superseded by solutions where advection of the energy released by viscosity is important, e.g. [Esin *et al.*, 1998]. The luminosity of the disc is highly suppressed when the diffusion time for photons across the vertical direction of the disc is much larger than the accretion time. In such a case a large fraction of the viscous heat is advected by the accreting matter [Abramowicz *et al.*, 1988]. A similar regime occurs when the disc is optically thin but unable to radiate its heat on the accretion time-scale. This regime of accretion has been applied to X-ray binaries and galactic nuclei. (See [Narayan *et al.*, 1998] and [Narayan and McClintock, 2008] for reviews).

1.3.4.3 Neutrino cooled discs

In some cases the emitted radiation is not even of electromagnetic nature. It has been theorized that during the collapse of a Wolf–Rayet star an accretion disc forms with accretion rates of 0.1—$1 M_{\odot}/\mathrm{s}$ [Woosley, 1993]. In the inner region of such a disc, electron temperatures are higher than $(m_n - m_p)c^2/k_B$ and neutrino emission is

energetically possible via

$$e^- + p \rightarrow n + \nu_e \quad \text{and} \quad e^+ + n \rightarrow p + \bar{\nu}_e. \tag{1.19}$$

Neutrino emitting discs are constructed in a similar way as the discs discussed above, except that the cooling physics is modified (see [Narayan *et al.*, 1992], [Popham *et al.*, 1999], [Chen and Beloborodov, 2007], see [Beloborodov, 2008] for a review). One must take into account lepton number conservation and the transport properties of neutrinos. Lepton number conservation is expressed by (see [Chen and Beloborodov, 2007])

$$\frac{1}{H}\left(\dot{N}_{\bar{\nu}} - \dot{N}_{\nu}\right) = u^r \left[\frac{\rho}{m_p}\frac{dY_e}{dr} + \frac{d}{dr}(n_\nu - n_{\bar{\nu}})\right], \tag{1.20}$$

where H is the scale height of the disc, $\dot{N}_\nu$ and $\dot{N}_{\bar{\nu}}$ are the number fluxes of neutrinos and antineutrinos leaving the disc, ρ is the baryon density of the disc, Y_e is the ratio of proton number density and the total baryon number density, and n_ν and $n_{\bar{\nu}}$ are the neutrino and antineutrino number densities. In [Chen and Beloborodov, 2007] the authors find that $\dot{N}_\nu \approx \dot{N}_{\bar{\nu}}$, and Y_e is close to its local thermal equilibrium value.

The transport of neutrinos across the disc is characterized by their optical depth, which is determined by the cross sections for several neutrino interactions. Neutrinos can be absorbed by nucleons or annihilate into electrons and positrons. There is also neutrino scattering by baryons, electrons and positrons. The cross sections for all these processes are of the same importance (of the same order of magnitude) for neutrinos with energies of a few MeV (see [Burrows and Thompson, 2002] or appendix B of [Chen and Beloborodov, 2007]).

Hyper-accreting discs emit large neutrino fluxes if the mass accretion rate is larger than $\dot{M}_{\rm ign}$. The disc is efficiently cooled by neutrinos if the mass accretion rate is below $\dot{M}_{\rm trap}$. The characteristic accretion rates $\dot{M}_{\rm ign}$ and $\dot{M}_{\rm trap}$ depend on the viscosity parameter α. They were calculated in [Chen and Beloborodov, 2007], and the numerical results are well approximated by the following formulae,

$$\dot{M}_{\rm ign} = K_{\rm ign}\left(\frac{\alpha}{0.1}\right)^{5/3}, \qquad \dot{M}_{\rm trap} = K_{\rm trap}\left(\frac{\alpha}{0.1}\right)^{1/3}. \tag{1.21}$$

The coefficients $K_{\rm ign}$ and $K_{\rm trap}$ are functions of the black-hole spin a. For $a = 0$, $K_{\rm ign} = 0.071 M_\odot s^{-1}$ and $K_{\rm trap} = 9.3 M_\odot s^{-1}$. For $a = 0.95$, $K_{\rm ign} = 0.021 M_\odot s^{-1}$ and $K_{\rm trap} = 1.8 M_\odot s^{-1}$.

Even for hyper-accreting discs equation 1.18 (changing σ by $7\sigma/8$ to account for the different statistics of neutrinos and photons) is a good estimate for the temperature of neutrinos emitted by the optically thick regions of the disc. See section 3.2 for the spectrum of neutrinos in optically thin regions of the disc. The disc is slim in its inner region if the mass accretion rate is in between $\dot{M}_{\rm ign}$ and $\dot{M}_{\rm trap}$.

1.3.5 Further considerations

There are many important aspects of accretion disc theory that are not discussed in this short introduction. This section ends with a list of caveats to keep in mind.

The disc may not necessarily be geometrically thin. A general class of geometrically thick discs are advection dominated accretion flows (ADAFs). In this case the disc puffs up because of its high internal energy content (See [Narayan *et al.*, 1998] and [Narayan and McClintock, 2008] for a reviews). If on the surface of the disc the radiation pressure force on ions is larger than the bounding gravitational tidal force, then the disc puffs up. The critical luminosity when this happens is known as the Eddington luminosity. The mass accretion rate may not be stationary. For example a disc that formed during the collapse of a Wolf–Rayet star will have a variable accretion rate resembling the density stratification of the star before the collapse. The accretion disc of an active galactic nucleus is partially fed by sporadic tidal disruption of stars. Many different instabilities can occur in accretion discs. Some can be thermally unstable, or gravitationally unstable and prone to fragmentation. Extended discussion of this considerations is found in [Pringle, 1981].

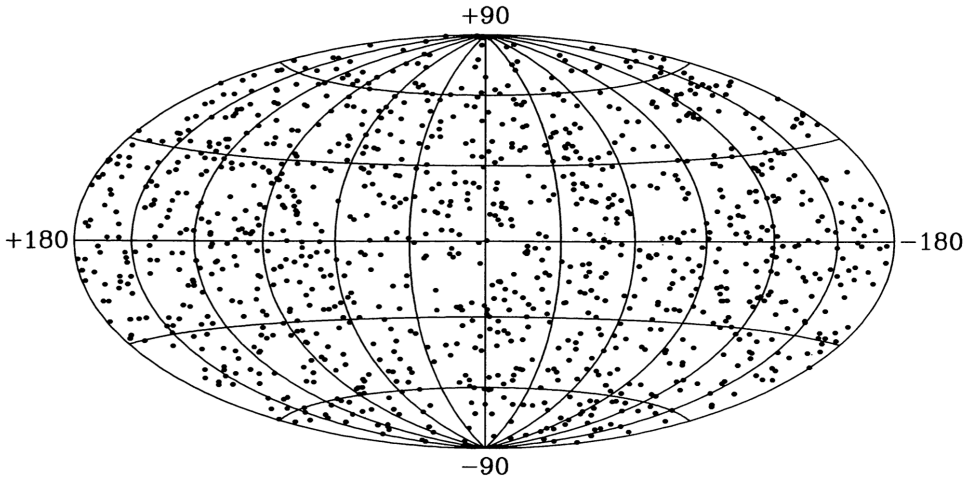

Figure 1.2: Sky distribution of GRBs. The figure shows about a thousand bursts detected by BATSE before 1997 (from [Meegan *et al.*, 1996]).

1.4 Gamma-ray bursts

In the late 1960s the Vela satellites, designed to detect nuclear detonations on Earth, serendipitously detected short bursts of gamma-rays not originating from the Sun or the Earth [Klebesadel *et al.*, 1973]. Gamma-ray bursts (GRBs), as they are now known, are the most energetic explosions since the Big Bang. These explosions involve the release of energies comparable to a thousandth of the rest-mass energy of the sun in a few seconds. See [Piran, 1999], [Piran, 2004] and [Mészáros, 2006] for reviews.

1.4.1 Observations

At the time of their discovery it was unknown if GRBs were coming from cosmological distances or from the nearby universe. Now we know, from redshift measurements [Metzger *et al.*, 1997], that they come from cosmological distances and are uniformly distributed on the sky (see figure 1.2, from [Meegan *et al.*, 1996]).

GRBs radiate most of the energy in a few seconds. Since early observations, it was noted that the duration of GRBs follows a bimodal distribution. The boundary

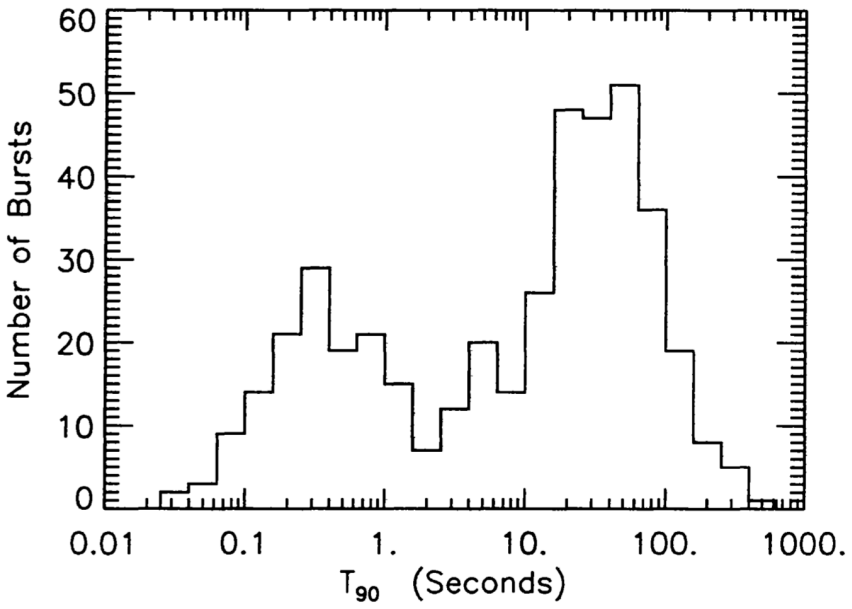

Figure 1.3: Distribution of GRB durations. T_{90} is the time in which the detector receives 90% of the total burst energy (from [Meegan *et al.*, 1996]).

between the two distributions is at about 2 seconds. Bursts lasting longer than 2 seconds are known as *long* GRBs and *short* otherwise. Figure 1.3 shows the duration distribution for bursts detected by BATSE on and before 1996.

Telescopes keep detecting emission from the source for several days after the initial burst of gamma-rays. Figure 1.4 (from [Panaitescu, 2006]) shows the light curve for a typical GRB. The prompt emission (typically lasting 0.1–10^3 seconds) is followed by a fast decay in flux and the spectrum shifts to the X-ray range. In this phase flares are common. Between 10^3 and 10^5 seconds usually a plateau is observed, sometimes accompanied by flares. Then the X-ray luminosity decreases. At about 10^6 seconds, a steepening in the light curve is often observed. If this "break" is achromatic, it is associated with the beaming angle of the explosion. Using this interpretation, energies of about 10^{51}–10^{52} erg have been inferred for GRBs (see [Sari *et al.*, 1999], [Cenko *et al.*, 2010]).

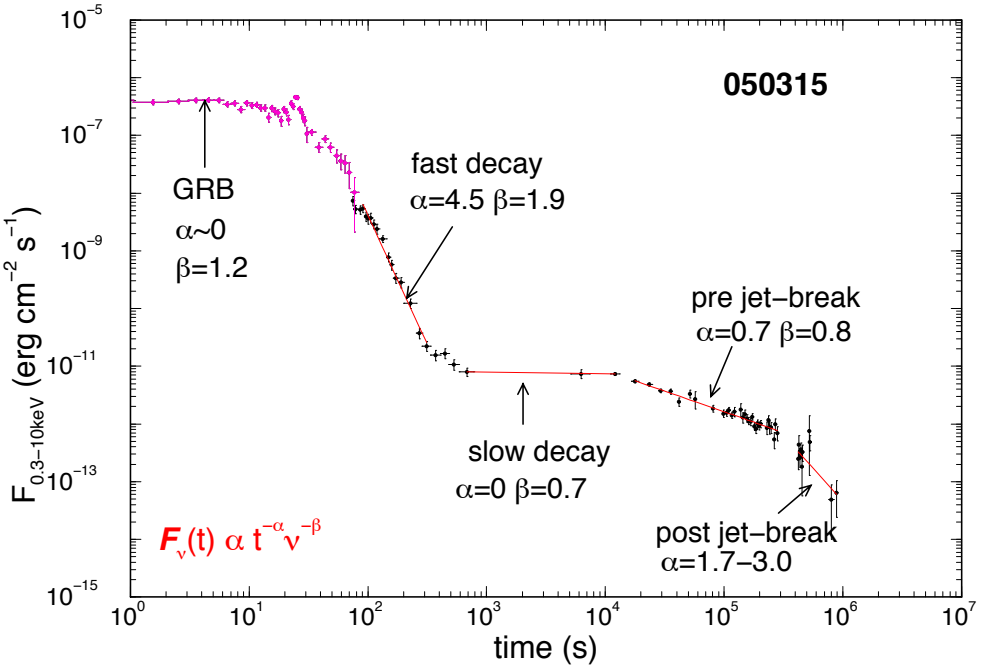

Figure 1.4: Typical light curve showing the prompt and afterglow emission from GRB 050315 (from [Panaitescu, 2006]).

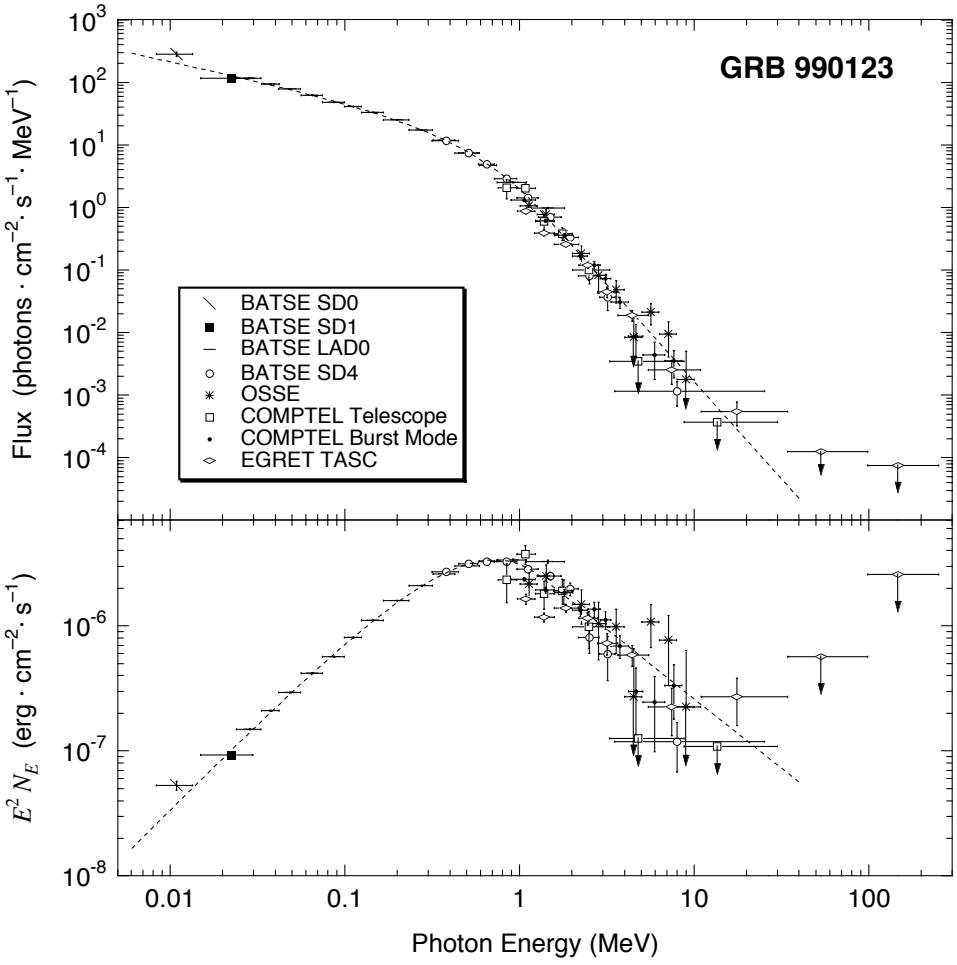

Figure 1.5: Shape of the spectrum of the prompt emission from GRBs. The peak of the spectrum is typically in between 0.1 and 1 Mev (from [Briggs *et al.*, 1999]).

A typical spectrum of the prompt emission is shown in figure 1.5 (from [Briggs *et al.*, 1999]). Most of the energy of the GRB is carried by photons of energies of $E_{\rm peak} \approx 1$ MeV. This spectrum can be fitted with two power laws with different indices on each side of $E_{\rm peak}$ (e.g.[Band *et al.*, 1993]). The prompt emission is produced by Compton scattering of low energy photons and, if a significant magnetic field is present, through synchrotron radiation from electrons and positrons. A "hot" flow of electrons and positrons is needed for this emission processes to work. One proposed way for heating the electron flow is through the formation of shock fronts in the GRB outflow [Rees and Meszaros, 1994]. Another mechanism is heating of the electrons via energy dissipation by magnetic reconnection (see [Thompson, 1994], [Spruit *et al.*, 2001], [Giannios, 2008]). A third mechanism that produces this spectrum is pion creation after the collisions of neutrons and protons in the GRB outflow. The pions ultimately decay into e^+e^- pairs which eventually create the observed high energy part of the spectrum by Comptonization of the lower energy photon field [Beloborodov, 2010].

1.4.2 Central engine

The typical time variability of the prompt emission from GRBs is of about $\tau \approx 10^{-2}$s. This would imply that the emitting region should not have an spatial extension of more than $l = \tau c \approx 3000$ km. From observations we know that GRBs emit about $E \approx 10^{51}$erg in gamma rays. This has the paradoxical implication that gamma-rays with an energy density of $E/(4\pi l^3/3)$ will immediately produce electron positron pairs via $\gamma\gamma \rightarrow e^+e^-$, implying that the high energy part of the spectrum should not be observed. A solution for this paradox is to propose that the photons are emitted by matter moving with a large Lorentz factor, Γ, towards the observer. The effect of this is two-fold. One, the time variability in the frame of the matter flow is dilated with respect to the observer by a factor of 2Γ. Two, the energy of the photons in the rest frame of the flow is reduced by a factor of Γ, and this reduces the number of

photons that can pair produce. From these arguments one infers that GRBs should be produced from ultra-relativistic matter flows with Lorentz factor of the order of 100 or larger (e.g. see [Lithwick and Sari, 2001] and also [Piran, 1999], [Mészáros, 2006]).

The physical processes that create the macroscopic flow of ultra-relativistic matter is a topic of current research. There are two leading mechanisms. Both of them involve a central black hole which forms after the collapse of a massive star or the merger of two compact objects.

One mechanism stipulates that most of the energy of the GRB comes from the radiation emitted by a hyper-accreting accretion disc around the black hole. In this case neutrinos carry away energy from the disc and subsequently deposit part of it in the vicinity of the black hole by annihilating into electron-positron pairs via $\nu\bar{\nu} \to e^+e^-$ (see [Narayan *et al.*, 1992], [Popham *et al.*, 1999], [Chen and Beloborodov, 2007], [Zalamea and Beloborodov, 2011] and references therein).

The second leading mechanism stipulates that most of the energy of the GRB comes from the rotational energy of the newly formed black hole. The rotational energy of the black hole can be carried away by a Poynting flux if there is a regular large scale magnetic field that pierces the black hole ([Blandford and Znajek, 1977]). An open question is how efficiently can the electromagnetic Poynting flux be dissipated into kinetic energy of the matter flow and energy of the radiation flow (e.g. [Metzger *et al.*, 2011]).

1.5 Gravitational waves

Einstein's equation of general relativity

$$G^{\mu\nu} = \frac{8\pi G}{c^4} T^{\mu\nu} \tag{1.22}$$

predicts the existence of gravitational waves when linearized around Minkowski metric $\eta_{\mu\nu}$. Writing the metric as

$$g_{\mu\nu} = \eta_{\mu\nu} + h_{\mu\nu}, \quad |h_{\mu\nu}| \ll 1, \tag{1.23}$$

Einstein's equation takes the form

$$\Box \tilde{h}^{\mu\nu} = \frac{16\pi G}{c^4} T^{\mu\nu} \tag{1.24}$$

where only linear terms in $h_{\mu\nu}$ are kept, and

$$\tilde{h}^{\mu\nu} \equiv h^{\mu\nu} - h^{\alpha}_{\ \alpha}\eta^{\mu\nu}. \tag{1.25}$$

Equation 1.24 is a wave equation for each component of $\tilde{h}_{\mu\nu}$.

1.5.1 Gravitational radiation from point masses

The effect of gravitational radiation on the Keplerian orbit of two point masses was worked out by [Peters and Mathews, 1963] and [Peters, 1964]. These authors find that the binary system loses energy and angular momentum at the following average rates per orbit

$$< \dot{E} > \ = \ -\frac{32}{5}\frac{G^4 m_1^2 m_2^2 (m_1+m_2)}{c^5 a^5 (1-e^2)^{7/2}} \left(1 + \frac{73}{24}e^2 + \frac{37}{96}e^4\right), \tag{1.26}$$

$$< \dot{L} > \ = \ -\frac{32}{5}\frac{G^{7/2} m_1^2 m_2^2 (m_1+m_2)^{1/2}}{c^5 a^5 (1-e^2)^{2}} \left(1 + \frac{7}{8}e^2\right), \tag{1.27}$$

where m_1 and m_2 are the masses of the point particles, and a and e are the semi-major axis and eccentricity of the orbit. Although equations 1.26 and 1.27 were derived for the case when the metric is everywhere close to Minkowski, [Martel, 2004] finds them to be a good approximation for the case when one of the masses is a Schwarzschild black hole and the other one is a test particle.

1.5.2 Detection of gravitational waves

The first experimental evidence for the existence of gravitational waves came from the precise measurements of the orbital period of a binary system ([Hulse and Taylor,

1975], [Taylor and Weisberg, 1989] and [Weisberg *et al.*, 2010]). Figure 1.6 shows, for PSR1913+16, the remarkable agreement between the observed change in the orbital period and the prediction from general relativity.

Although the agreement between theory and observations for PSR1913+16 is a confirmation of the existence of gravitational radiation, so far there has not been direct detection of gravitational waves. There are several experiments that aim at a direct detection. The Laser Interferometer Gravitational Wave Observatory (LIGO)[2] is a ground based detector which uses two laser interferometers to detect gravitational waves. LIGO is most sensitive to gravitational waves with frequencies around 10^2 Hz. Such waves can be produced by mergers of stellar-mass compact objects. Another proposed experiment is the Laser Interferometer Space Antenna[3][4]. LISA is expected to be most sensitive at frequencies around 10^{-3} Hz, this includes mergers of massive black holes and mergers of massive black holes and stellar mass compact objects. Figure 1.7 shows the sensitivities of LISA and LIGO and the expected detectable sources for each experiment.

The possibility of dual detection of gravitational and electromagnetic radiation has recently attracted the attention of the astrophysical community. See [Bloom *et al.*, 2009] and [Phinney, 2009] for two Astro2010 Decadal Survey Whitepapers. A particular application worth of attention is the possibility to create a new version of the Hubble diagram based on gravitational distance measurements (see [Menou *et al.*, 2008] and references therein).

---

[2]http://www.ligo.caltech.edu/

[3]http://lisa.nasa.gov/

[4]LISA was initially a joint project of NASA and ESA, but currently NASA has backed out and it is under study only by ESA.

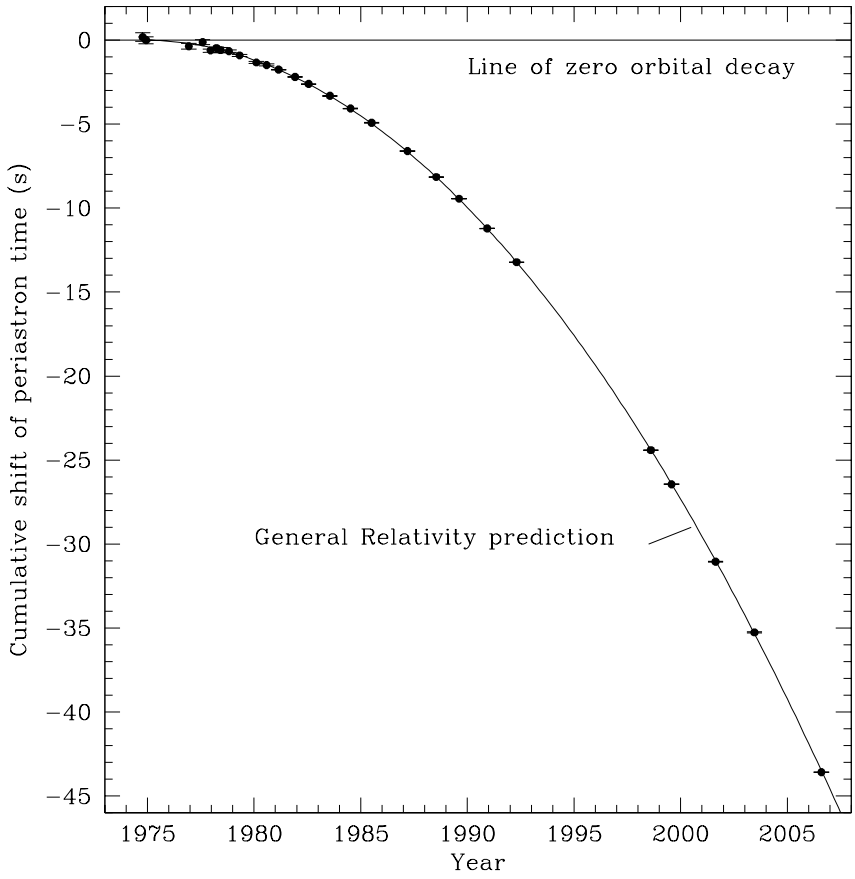

Figure 1.6: The figure shows the cumulative shift of periastron time for pulsar PSR 1913+16 since October 1974. Figure from [Weisberg et al., 2010].

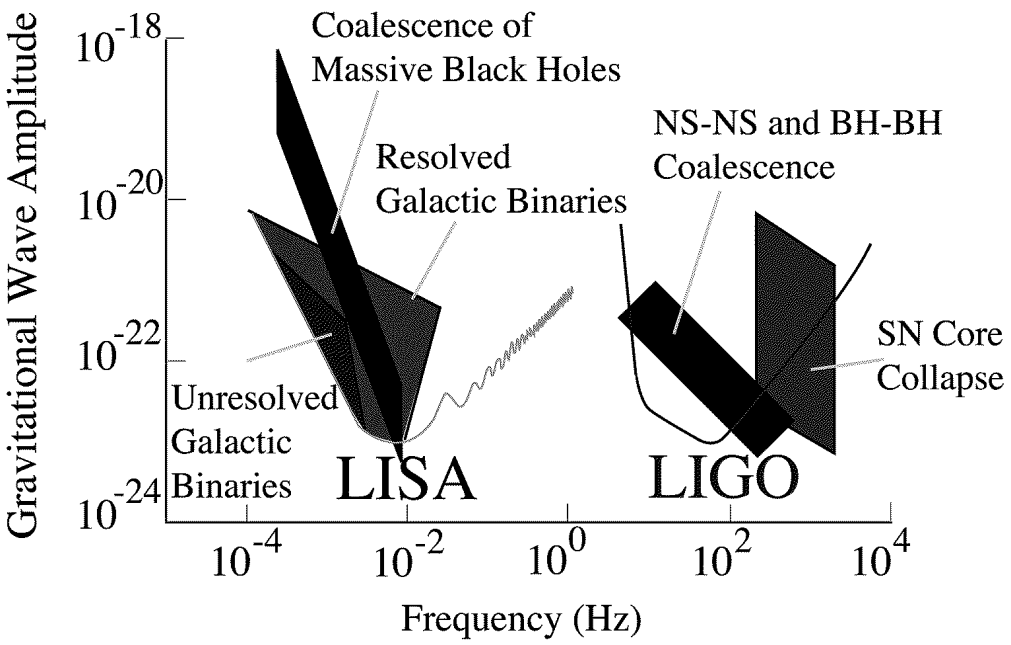

Figure 1.7: The figure shows the gravitational wave amplitude for which LISA and LIGO are sensitive as a function of the gravitational wave frequency. The shaded regions show different sources that would produce detectable signals. Adapted from http://imagine.gsfc.nasa.gov/

Chapter 2

Mini-discs around spinning black holes

Ivan Zalamea, Andrei M. Beloborodov

[Published in MNRAS, 398:2005–2011, October 2009]

Accretion onto black holes in wind-fed binaries and in collapsars forms small rotating discs with peculiar properties. Such "mini-discs" accrete on the free-fall time without help of viscosity and nevertheless can have a high radiative efficiency. The inviscid mini-disc model was previously constructed for a non-rotating black hole. We extend the model to the case of a spinning black hole, calculate the structure and radiative efficiency of the disc and find their dependence on the black hole spin. If the angular momenta of the disc and the black hole are anti-aligned, a hydrodynamic analog of Penrose process takes place.

2.1 Introduction

The mini-disc model was motivated by the estimate for angular momentum of accretion flows, l, in wind-fed X-ray binaries ([Illarionov and Sunyaev, 1975] ; [Shapiro and Lightman, 1976] ; [Illarionov and Beloborodov, 2001]). These systems happen to

have $l \sim r_g c$, where $r_g = 2GM/c^2$ is the gravitational radius of the black hole. It is marginally sufficient to form a centrifugally supported disc. Then a small disc can form, which is not supported centrifugally and instead accretes on the free-fall time ([Beloborodov and Illarionov, 2001], hereafter BI01). The mini-disc accretes so fast (super-sonically) that the effects of viscosity can be neglected. A similar disc may form inside collapsing stars ([Lee and Ramirez-Ruiz, 2006] ; [Beloborodov, 2008]).

The mini-disc can be thought of as a caustic in the equatorial plane of a rotating accretion flow. It absorbs the feeding infall, and this interaction releases energy, making the accretion radiatively efficient. With increasing angular momentum, the size of the disc grows up to $14 r_g c$, and at this point the centrifugal barrier stops accretion, so that it can proceed only on a viscous timescale. Thus, the mini-disc model fills the gap between two classical regimes of accretion — spherical ($l < r_g c$, [Bondi, 1952]) and standard accretion disc ($l \gg r_g c$, [Shakura and Sunyaev, 1973]) — and is qualitatively different from both.

The calculations of BI01 were limited to the case of a Schwarzschild black hole. In the present paper we study the mini-disc around Kerr black holes. The model is constructed under the following assumptions:

(i) The flow is axially symmetric. We assume that the rotational axes of the accretion flow and the black hole are aligned (or anti-aligned).

(ii) The flow is symmetric under reflection about the equatorial plane. The symmetric streamlines collide in the equatorial plane and form a ring-like caustic around the black hole.

(iii) The flow falls freely (ballistically) from a large radius $r \gg r_g$ until it hits the caustic; its pressure is negligible everywhere except in the mini-disc. This assumption is valid if the flow is cooled efficiently (by radiation in X-ray binaries or by neutrinos in collapsars). The heat released in the shocks that accompany the disc-infall interaction is assumed to be quickly radiated away, so that the shocks stay near the disc plane, forming a "sandwich". The validity of this assumption is discussed in BI01 for the

case of X-ray binaries and in [Beloborodov, 2008] for collapsars.

(iv) The flow is quasi-steady: its accretion rate and angular momentum remain constant on the timescale of accretion through the mini-disc (which is comparable to the free-fall time from $r \sim 10r_g$).

The paper is organized as follows. Section 2 describes the parabolic ballistic infall in Kerr metric and its ring caustic in the equatorial plane. In section 3 we write down the equations that govern the gas motion in the caustic (the mini-disc) and solve the equations numerically. In section 4 we calculate the total luminosity of the disc observed at infinity, taking into account the light capture into the black hole.

2.2 Supersonic infall with angular momentum

The spacetime of a black hole of mass M and angular momentum J is described by the Kerr metric. In Boyer-Lindquist coordinates (ct, r, θ, ϕ) the metric is given by

$$\begin{aligned} g_{ij}dx^i dx^j &= -\left(1-\frac{r_g r}{\rho^2}\right)(cdt)^2 - \frac{2r_g a r}{\rho^2}\sin^2\theta (cdt)d\phi \\ &\quad + \frac{\rho^2}{\Delta}dr^2 + \rho^2 d\theta^2 + \frac{\sin^2\theta}{\rho^2} \\ &\quad + \left[(r^2+a^2)^2 - a^2\Delta\sin^2\theta\right]d\phi^2, \end{aligned} \tag{2.1}$$

$$\rho^2 = r^2 + a^2\cos^2\theta, \tag{2.2}$$

$$\Delta = r^2 - r_g r + a^2. \tag{2.3}$$

The spin parameter of the black hole $a = J/Mc$ has dimension of cm and must be in the interval $|a| \le r_g/2 = GM/c^2$. Throughout the paper we shall also use the dimensionless parameter $a_\star = ac^2/GM$, $|a_\star| \le 1$.

We assume that the gas infall forms at a large radius $r \gg r_g$, where it is efficiently cooled and, like dust, begins to fall freely towards the black hole. A streamline of this ballistic infall is determined by three integrals of motion: specific angular momentum l, its projection l_z on the spin axis of the black hole, and specific orbital energy $E \approx c^2$

(the infall is nearly parabolic). The four-velocity of a parabolic free-fall in Kerr metric is given by (e.g. Misner et al. 1973),

$$\rho^2 \frac{dr}{d\tau} = \pm c\sqrt{R}, \tag{2.4}$$

$$\rho^2 \frac{d\theta}{d\tau} = \pm\sqrt{\Theta}, \tag{2.5}$$

$$\rho^2 \frac{d\phi}{d\tau} = \frac{1}{\Delta}\left(cr_g ar - a^2 l_z\right) + \frac{l_z}{\sin^2\theta}, \tag{2.6}$$

$$\rho^2 \frac{dt}{d\tau} = \frac{1}{\Delta}\left[\left(r^2+a^2\right)^2 - r_g ar\frac{l_z}{c}\right] - a^2\sin^2\theta, \tag{2.7}$$

where $l_z = l\sin\theta_\infty$, θ_∞ is the asymptotic polar angle of a streamline at large r, and

$$\begin{aligned} R(r) &= r_g r^3 - \frac{l^2}{c^2}r^2\left(1-\frac{r_g}{r}\right) - 2r_g a\frac{l}{c}r\sin\theta_\infty \\ &\quad + a^2\left(r_g r - \frac{l^2}{c^2}\cos^2\theta_\infty\right), \end{aligned} \tag{2.8}$$

$$\Theta(\theta) = l_z^2(\cot^2\theta_\infty - \cot^2\theta). \tag{2.9}$$

The ballistic accretion flow is completely specified by the distribution of its density and angular momentum on a sphere of a large radius $r \gg r_g$. As the gas approaches the black hole and develops a significant rotational velocity, the infall is deflected from pure radial motion, and its streamlines intersect in the equatorial plane. The radius of this collision is determined by the angular momentum of the colliding symmetric streamlines.

2.2.1 Collision Radius

The streamline coming from an asymptotic direction $(\theta_\infty, \phi_\infty)$ with angular momentum $l(\theta_\infty, \phi_\infty)$ reaches the equatorial plane and collides with the symmetric streamline at the radius $r_\star$ defined by

$$-\int_\infty^{r_\star}\frac{dr}{\sqrt{R}} = \int_{\theta_\infty}^{\pi/2}\frac{cd\theta}{\sqrt{\Theta}} = \frac{\pi c}{2l}. \tag{2.10}$$

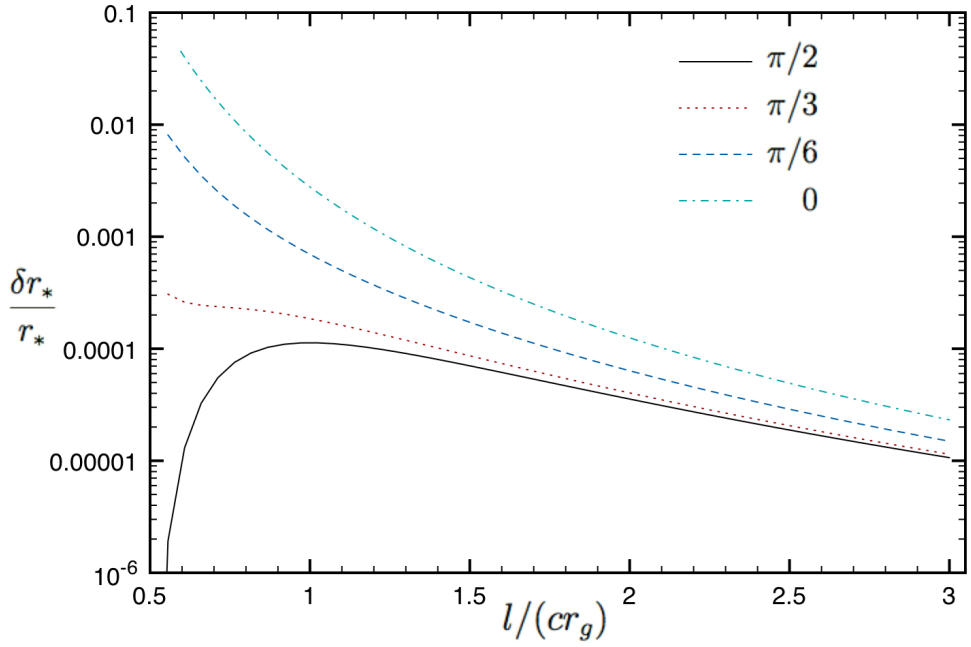

Figure 2.1: Fractional difference between the exact $r_\star$ and its approximation (eq. 2.11) as a function of l. The curves start at $l_0 = l_\star$ that corresponds to $r_\star$ at the horizon of the black hole. All curves are plotted for maximally rotating black holes ($a_\star = 1$), when eq. (2.11) is least accurate.

We solved this equation for $r_\star$ numerically (it involves an elliptic integral on the left-hand side). A good analytical approximation to $r_\star$ is given by

$$r_\star \approx \frac{l^2}{GM} - r_g\Big[\frac{10-3\pi}{4}\left(\frac{l_{eff}}{l}\right)^2 - \frac{48-15\pi}{16}\left(\frac{ac\cos\theta_\infty}{l}\right)^2\Big], \tag{2.11}$$

where $l_{eff}^2 \equiv l^2 + (ac)^2 - 2acl\sin\theta_\infty$. The accuracy of this approximation is shown in Figure 2.1. It is better than 3 per cent when $r_\star$ is outside the horizon, for any set of parameters relevant for the mini-disc formation.

The collision radius is maximum for the streamlines near the equatorial plane

($\theta_\infty \to \pi/2$). This defines the outer radius of the disc,

$$r_d = r_\star \left(\theta_\infty = \frac{\pi}{2}\right). \tag{2.12}$$

2.2.2 Non-intersection of streamlines above the equatorial plane

The ballistic flow defines a mapping from the sphere $(\theta_\infty, \phi_\infty)$ to a sphere of radius r (cf. BI01): $(\theta_\infty, \phi_\infty) \to (\theta(r), \phi(r))$. The streamlines of the flow do not intersect before reaching the equatorial plane if the Jacobian of this mapping remains positive for all $r > r_\star$, i.e.

$$\mathcal{J} = \mathrm{Det} \begin{pmatrix} \dfrac{\partial\theta(r)}{\partial\theta_\infty} & \dfrac{\partial\phi(r)}{\partial\theta_\infty} \\ \\ \dfrac{\partial\theta(r)}{\partial\phi_\infty} & \dfrac{\partial\phi(r)}{\partial\phi_\infty} \end{pmatrix} > 0. \tag{2.13}$$

This condition is equivalent to $\partial\theta(r)/\partial\theta_\infty > 0$. Using the relation between θ and r,

$$\frac{\cos\theta(r)}{\cos\theta_\infty} = \cos\psi, \qquad \psi \equiv \frac{l}{c}\int_r^\infty \frac{dr}{\sqrt{R}}, \tag{2.14}$$

one finds that $\mathcal{J} > 0$ if

$$\frac{d\cos\theta(r)}{d\cos\theta_\infty} = \cos\psi - \cos\theta_\infty \sin\psi \frac{d\psi}{d\cos\theta_\infty} > 0. \tag{2.15}$$

This condition must be checked for a given distribution of angular momentum $l(\theta_\infty)$. In the numerical examples below we assume a distribution of the form

$$l(\theta_\infty) = l_0 \sin\theta_\infty, \tag{2.16}$$

(rigid-body rotation at infinity). We find that the streamlines do not intersect before reaching the ring caustic in the equatorial plane.

2.3 Disc Dynamics

We consider here only accretion flows that are asymptotically spherical at $r \gg r_g$, i.e. we assume that the accretion rate at infinity is spherically symmetric, $d\dot{M}/d\Omega_\infty =$

$const = \dot{M}_{\rm tot}/4\pi$. Streamlines that start at θ_∞ with angular momentum $l(\theta_\infty)$ reach the equatorial caustic at a radius $r_\star(\theta_\infty)$. The accretion rate through the disc at a radius r, $\dot{M}(r)$, equals the net accretion rate along the streamlines that enter the caustic outside r,

$$\dot{M}(r) = \dot{M}_{\rm tot} \cos\theta_\infty(r), \tag{2.17}$$

where $\theta_\infty(r)$ is the asymptotic polar angle of streamlines that collide at radius r. We find it by inverting the function $r_\star(\theta_\infty)$.

Matter inside the disc moves horizontally with four-velocity $u^i = (u^t, u^r, 0, u^\phi)$ and density ρ. The disc is steady and axially symmetric, so u^i and ρ depend on r only. Equations for $u^i(r)$ and $\rho(r)$ are derived using the conservation laws for baryon number, energy and momentum. These laws are expressed by the following general equations (e.g.[Landau and Lifshitz, 1971]),

$$\frac{1}{\sqrt{-g}}\partial_i(\sqrt{-g}\rho u^i) = 0, \tag{2.18}$$

$$\frac{1}{\sqrt{-g}}\partial_k(\sqrt{-g}T^k_i) = \frac{1}{2}\frac{\partial g_{kl}}{\partial x^i}T^{kl}, \tag{2.19}$$

where $T^{kl} = \rho c^2 u^k u^l$ is the stress-energy tensor; we assume that it is dust-like everywhere, i.e. neglect the internal energy density, pressure, and magnetic fields compared with ρc^2. The radiation leaving the disc contributes to the energy momentum tensor with (e.g. [Misner *et al.*, 1973])

$$T^{ij}_{rad} = u^i q^j + u^j q^i, \tag{2.20}$$

where q^i is the four-flux of radiation. The effects of radiation on the dynamics of the disc are of the order of $\epsilon = L/\dot{M}c^2$, where L is luminosity of the disc. In what follows we will neglect the contribution of T^{ij}_{rad} since for most disc models $\epsilon \ll 1$. Above the disc, the stress-energy tensor is that of the ballistic infall. The infall four-velocity and density just above the disc shall be denoted by $\hat{u}^i$ and $\hat{\rho}$, to distinguish them from the similar quantities inside the disc, u^i and ρ. Then the conservation laws (eqs. 2.18

and 2.19) give [1],

$$\frac{d\dot{M}}{dr} = -4\pi r^2 \hat{\rho}\hat{u}^{\theta}, \tag{2.26}$$

$$\frac{d}{dr}\left(\frac{h}{r}T_i^r\sqrt{-g}\right) + 2\sqrt{-g}\hat{T}_i^{\theta} = \frac{1}{2}\frac{h}{r}\sqrt{-g}\frac{\partial g_{kl}}{\partial x^i}T^{kl}. \tag{2.27}$$

Here $\dot{M} = 2\pi r h \rho u^r$, h is the thickness of the disc, and $\hat{T}^{kl} = \hat{\rho}c^2\hat{u}^k\hat{u}^l$ is the stress-energy tensor of the infall. Using equation (2.26) one finds from equation (2.27)

$$\frac{d}{dr}(\dot{M}u_i) - \hat{u}_i\frac{d\dot{M}}{dr} = \frac{1}{2}\frac{\partial g_{kl}}{\partial x^i}u^k u^l\frac{\dot{M}}{u^r}. \tag{2.28}$$

For $i = \{t, \phi\}$ (conservation of energy and angular momentum) the right-hand side of this equation vanishes. In particular, for $i = \phi$ this equation gives

$$\frac{d(\dot{M}u_\phi)}{dr} = \hat{u}_\phi\frac{d\dot{M}}{dr}, \tag{2.29}$$

$$u_\phi(r) = -\frac{1}{\dot{M}(r)}\int_r^{r_d}\hat{u}_\phi\frac{d\dot{M}}{dr}dr. \tag{2.30}$$

---

[1] In general, conservation laws are written in the form

$$\partial_\mu(f^\mu) = g. \tag{2.21}$$

We want to integrate equation 2.21 across the perpendicular direction of a planar region, with angular symmetry and for time independent functions. In general,

$$\int dx^4\Big(\partial_\mu(f^\mu) - g\Big) = 0, \tag{2.22}$$

$$0 = \int_{t_1}^{t_2} dt\int_V dx^3\Big(\partial_i(f^i) - g\Big) \quad \Rightarrow \quad \int_V dx^3\Big(\partial_i(f^i) - g\Big) = 0, \tag{2.23}$$

for any volume V. Using divergence theorem we can write

$$\int_{\partial V}\vec{ds}\cdot\vec{f} = \int_V dx^3 g. \tag{2.24}$$

Taking $V = \{$Equatorial ring of inner radius r and outer radius $r+dr$ and "small" height $h\}$ equation 2.24 reads

$$\frac{d}{dr}(\frac{h}{r}f^r) + 2\hat{f}^{\theta} = -\frac{h}{r}g, \tag{2.25}$$

where $\hat{\cdot}$ means evaluation of the function just above the disc.

For $l(\theta_\infty)$ given by equation (2.16) we have $\hat{u}_\phi \equiv l_z = l^2/l_0$ and, using equation (2.17), we find

$$u_\phi(r) = \frac{2}{3} l_0 + \frac{l^2(r)}{3 l_0}. \tag{2.31}$$

For $i = r$, equation (2.28) expresses conservation of radial momentum. Its right-hand side does not vanish, and one needs to evaluate $\frac{\partial g_{kl}}{\partial r} u^k u^l$. Substituting $u^\phi = (u_\phi - g_{t\phi} u^t)/g_{\phi\phi}$, using $u_i u^i = -c^2$ and collecting terms one can write

$$\frac{\partial g_{kl}}{\partial r} u^k u^l = A + B(u^r)^2 + C u_\phi^2 + D u_\phi u^t, \tag{2.32}$$

where A, B, C and D are functions of r only (detailed calculation of this coefficients is presented in Appendix A),

$$A = -\frac{r_g c^2 [r^4 + a^4 + 2a^2 r(r - r_g)]}{r[a^2 + r(r - r_g)][r^3 + a^2(r + r_g)]},$$

$$B = 2\partial_r g_{rr} - \frac{a^2 r(2r - 3r_g)}{[a^2 + r(r - r_g)][r^3 + a^2(r + r_g)]},$$

$$C = \frac{r^4(2r - 3r_g) - 2a^4 r_g + a^2 r(2r^2 - 3r_g r + 3r_g^2)}{[a^2 + r(r - r_g)][r^3 + a^2(r + r_g)]^2},$$

$$D = -\frac{2a r_g (3r^2 + a^2)}{[r^3 + a^2(r + r_g)]^2}. \tag{2.33}$$

Equation (2.28) for $i = r$ becomes

$$\begin{aligned} \frac{du^r}{dr} &= \frac{\hat{u}^r - u^r}{\dot{M}} \frac{d\dot{M}}{dr} \\ &\quad + \frac{A + (B - 2\partial_r g_{rr})(u^r)^2 + C u_\phi^2 + D u_\phi u^t}{2 g_{rr} u^r}. \end{aligned} \tag{2.34}$$

Finally, u^t can be expressed in terms of u^r and u_ϕ from $u_i u^i = -c^2$,

$$\begin{aligned} (u^t)^2 &= 1 + \frac{r_g(r^2 + a^2)}{r[a^2 + r(r - r_g)]} + \frac{u_\phi^2/c^2}{a^2 + r(r - r_g)} \\ &\quad + \frac{r^4 + a^2 r(r + r_g)}{[a^2 + r(r - r_g)]^2} \left(\frac{u^r}{c}\right)^2. \end{aligned} \tag{2.35}$$

In equation (2.34) all quantities are known functions of radius except u^r. We solve numerically this differential equation for $u^r(r)$. Example solutions are shown in Fig. 2.2, where we plot the radial and azimuthal velocities measured by ZAMO (zero-angular-momentum observer at fixed r; Appendix B gives the transformation of 4-vectors to the ZAMO frame).

If the angular-momentum parameter of the flow, l_0, exceeds a critical value $l_{\rm cr}$, accretion in the disc is stopped by the centrifugal barrier (u^r changes sign). For flows with $l_0 < l_{\rm cr}$ the radial velocity remains everywhere negative. As l_0 approaches $l_{\rm cr}$ the trajectory of disc accretion makes more turns around the black hole (see Fig. 2.3) and at $l_0 = l_{\rm cr}$ it makes infinite number of turns. Similar behavior was found for mini-discs around Schwarzschild black holes; in this case $l_{\rm cr} = 2.62 r_g c$ (BI01). For spinning black holes, $l_{\rm cr}$ depends on $a_\star$. We have evaluated numerically $l_{\rm cr}(a_\star)$ and the corresponding maximum size of the mini-disc $r_d(a_\star)$. The results are shown in Figure 2.4.

Figure 2.4 also shows the minimum value of l_0, denoted by $l_\star$, that is required to form a disc outside the black-hole horizon,

$$r_h(a_\star) = \frac{1+\sqrt{1-a_\star^2}}{2}\, r_g. \tag{2.36}$$

Accretion proceeds in the inviscid mini-disc regime when $l_\star < l_0 < l_{\rm cr}$. This range shrinks with increasing $a_\star > 0$, and expands if $a_\star < 0$ (which means that the black hole and the accretion flow rotate in the opposite directions).

Matter in the polar region of a quasi-spherical accretion flow falls directly into the black hole before crossing the equatorial plane. The mini-disc is formed in the other, equatorial part of the flow (cf. Fig. 1 in BI01). The boundary between these two accretion zones is determined by the condition $r_\star(l) = r_h$. Equation (2.17) gives the fraction of $\dot{M}_{\rm tot}$ that accretes through the disc,

$$\frac{\dot{M}(r_h)}{\dot{M}_{\rm tot}} = \cos\theta_\infty(r_h), \tag{2.37}$$

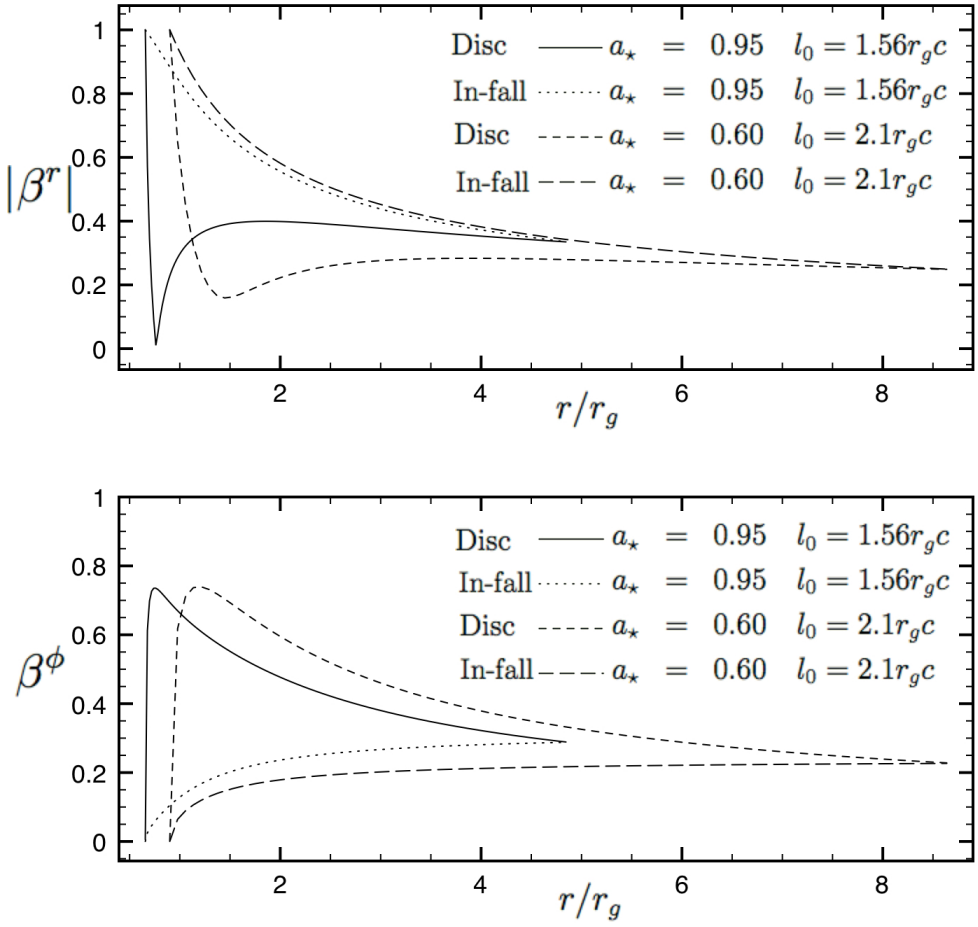

Figure 2.2: *Upper panel:* solutions for the radial velocity measured by ZAMO (in units of c) of the parabolic infall above the disc and the matter inside the disc. Two cases are shown: $a_\star = 0.6$, $l_0 = 2.1 r_g c$ and $a_\star = 0.95$, $l_0 = 1.56 r_g c$. *Lower panel:* the corresponding azimuthal velocities of the infall and the disc, measured by ZAMO.

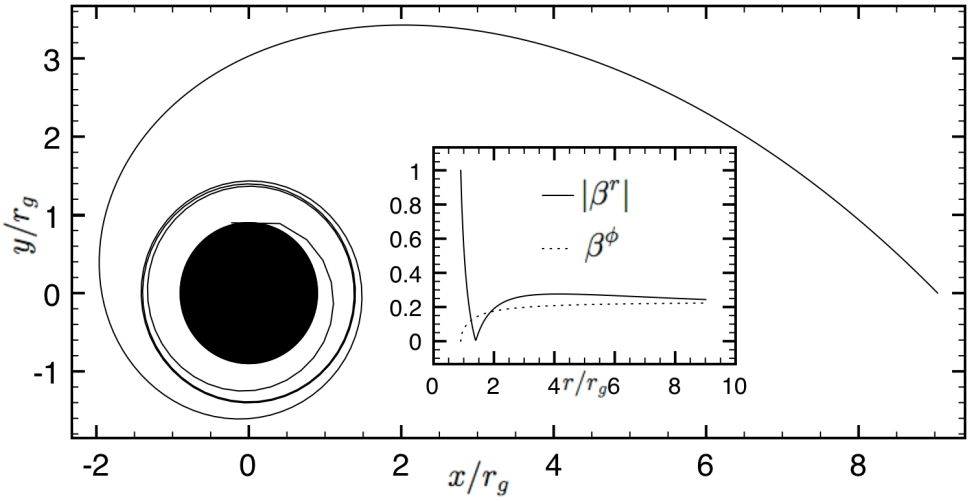

Figure 2.3: Trajectory of disc matter in the critical case $l_0 = 2.14 r_g c$ for a black hole with $a_\star = 0.6$. The insert shows the radial and azimuthal velocities of the disc measured by ZAMO. x and y are the coordinates in the equatorial plane defined by $x = r\cos\phi$, $y = r\sin\phi$.

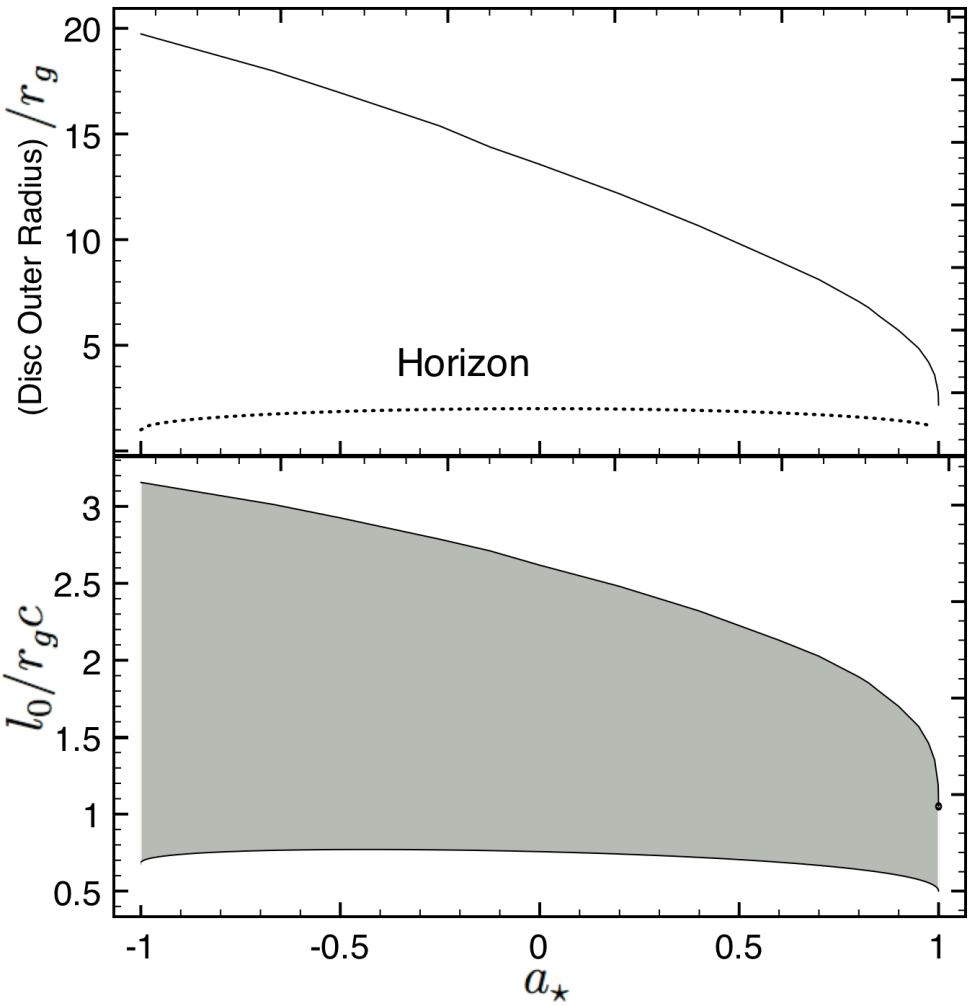

Figure 2.4: *Bottom panel:* the range of angular momenta $l_\star(a_\star) < l_0 < l_{\rm cr}(a_\star)$ that lead to the inviscid mini-disc regime (shaded region). Accretion with $l_0 < l_\star$ is quasi-spherical all the way into the black hole; it does not form a caustic outside the horizon. Accretion with $l_0 > l_{\rm cr}$ must proceed through a viscous, centrifugally supported disc. *Top panel:* maximum radius of the mini-disc ($l_0 = l_{\rm cr}$) as a function of the black-hole spin parameter $a_\star$ (solid curve). The radius of the black hole $r_h(a_\star)$ (eq. 2.36) is shown by the dotted curve.

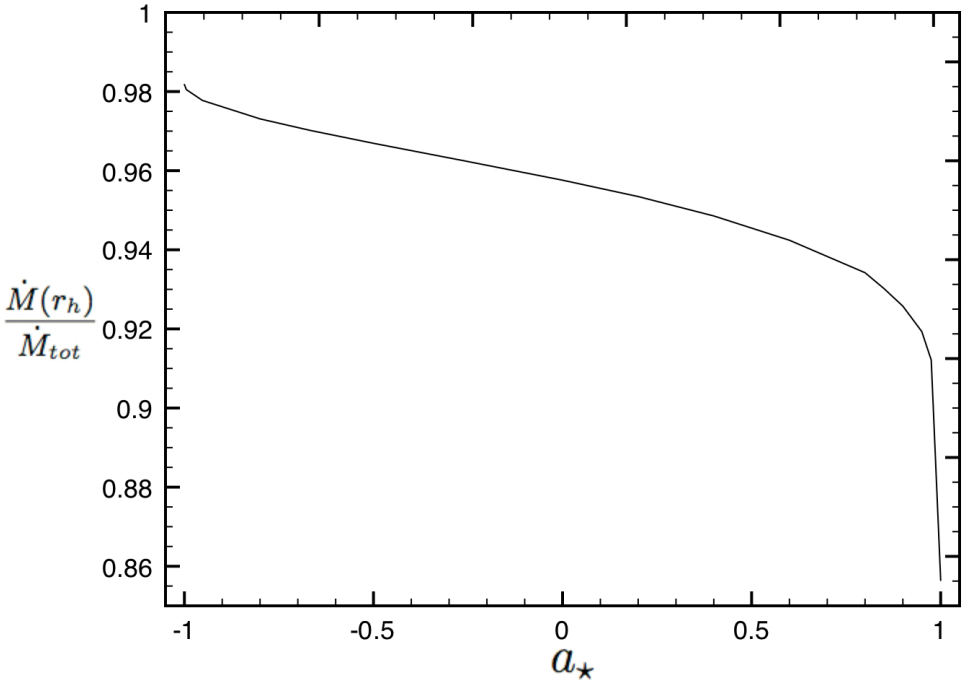

Figure 2.5: Maximum mass fraction accreted through the inviscid mini-disc. This maximum corresponds to $l_0 = l_{\rm cr}$ and depends on the black-hole spin $a_\star$ (see the text).

which depends on l_0 and a; it is maximum when $l_0 = l_{\rm cr}$. The maximum fraction is shown in Figure 2.5.

2.4 Disc luminosity

The mini-disc is a radiative caustic that converts kinetic energy of the acretion flow to radiation. Let $L(r)$ be the total luminosity produced by the disc outside radius r. The law of energy conservation gives an explicit expression for the luminosity,

$$L(r) = \left[c^2 + cu_t(r)\right] \dot{M}(r), \tag{2.38}$$

where c^2 is the initial orbital energy of the accretion flow at infinity and $-cu_t(r)$ is the orbital energy of the disc material at radius r. It is found using the solution for

$u^i(r)$ from section 3. The radial distribution of luminosity is given by dL/dr, and the total produced luminosity is $L = L(r_h)$. This luminosity would be received at infinity if no radiation were captured by the black hole.

When the capture effect is taken into account, the luminosity escaping to infinity may be written as

$$L_{\rm esc} = \int_{r_h}^{r_d} \frac{dL}{dr}\, f_{\rm esc}(r)\, dr, \tag{2.39}$$

where $f_{\rm esc}(r)$ is the escaping fraction of radiation emitted at radius r; the fraction $1 - f_{\rm esc}$ is absorbed by the black hole. Assuming that the emission is approximately isotropic in the rest frame of the disc, we derive in Appendix B

$$f_{\rm esc} = \left(1 - \frac{g_{t\phi}}{\sqrt{-\tilde{g}_{tt} g_{\phi\phi}}} \frac{\beta^\phi}{\gamma}\right)^{-1} \int_{S_{\rm esc}} \frac{1 - \dfrac{g_{t\phi}\bar{\Omega}^\phi}{\sqrt{-\tilde{g}_{tt} g_{\phi\phi}}}}{\gamma^4 (1 - \beta\cdot\bar{\mathbf{\Omega}})^3} \frac{d\bar{\Omega}}{4\pi}, \tag{2.40}$$

where β is the disc velocity (in units of c) measured by ZAMO (zero-angular-momentum observer at fixed r), $\gamma = (1-\beta^2)^{-1/2}$ and $\tilde{g}_{tt} = g_{tt} - g_{t\phi}^2/g_{\phi\phi}$. The integral is taken over the escape cone $S_{\rm esc}(r)$ — all photon directions $\bar{\mathbf{\Omega}}$ (in the ZAMO frame) that lead to escape. The calculation of these cones is described in Appendix B

The resulting $L_{\rm esc}(r)$ is found numerically. Figure 2.6 shows the radial distribution $dL_{\rm esc}/dr$ for mini-discs with three different l_0 around a black hole with spin parameter $a_\star = 0.9$. Most of the luminosity is produced in the region $r_g < r < 1.4 r_g$ where the infall velocity relative to the disc is large and hence a large energy is released in the disc-infall interaction.

We define the radiative efficiency of the disc as the ratio of the total luminosity radiated to infinity, $L_{\rm esc} = L_{\rm esc}(r_h)$, to the rest-mass flux through the disc,

$$\eta_{\rm esc} = \frac{L_{\rm esc}}{\dot{M}(r_h) c^2}. \tag{2.41}$$

If the light capture into the black hole is ignored, i.e. $L_{\rm esc}$ is replaced by L, the efficiency is given by

$$\eta = \frac{L(r_h)}{\dot{M}(r_h) c^2} = 1 + \frac{u_t(r_h)}{c}. \tag{2.42}$$

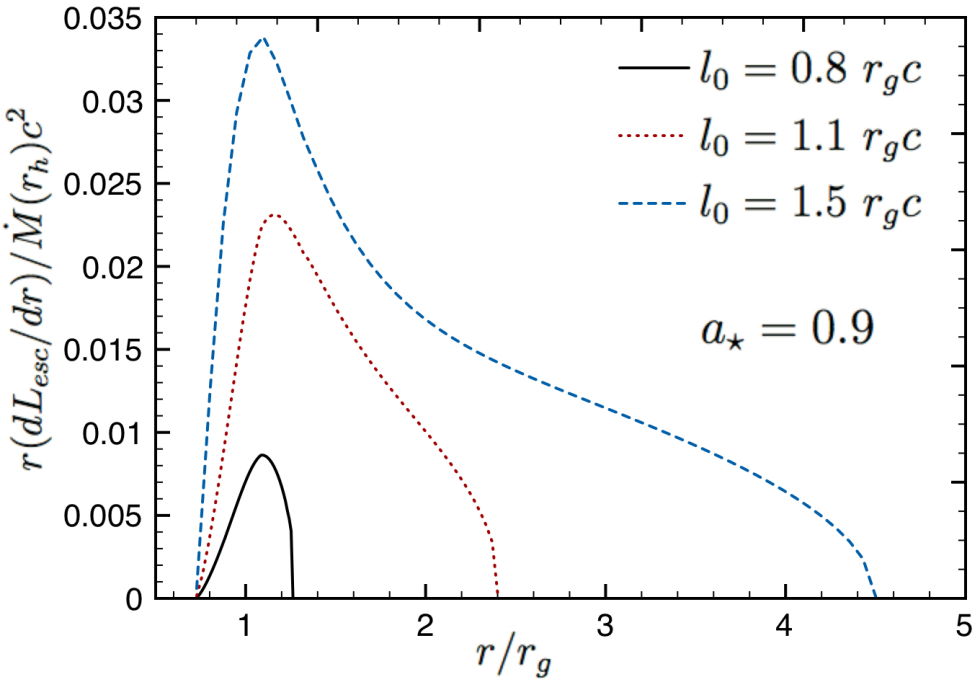

Figure 2.6: Radial distribution of escaping luminosity for discs with $l_0/r_g c = 0.8$, 1.1, and 1.5 around a black hole with spin parameter $a_\star = 0.9$. The luminosity is normalized by the rate of rest-mass accretion through the disc, $\dot{M}(r_h)c^2$.

We evaluated numerically the dependence of η on the two parameters of the mini-disc l_0 and $a_\star$ (Fig. 2.7). This dependence may be better understood if we express $u_t(r_h)$ in terms of $u^r(r_h)$ and $u_\phi(r_h)$ from $u_i u^i = -c^2$; then equation (2.42) yields

$$\begin{aligned} \eta &= 1 - \left(1 + \sqrt{1 - a_\star^2}\right)^{1/2} \frac{|u^r(r_h)|}{c\sqrt{2}} \\ &\quad -a_\star \left(1 + \sqrt{1 - a_\star^2}\right)^{-1/2} \frac{u_\phi(r_h)}{r_g c}. \end{aligned} \tag{2.43}$$

If $a_\star = 0$ this equation simplifies to $\eta = 1 - |u^r(r_h)|/c$ and gives a monotonic dependence of η on l_0: flows with larger angular momenta have smaller $|u^r(r_h)|$ (their radial motion is centrifugally decelerated) and higher η. In the case of a rotating black hole, equation (2.43) has additional terms which lead to a complicated dependence of η on l_0 and $a_\star$. For instance, when $a_\star = 0.9$ the dependence of η on l_0 is not monotonic (Fig. 2.7).

The efficiency η is generally increasing with increasing spin of the black hole. It is especially high for retrograde discs, which are described by the solutions with $a_\star < 0$. In this case, the second term on the right-hand side of equation (2.43) is positive and can substantially increase η. A remarkable feature of retrograde discs is that they can extract energy from the black hole via a hydrodynamic analog of Penrose process. This occurs if $a_\star$ is close to -1; in such discs $u_t(r_h) < 0$ and $\eta > 1$. The maximum $\eta = 1.1$ is reached when $a_\star = -1$ and $l_0 = l_{\rm cr}(-1) = 3.15 r_g c$. It has to be noted that we have neglected the back-reaction of radiation on the dynamics of the flow, this approximation breaks down when $\eta \simeq 1$.

Next, we evaluated numerically the efficiency $\eta_{\rm esc}$ that takes into account the capture of the produced radiation into the black hole (Fig. 2.8). This effect greatly reduces the observed luminosity. The reduction is especially significant for retrograde discs because their radiation is Doppler-beamed in the direction opposite to the black hole rotation, so most of their radiation misses the escape cones shown in Figure B.1. The resulting efficiency $\eta_{\rm esc}$ is highest for prograde discs around maximally rotating black holes ($a_\star = 1$). The maximum $\eta_{\rm esc}$ is close to 10 per cent.

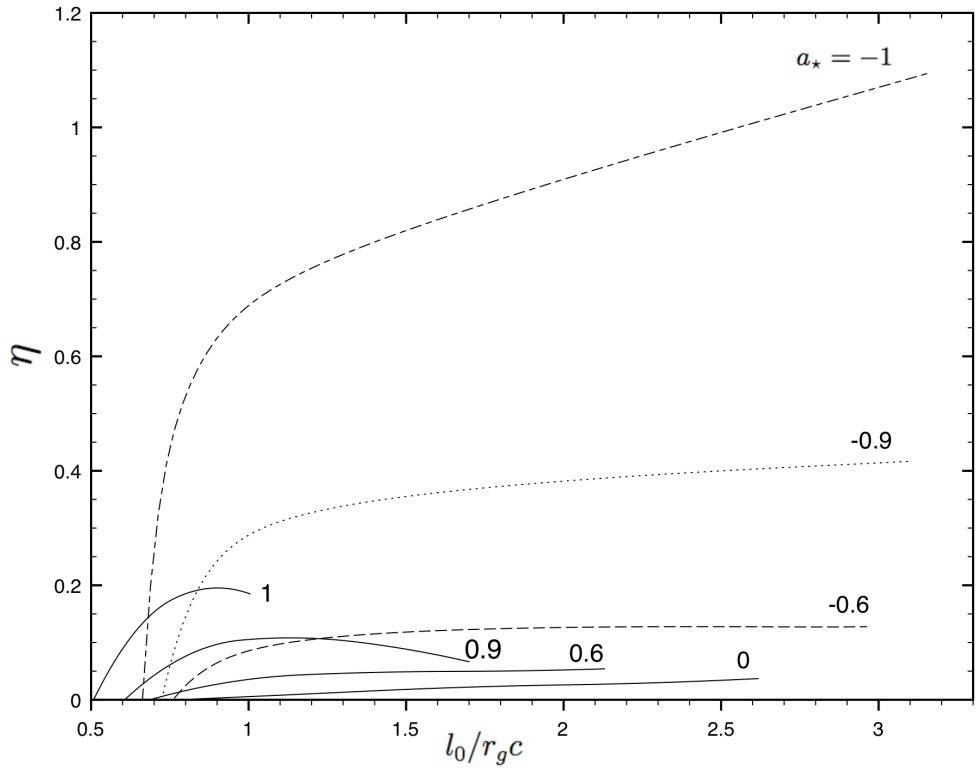

Figure 2.7: Radiative efficiency as a function of l_0, ignoring the light capture into the black hole. Seven curves are plotted for black holes with different spin parameters $a_\star$. Solid curves are used for $a_\star \geqslant 0$ and broken curves for $a_\star < 0$.

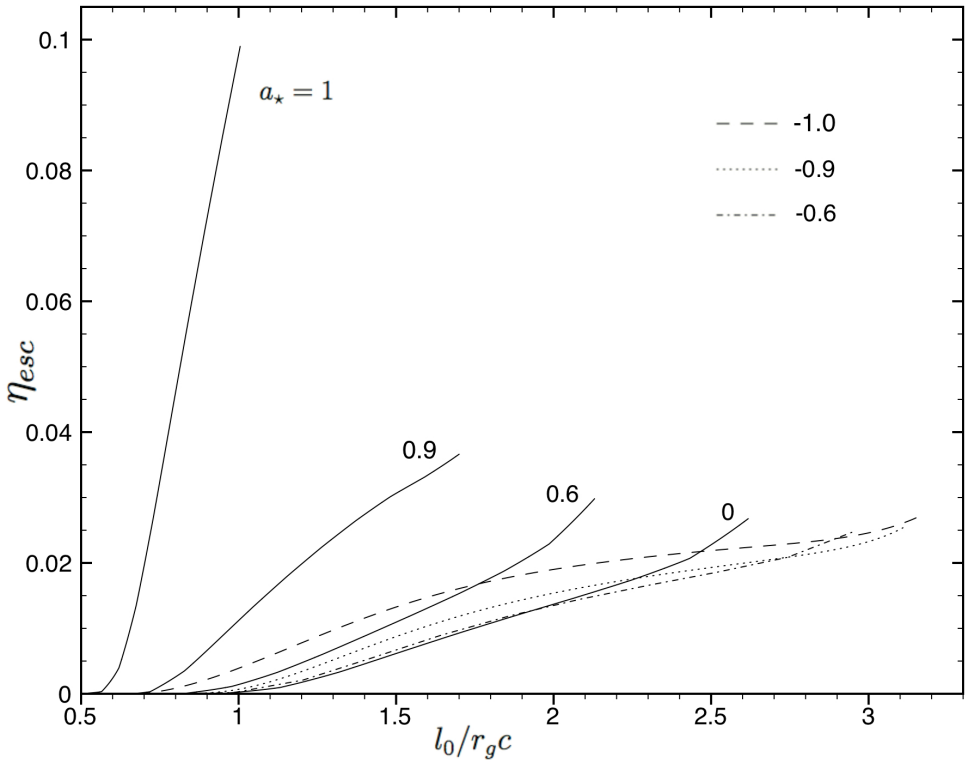

Figure 2.8: Same as Fig. 2.7 but taking into account the suppression of radiative efficiency due to light capture into the black hole.

2.5 Conclusions

In our model, the mini-disc is completely described by two parameters: the maximum angular momentum of the accreting gas l_0 and the spin parameter of the black hole $a_\star$. $l_0 = 0$ corresponds to spherical accretion. The inviscid mini-disc forms when l_0 is in the range $l_\star(a_\star) < l_0 < l_{\rm cr}(a_\star)$ shown in Fig. 2.4.

When the black hole rotates in the same direction as the accretion flow ($a_\star > 0$), this range becomes smaller compared to the Schwarzschild case and the maximum possible size of the mini-disc is reduced. For example, for the typical $a_\star \sim 0.9$ expected in collapsars we find $l_{\rm cr} \approx 1.5 r_g c$, which corresponds to a disc of radius $r_d \approx 6 r_g = 12GM/c^2$. The mini-disc model may describe collapsars at the early stage when the disc grows from the black hole horizon r_h to $\sim 12GM/c^2$; then it must switch to the standard viscous regime.

We have calculated the radiative efficiency of mini-discs taking into account the effect of photon (or neutrino) capture into the black hole (Fig. 2.8). The efficiency is maximum when the mini-disc has its maximum size, near the transition to the viscous-disc regime. For prograde discs around rapidly rotating black holes, the efficiency approaches 0.1, which is ~ 3 times higher than for non-rotating black holes.

We have also studied the case of retrograde discs, where the disc and the black hole are counter-rotating ($a_\star < 0$). Such discs can form in wind-fed X-ray binaries where gas accretes with alternating angular momentum due to fluctuations and 'flip-flop' instability (e.g. [Shapiro and Lightman, 1976] ; [Blondin and Pope, 2009] and refs. therein). We find that a hydrodynamic analog of Penrose process works in such discs if $a_\star$ is close to -1, i.e. the black hole is close to maximum rotation. Then the black hole accretes matter with negative orbital energy, which means that energy is extracted from the black hole. However, if the extracted energy is radiated quasi-isotropically in the disc rest-frame, most of the produced radiation ends up inside the black hole, and the escaping luminosity is suppressed.

Chapter 3

Neutrino heating near hyper-accreting black holes

Ivan Zalamea, Andrei M. Beloborodov

[Published in MNRAS, 410:2302–2308, February 2011]

Hyper-accretion discs around black holes emit copious neutrinos and anti-neutrinos. A fraction of the emitted neutrinos convert to electron-positron plasma above the disc through the annihilation reaction $\nu\bar{\nu} \rightarrow e^+e^-$. This process may drive relativistic jets associated with GRB explosions. We calculate the efficiency of energy deposition by neutrinos. Our calculation is fully relativistic and based on a geodesic-tracing method. We find that the efficiency of neutrino heating is a well-defined function of (i) accretion rate and (ii) spin of the black hole. It is practically independent of the details of neutrino transport in the opaque zone of the disc. The results help identify accretion discs whose neutrino emission can power GRBs.

3.1 Introduction

A plausible model for the central engines of gamma-ray bursts (GRBs) pictures a transient, hyper-accreting disc formed around a rotating black hole (e.g. [Narayan

et al., 2001], see [Beloborodov, 2008] for a review). The disc is a source of copious neutrinos and anti-neutrinos, which partially annihilate above the disc and turn into $e^{\pm}$ pairs, $\nu + \bar{\nu} \rightarrow e^{-} + e^{+}$. This process was proposed as a possible mechanism for creating relativistic, $e^{\pm}$-dominated jets that could power observed GRBs [Eichler *et al.*, 1989]. However, its efficiency remained unsettled. Its accurate calculation requires a detailed relativistic model for the neutrino source — the accretion disc — as well as tracing the neutrino propagation in the Kerr spacetime of the black hole.

A detailed relativistic model for GRB discs was completed recently ([Chen and Beloborodov, 2007], hereafter CB07). It describes the disc down to its inner edge and gives accurate energy fluxes carried away by ν and $\bar{\nu}$ at all radii r. In the present work we trace the neutrino trajectories and calculate the rate of $\nu\bar{\nu}$ annihilation around the disc. Neutrino annihilation was previously calculated in a number of works (e.g. [Popham *et al.*, 1999]; [Asano and Fukuyama, 2001]; [Birkl *et al.*, 2007]). Our work has three motivations: (i) A relativistic calculation of $\nu\bar{\nu}$ annihilation has never been done for a realistic accretion disc around a spinning black hole. Previous works either used a toy model for neutrino source (e.g. [Birkl *et al.*, 2007]) or replaced neutrino trajectories by straight lines [Popham *et al.*, 1999]. (ii) The efficiency of $\nu\bar{\nu}$ annihilation strongly depends on the accretion rate $\dot{M}$ and the spin parameter a of the black hole. It is desirable to know this dependence and identify the range of $\dot{M}$ and a where $\nu\bar{\nu}$ annihilation can provide the observed energy of GRB explosions. (iii) In addition to $\nu\bar{\nu}$ annihilation, neutrinos can create $e^{\pm}$ pairs off magnetic field [Kuznetsov and Mikheev, 1997]; [Gvozdev and Ognev, 2001]). The contribution of this process to the energy deposition rate should be included.

The paper is organized as follows. Section 3.2 describes the setup and method of our calculations. The results are presented in Section 3.3 and summarized in Section 4.

3.2 Model description

Neutrinos emitted by the disc follow geodesics in Kerr spacetime. The efficiency ϵ of their annihilation can be calculated numerically by tracing the geodesics, evaluating the local energy deposition rate [erg s^{-1} cm^{-3}] everywhere around the black hole and then integrating over volume outside the disc to obtain the net energy deposition rate $\dot{E}_{\nu\bar{\nu}}$ (energy at infinity per unit time at infinity).

The neutrino emission and annihilation is concentrated near the black hole, where the accretion time-scale is short and $\dot{M}$ may be assumed to be quasi-steady. Then $\dot{E}_{\nu\bar{\nu}}$ depends on four parameters that specify the steady disc model: accretion rate $\dot{M}$, viscosity parameter α, mass of the black hole M, and spin of the black hole a.

3.2.1 Neutrino source: disc model

As the disc matter spirals into the black hole, it is viscously heated: the gravitational energy is converted to heat. Part of the heat is lost to neutrino emission, and part is stored in the disc and distributed between nuclear matter, radiation, and $e^{\pm}$ pairs, in perfect thermodynamic and nuclear statistical equilibrium. The equilibrium microphysics is determined by only three parameters: temperature T, baryon mass density ρ, and electron fraction Y_e (equal to the charged nucleon fraction). Other parameters — e.g. the electron chemical potential μ_e and density of $e^{\pm}$ pairs $n_{\pm}$ — are derived from T, ρ and Y_e.

The neutrino emission peaks in the inner region of the disc. The far dominant emission mechanism is the e^-/e^+ capture onto protons/neutrons,

$$e^- + p \rightarrow n + \nu_e, \qquad e^+ + n \rightarrow p + \bar{\nu}_e. \tag{3.1}$$

The neutrino-cooled discs are nearly in β-equilibrium: the rates of the two reactions in equation (3.1) are practically equal, which determines the value of $Y_e(\rho, T)$ ([Imshennik *et al.*, 1967]; [Beloborodov, 2003]). In principle, all three flavors of neutrinos

could be emitted from the disc, but only electron neutrinos need to be considered; the emission rates for muon and tau neutrinos are negligible (CB07).

A detailed model for neutrino-cooled relativistic discs was developed in CB07, and we use their model in our calculations. The approximate hydrodynamic disc equations are solved with the vertically-integrated α prescription. The equations include radial transport of heat and lepton number. Local microphysics is treated exactly: nuclear composition, electron degeneracy, neutrino emissivity and opacity etc., using the equilibrium distribution functions for all species except neutrinos. Neutrinos are modeled separately in the opaque and transparent zones of the disc, matching at the transition between the two zones.

The disc model provides the vertically averaged T, ρ, Y_e, μ_e (which are approximately equal to their values in the midplane $\theta = \pi/2$) and the half-thickness of the disc H. The ν and $\bar{\nu}$ spectra emitted from the neutrino-transparent (optically thin) zone of the disc are given by

$$\begin{aligned} f(E) &\equiv h^3 \frac{dN_\nu}{\mathrm{d}^3x\,\mathrm{d}^3p} \\ &= \frac{\lambda^3 K H \rho Y_e}{\pi m_p c} \frac{(E+q)\sqrt{(E+q)^2-1}}{e^{(E+q-\mu_e)/\Theta}+1} \end{aligned} \tag{3.2}$$

for neutrinos ($E > 0$), and

$$\begin{aligned} f'(E) &\equiv h^3 \frac{dN_{\bar{\nu}}}{\mathrm{d}^3x\,\mathrm{d}^3p} \\ &= \frac{\lambda^3 K H \rho (1-Y_e)}{\pi m_p c} \frac{(E-q)\sqrt{(E-q)^2-1}}{e^{(E-q+\mu_e)/\Theta}+1} \end{aligned} \tag{3.3}$$

for anti-neutrinos ($E > q+1$). Here $h = 2\pi\hbar$, $\lambda = h/m_e c$, $q = (m_n - m_p)/m_e = 2.53$, $K = 6.5 \times 10^{-4} s^{-1}$, $\Theta = kT/m_e c^2$, μ_e is electron chemical potential in units of $m_e c^2$ and E is neutrino/anti-neutrino energy in units of $m_e c^2$.

The spectra emerging from the opaque zone are controlled by neutrino transport through the disc, which cannot be reliably calculated — it depends on the unknown vertical distribution of viscous heating. Fortunately, the $\nu\bar{\nu}$ annihilation rate depends

only on the *energy fluxes* F_ν and $F_{\bar{\nu}}$ from the disc surface, which are insensitive to the neutrino-transport details. This fact has a simple analytical explanation [Beloborodov, 2008]. It follows from the proportionality $\sigma_{\nu\bar{\nu}} \propto E_\nu E_{\bar{\nu}}$, where $\sigma_{\nu\bar{\nu}}$ is the cross-section for annihilation for neutrino and anti-neutrinos with energies E_ν and $E_{\bar{\nu}}$.

To demonstrate that the rate of $\nu\bar{\nu}$ annihilation depends on F_ν and $F_{\bar{\nu}}$ but not on the exact shapes of ν and $\bar{\nu}$ spectra, we consider below two extreme models A and B, and they give practically the same annihilation rates:

Model A: Neutrinos and anti-neutrinos are emitted with the same spectra as found *inside* the disc. The spectra are normalized so that the emerging emission carries away the known energy fluxes F_ν and $F_{\bar{\nu}}$. In the opaque region, the spectra of ν and $\bar{\nu}$ are described by Fermi-Dirac distributions. The temperature and chemical potential for ν and $\bar{\nu}$ inside the disc are obtained from the numerical models of CB07.

Model B: Neutrinos and anti-neutrinos are emitted with a thermal spectrum with zero chemical potential and temperature $T = T_{\rm eff}$, where $T_{\rm eff}$ is the effective surface temperature defined by $(7/8)\sigma T_{\rm eff}^4 = F_\nu + F_{\bar{\nu}}$ (σ is the Stefan-Boltzmann constant and the coefficient 7/8 takes into account the difference between statistics of photons and ν, $\bar{\nu}$).

When the disc is efficiently cooled (neutrino energy flux almost balances viscous heating), $T_{\rm eff}$ is given by the standard thin-disc model of [Page and Thorne, 1974]: $T_{\rm eff} \approx T_{\rm eff}^{\rm st}$. This regime occurs in a broad range of accretion rates $\dot{M}_{\rm ign} < \dot{M} < \dot{M}_{\rm trap}$ (CB07). If $\dot{M} < \dot{M}_{\rm ign}$, the disc temperature is not high enough to ignite the neutrino emitting reactions. If $\dot{M} > \dot{M}_{\rm trap}$, the emitted neutrinos become trapped in the disc and advected into the black hole. Our third (simplest) model for the neutrino source is defined as follows.

Model C: Neutrinos and anti-neutrinos are emitted with a thermal spectrum

that has zero chemical potential and the following temperature,

$$T_{\rm eff}(\dot{M},r) = T_{\rm eff}^{\rm st}(\dot{M}_{\rm ign},r) \times \begin{cases} 0 & \dot{M} < \dot{M}_{\rm ign} \\ (\dot{M}/\dot{M}_{\rm ign})^{1/4} & \dot{M}_{\rm ign} < \dot{M} < \dot{M}_{\rm trap} \\ (\dot{M}_{\rm trap}/\dot{M}_{\rm ign})^{1/4} & \dot{M} > \dot{M}_{\rm trap} \end{cases} \tag{3.4}$$

This model does not even require the calculation of the disc structure as $T_{\rm eff}^{\rm st}$ is a known analytical function of r (Page & Thorne 1974). As we show below, this simplest model gives remarkably accurate result for $\dot{E}_{\nu\bar{\nu}}$.

The characteristic accretion rates $\dot{M}_{\rm ign}$ and $\dot{M}_{\rm trap}$ depend on the viscosity parameter α. They were calculated in CB07, and the numerical results are well approximated by the following formulae,

$$\dot{M}_{\rm ign} = K_{\rm ign}\left(\frac{\alpha}{0.1}\right)^{5/3}, \qquad \dot{M}_{\rm trap} = K_{\rm trap}\left(\frac{\alpha}{0.1}\right)^{1/3}. \tag{3.5}$$

The coefficients $K_{\rm ign}$ and $K_{\rm trap}$ are functions of the black-hole spin a. For $a = 0$, $K_{\rm ign} = 0.071 M_\odot s^{-1}$ and $K_{\rm trap} = 9.3 M_\odot s^{-1}$. For $a = 0.95$, $K_{\rm ign} = 0.021 M_\odot s^{-1}$ and $K_{\rm trap} = 1.8 M_\odot s^{-1}$.

In all three models A, B and C the neutrino emission is assumed to be isotropic in the local rest frame of the disc (which is in Keplerian rotation around the black hole).

3.2.2 Neutrino transport

To evaluate the $\nu\bar{\nu}$ annihilation rate at a given point we need to know the local ν and $\bar{\nu}$ distribution functions. They can be obtained using the known neutrino distribution functions at the surface of the disc. To a first approximation, neutrinos obey the collisionless Boltzmann equation, because most of them do not participate in any interactions (and eventually escape to infinity or get captured into the black hole). The Boltzmann equation in curved spacetime has the same form as in flat spacetime.

It states that the phase-space density (or occupation number) of neutrinos remains constant along their trajectories,

$$\frac{df(x^\mu(\lambda), p^\mu(\lambda))}{d\lambda} = 0. \tag{3.6}$$

Here $x^\mu(\lambda)$ is a parameterized worldline for a ν or $\bar{\nu}$. The neutrinos emitted by the disc have huge energies compared to their rest mass and we treat them as massless particles propagating along null geodesics in Kerr spacetime. We use Boyer-Lindquist coordinates $x^\alpha = (t, \phi, r, \theta)$, where the Kerr metric has the form,

$$ds^2 = g_{tt}dt^2 + 2g_{t\phi}dtd\phi + g_{\phi\phi}d\phi^2 + g_{rr}dr^2 + g_{\theta\theta}d\theta^2. \tag{3.7}$$

The metric tensor $g_{\alpha\beta}$ is specified by two parameters: $r_g = 2GM/c^2$ and the spin parameter $|a| < 1$; it is given in e.g. [Chandrasekhar, 1992].

Equation (3.6) is covariant and its solution takes into account Doppler and gravitational redshifts. The null geodesics in Boyer-Lindquist coordinates are described by the known ordinary differential equations of first order (e.g. [Chandrasekhar, 1992]) which we solve numerically.

Figure 3.1 shows the image of the accretion disc observed from three locations near the black hole. Colour represents the redshift (or blueshift) of neutrinos as they propagate from the emission point on the disc to the observation point. The asymmetry of the images is caused by the rotation of the black hole.

3.2.3 Local rates of $e^\pm$ creation

3.2.3.1 Reaction $\nu\bar{\nu} \to e^+e^-$

The rate of $\nu\bar{\nu}$ annihilation at a given point depends only on the local momentum distribution of ν and $\bar{\nu}$. We use the phase-space occupation number to describe this distribution; it is denoted by f for neutrinos and by f' for anti-neutrinos. The local energy-momentum deposition rate is given by (see e.g. [Birkl *et al.*, 2007],

$$Q^\alpha_{\nu\bar{\nu}} = \int \frac{\mathrm{d}^3p}{h^3}\frac{\mathrm{d}^3p'}{h^3} A(p,p')\,(p^\alpha + p'^\alpha)\,f(p)f'(p'), \tag{3.8}$$

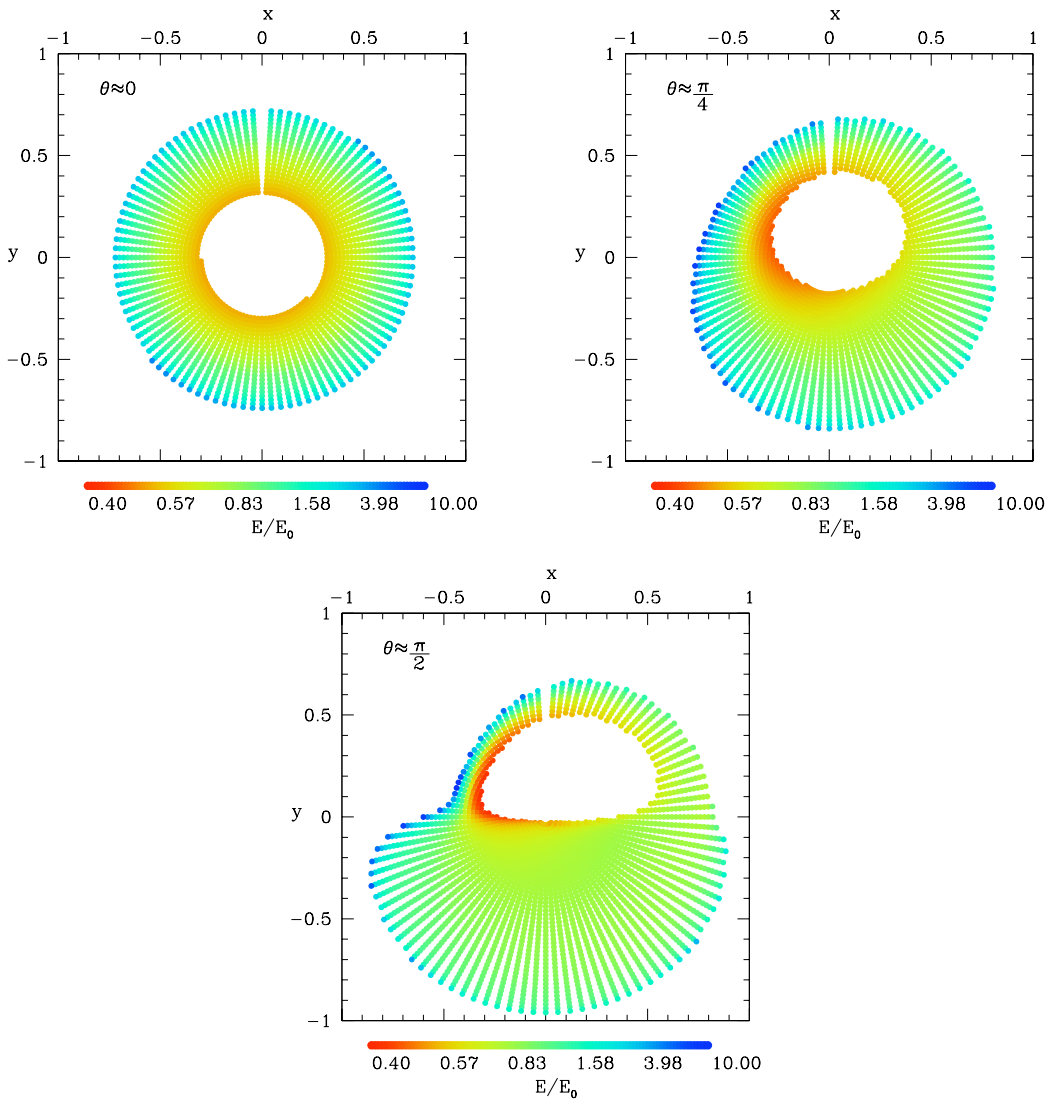

Figure 3.1: Projection of the sky for three different observers receiving neutrinos from a disc of radius $140r_h$. The colour codes the ratio of the energy at reception to the energy at emission for neutrinos, as measured in the local ZAMO frames (Section 2.4). All three observers are located at 3.1 horizon radii r_h around a black hole of spin $a = 0.95$. Their θ positions are approximately 0, $\pi/4$ and $\pi/2$. The observer sky is parameterized with two angles $\alpha \in (0, \pi)$ and $\beta \in (0, 2\pi)$ in the ZAMO frame. The axis $\alpha = 0$ points into the black hole and $\alpha = \pi$ points away from the black hole. The x and y coordinates in the figure are $(x, y) = (\frac{\alpha}{\pi} \sin\beta, \frac{\alpha}{\pi} \cos\beta)$.

where

$$A(p,p') = \frac{\sigma_0 c^2}{4}\Big[C_1 \frac{p^0 p'^0}{m_e^2 c^2}(1-\cos\theta)^2 + C_2(1-\cos\theta)\Big], \tag{3.9}$$

where p and p' are the four-momenta of neutrino and anti-neutrino, θ is the angle between the spatial (3D) components of p and p', $\sigma_0 = 4m_e^2 G_{\rm F}^2/\pi\hbar^4 \approx 1.71\times10^{-44}{\rm cm}^2$, $G_{\rm F}$ is Fermi constant, $C_1 = 0.78$ and $C_2 = 1.06$. We neglect the mass of ν and $\bar{\nu}$, i.e. assume $p^\alpha p_\alpha = 0$ and $p'^\alpha p'_\alpha = 0$.

3.2.3.2 Reaction $\nu \to \nu e^+ e^-$ in a strong magnetic field

Neutrinos propagating in a strong magnetic field B can create electron-positron plasma through the process $\nu \to \nu e^+ e^-$ ([Kuznetsov and Mikheev, 1997]; [Gvozdev and Ognev, 2001]). A neutrino with four-momentum p^α and energy E deposits energy-momentum into the $e^\pm$ plasma with the following rate

$$q^\alpha = \frac{7(c_v^2+c_a^2)}{1728\pi^2}\,\frac{\sigma_0}{\hbar}\,(eB\sin\psi)^2 \ln\left(\frac{\hbar p^0 eB\sin\psi}{m_e^3 c^4}\right)\frac{p^0 p^\alpha}{(m_e c)^2}, \tag{3.10}$$

where ψ is the angle between the magnetic field and the neutrino momentum, $c_v \approx 0.96$ and $c_a = 1/2$. The local energy-momentum deposition rate via reactions $\nu \to \nu e^+ e^-$ and $\nu' \to \nu' e^+ e^-$ is given by

$$Q^\alpha_{\nu B} = \int \frac{{\rm d}^3 p}{h^3}\,[f(p) + f'(p)]\; q^\alpha(p). \tag{3.11}$$

3.2.4 Integration of the energy deposition rate over volume

The local energy-momentum deposition rates (eqs. 3.8 and 3.11) can be calculated in any frame of reference. We chose the frame of Zero Angular Momentum Observer, ZAMO. These observers do not move in r or θ directions. Their ϕ motion corresponds to zero angular momentum ($p_\phi = 0$). We use ZAMO frames because they are well defined everywhere outside the black-hole horizon (no observers can be static in Boyer-Lindquist coordinates inside the ergosphere). The local orthonormal coordinates of

ZAMO, $d\tilde{x}^\alpha$, are related to $dx^\alpha = (dt, d\phi, dr, d\theta)$ by

$$d\tilde{x}^\alpha = \mathcal{A}^\alpha_{\ \beta}\, dx^\beta, \tag{3.12}$$

where

$$\mathcal{A} = \begin{pmatrix} \sqrt{-g_{tt} + (g_{t\phi})^2/g_{\phi\phi}} & 0 & 0 & 0 \\ g_{t\phi}/\sqrt{g_{\phi\phi}} & \sqrt{g_{\phi\phi}} & 0 & 0 \\ 0 & 0 & \sqrt{g_{rr}} & 0 \\ 0 & 0 & 0 & \sqrt{g_{\theta\theta}} \end{pmatrix}.$$

$\det\mathcal{A} = \sqrt{-g}$ and the element of four-dimensional volume measured by ZAMO $d\tilde{V}$ is related to the Boyer-Lindquist coordinate volume $dV = dt\, d\phi\, dr\, d\theta$ by

$$d\tilde{V} = \sqrt{-g}\, dt\, d\phi\, dr\, d\theta. \tag{3.13}$$

Let $d\tilde{P}^\alpha = Q^\alpha d\tilde{V}$ be four-momentum deposited in $d\tilde{V}$ as measured by ZAMO. The deposited energy measured by a distant observer is $dE = -c\, dP_t$. It can be expressed in terms of $d\tilde{P}^\alpha$,

$$\frac{dE}{c} = -g_{tt} dP^t - g_{t\phi} dP^\phi = \frac{d\tilde{P}^t}{\sqrt{-g^{tt}}} - \frac{g_{t\phi}}{\sqrt{g_{\phi\phi}}}\, d\tilde{P}^\phi, \tag{3.14}$$

where we used the transformation $d\tilde{P}^\alpha = \mathcal{A}^\alpha_{\ \beta} dP^\beta$. This yields

$$dE = \left(\frac{Q^t}{\sqrt{-g^{tt}}} - \frac{g_{t\phi}}{\sqrt{g_{\phi\phi}}}\, Q^\phi \right) \sqrt{-g}\, dt\, d\phi\, dr\, d\theta. \tag{3.15}$$

The net energy deposition rate outside the horizon dE/dt (measured by a distant observer) is given by

$$\dot{E} = \int_{r>r_h} \left(\frac{Q^t}{\sqrt{-g^{tt}}} - \frac{g_{t\phi}}{\sqrt{g_{\phi\phi}}}\, Q^\phi \right) \sqrt{-g}\, d\phi\, dr\, d\theta, \tag{3.16}$$

where r_h is the horizon radius.

3.2.5 Numerical Method

We compute the local rates of four-momentum deposition Q^α on a spatial grid. The problem is axially symmetric and the grid is set on the (r, θ) plane. It covers the region $r_h < r < r_{\rm max}$ and $0 < \theta < \pi/2$ (we use the symmetry about the equatorial plane $\theta = \pi/2$). The radius $r_{\rm max}$ is chosen between $26r_h$ and $38r_h$, depending on the black hole spin. The grid has 25×20 points. Its spacing is logarithmic in the r-direction and uniform in the θ-direction.

We calculate Q^α according to equations (3.8) and (3.11). The distributions $f(p)$ and $f'(p')$ are Lorentz-invariant (scalar) functions of four-momentum. They remain constant along the neutrino trajectories (eq. 3.6). Therefore, to calculate $f(p)$ measured by ZAMO at a given point, it is sufficient to trace the neutrino with momentum p back to its emission point, find its four-momentum there in the rest-frame of the disc, $p_{\rm em}$, and use the equality $f(p) = f_{\rm em}(p_{\rm em})$. The values of $f_{\rm em}(p_{\rm em})$ and $f'_{\rm em}(p'_{\rm em})$ are provided by the disc models described in § 2.1.

For every point of the grid we trace back the neutrino trajectories for 5000 directions uniformly distributed on the local ZAMO sky. Each direction is followed until the geodesic reaches the disc, goes into the black-hole horizon or reaches a maximum radius that we set equal to $140r_h$. For trajectories coming from outside $140r_h$ or connecting to the horizon we set $f = f' = 0$. For trajectories connecting our grid point to the disc, we find f and f' as described above.

The accuracy of our calculation of Q^α can be estimated by doubling the number of sampled geodesics; it is a few per cent. The accuracy of the volume-integrated quantity $\dot{E}$ is controlled mainly by the number of grid points. We checked it by repeating the same calculation with a coarser grid; the estimated error in $\dot{E}$ is smaller than 10 per cent (Table 1).

		Half spatial resolution	Twice geodesics
Code accuracy	a=0	$\lvert\Delta\dot{E}/\dot{E}\rvert = 0.03$	$\lvert\Delta\dot{E}/\dot{E}\rvert = 5 \times 10^{-3}$
	a=0.95	$\lvert\Delta\dot{E}/\dot{E}\rvert = 0.07$	$\lvert\Delta\dot{E}/\dot{E}\rvert = 0.02$

Table 3.1: Fractional change of the energy deposition rate when the grid resolution is reduced from 500 to 240 points (left column), and when the number of geodesics is increased from 5×10^3 to 10^4 (right column).

3.2.6 Comparison with previous works

We compared our calculations with three previous works: [Birkl *et al.*, 2007], [Asano and Fukuyama, 2001] and [Popham *et al.*, 1999].

[Birkl *et al.*, 2007] calculated $Q^{\alpha}_{\nu\bar{\nu}}$ and the corresponding volume-integrated energy deposition rate $\dot{E}_{\nu\bar{\nu}}$ outside the ergosphere for several toy models of the neutrino source. They traced exactly the neutrino trajectories in the Kerr metric. Unfortunately, they incorrectly computed $\dot{E}_{\nu\bar{\nu}}$ by integrating dP^t instead of $-dP_t$. For test purposes we did a similar integration. We computed their models D and REF, which assume that neutrinos are emitted by an isothermal blackbody ring (see Table 1 in [Birkl *et al.*, 2007]). The results agreed within the numerical errors of their and our calculations.

[Asano and Fukuyama, 2001] calculated $\dot{E}_{\nu\bar{\nu}}$ on the rotational axis in Kerr metric as a function of r. The neutrino source was modeled as a blackbody disc with the temperature having a power-law dependence on radius. For test purposes, we repeated the calculation for their isothermal disc model and obtained $\dot{E}_{\nu\bar{\nu}}(r)$ on the axis. The functional shape of $\dot{E}_{\nu\bar{\nu}}(r)$ agrees with the shape of function $G(r)$ in [Asano and Fukuyama, 2001] (see their eq. 18).

[Popham *et al.*, 1999] made more realistic assumptions about the neutrino source, similar to our Model C (Section 2.1). They evaluated numerically $\dot{E}_{\nu\bar{\nu}}$ for several values of accretion rate $\dot{M}$ and black-hole spin a (see their Table 3). The neutrino

geodesics in Kerr metric were replaced by straight lines. When comparing their results with ours (which are presented in the next section) we found a significant disagreement, exceeding factor of 10. Generally, we find that $\dot{E}_{\nu\bar{\nu}}$ of Popham et al. (1999) was overestimated. The dependence of $\dot{E}_{\nu\bar{\nu}}$ on a that is suggested by Table 3 in [Popham *et al.*, 1999] is incorrect, apparently steeper than what we find numerically and estimate analytically (see next section).

3.3 Results

The two processes of $e^{\pm}$ creation considered in this paper (Section 2.3) give the total energy deposition rate $\dot{E} = \dot{E}_{\nu\bar{\nu}} + \dot{E}_{\nu B}$. We first focus on $\dot{E}_{\nu\bar{\nu}}$ and discuss the contribution $\dot{E}_{\nu B}$ separately in Section 3.2.

3.3.1 Energy deposition from $\nu\bar{\nu} \rightarrow e^+e^-$

Figures 3.2 and 3.3 show $Q^t_{\nu\bar{\nu}}$ for an accretion disc with $\dot{M} = 1M_\odot$ s^{-1} around a black hole of mass $M = 3M_\odot$. In Figure 3.2 the black hole is assumed to be rapidly rotating ($a = 0.95$), and in Figure 3.3 it is non-rotating ($a = 0$). In the case of $a = 0.95$, the deposition rate $Q^t_{\nu\bar{\nu}}$ peaks closer to the black hole and reaches much higher values, because the disc extends to smaller radii and emits a higher neutrino flux.

Volume integration of $Q^t_{\nu\bar{\nu}}$ and $Q^\phi_{\nu\bar{\nu}}$, as described by equation (3.16), gives the net energy deposition rate due to $\nu\bar{\nu}$ annihilation outside the black-hole horizon, $\dot{E}_{\nu\bar{\nu}}$. Figure 3.4 shows $\dot{E}_{\nu\bar{\nu}}$ as a function of the disc accretion rate $\dot{M}$ for the two cases, $a = 0$ and $a = 0.95$. For all $\dot{M}$, $\dot{E}_{\nu\bar{\nu}}$ is much higher when the black hole is rapidly rotating.

The results are sensitive to $\dot{M}$ and a, but remarkably insensitive to the details of the disc model.

(i) The uncertainty in the vertical structure of the accretion disc leads to a small uncertainty in $\dot{E}_{\nu\bar{\nu}}$ as illustrated by two extreme models described in Section 2.1:

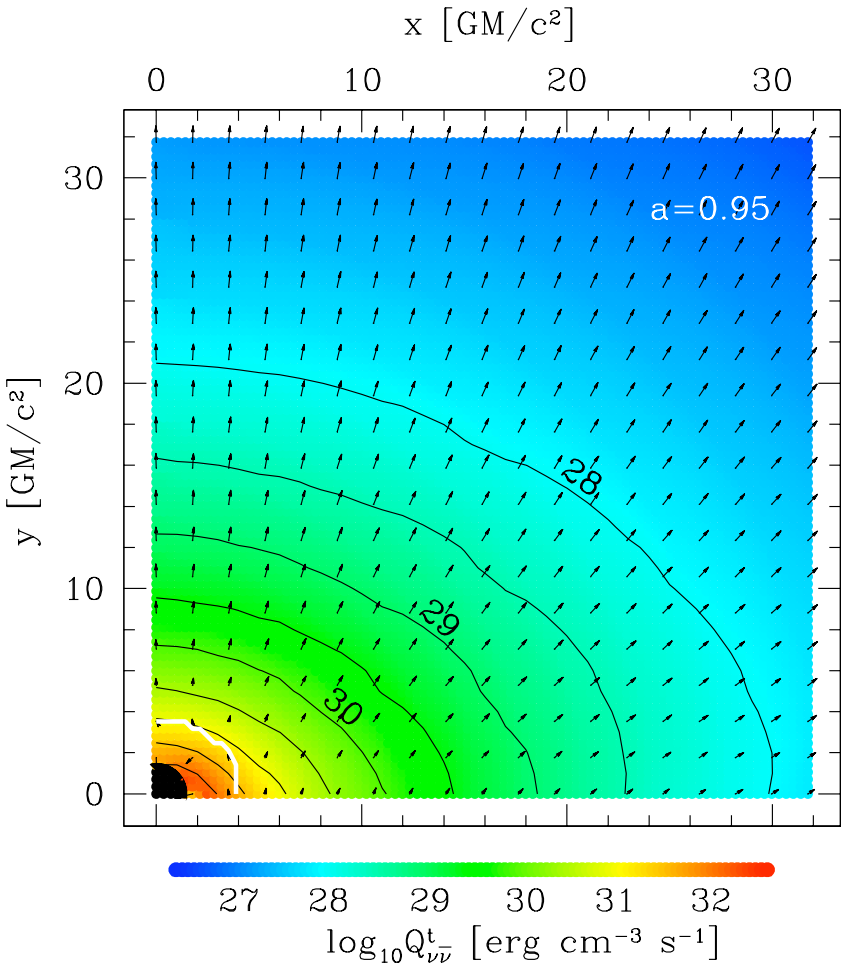

Figure 3.2: Color-coded and contour plot for $\log_{10} Q^t_{\nu\bar{\nu}}$ around an accretion disc with $\dot{M} = 1M_\odot/s$. The black hole has mass $M = 3M_\odot$ and spin parameter $a = 0.95$. The horizon sphere (black) has the radius $r_h \approx 1.3GM/c^2$, and the inner edge of the disc (the marginally stable orbit) is at $r_{\rm ms} \approx r_g = 2GM/c^2$. Arrows show the projection of $Q^i_{\nu\bar{\nu}}/Q^t_{\nu\bar{\nu}}$ on the plane of the figure. The white curve is where the radial component of injected momentum $Q^r_{\nu\bar{\nu}}$ changes sign. It roughly indicates the region where the deposited energy may be lost into the black hole rather than escape in an outflow. Disc Model A with viscosity parameter $\alpha = 0.1$ (Section 2.1) was used in the calculation. Practically the same $Q^t_{\nu\bar{\nu}}$ is found for Models B and C, and for different α (e.g. $\alpha = 0.01$).

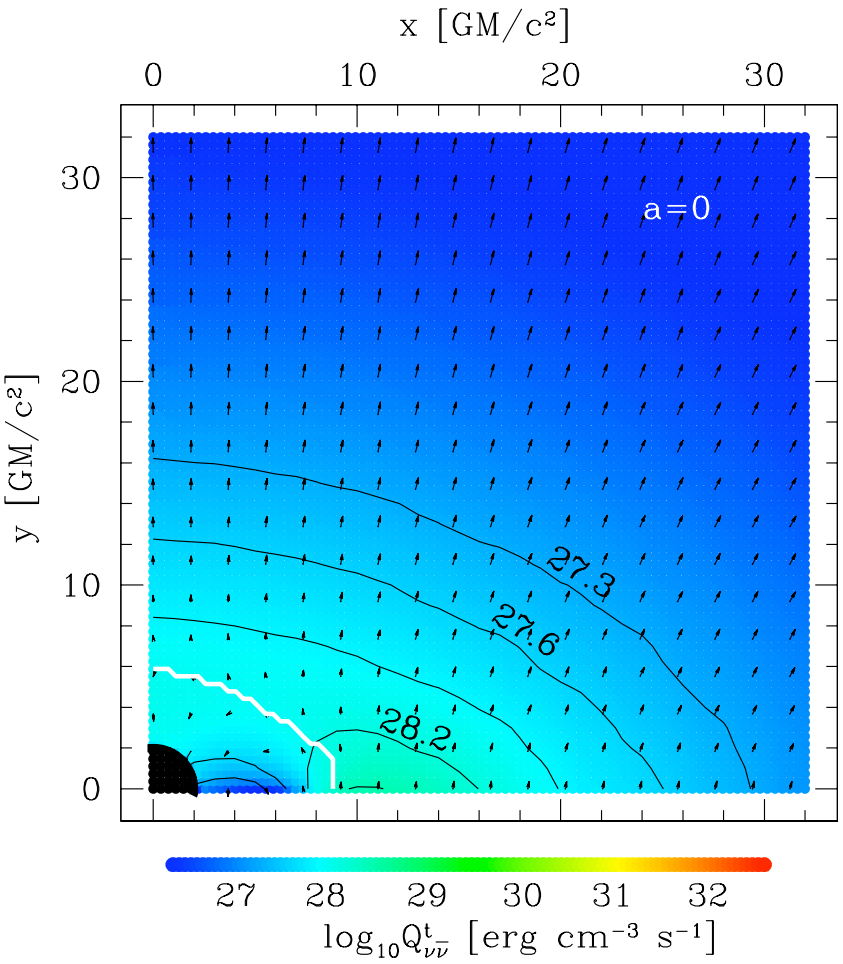

Figure 3.3: Same as Fig. 3.2 but for a non-rotating black hole, $a = 0$.

Model A and Model B. The results of both models are well approximated by simple Model C (eq. 3.4). Deviations of Model C from Model A arise mainly where Model C does not accurately predict the neutrino flux from the disc, i.e. where the disc is not strongly cooled by neutrino emission.

(ii) The uncertainty in viscosity parameter $\alpha \sim 0.1$ has almost no effect on $\dot{E}_{\nu\bar{\nu}}$ as long as $\dot{M}_{\rm ign} < \dot{M} < \dot{M}_{\rm trap}$. In particular, Model C in this range of $\dot{M}$ is explicitly independent of α. The two characteristic accretion rates $\dot{M}_{\rm ign}$ and $\dot{M}_{\rm trap}$ depend on viscosity parameter α (see eq. 3.5); in Figure 3.4 we assumed $\alpha = 0.1$.

The dependence of $\dot{E}_{\nu\bar{\nu}}$ on the black hole spin, for a fixed $\dot{M} = 1 M_{\odot}/s$, is shown in Figure 3.6. Instead of using the spin parameter a directly, it is more instructive to plot $\dot{E}_{\nu\bar{\nu}}$ versus radius of the last (marginally stable) orbit $r_{\rm ms}$. Then one can see the power-law dependence of $\dot{E}_{\nu\bar{\nu}}$ on $r_{\rm ms}$: $\dot{E}_{\nu\bar{\nu}} \propto r_{\rm ms}^{-4.8}$. This power-law is accurate for $r_{\rm ms} > r_g$ which corresponds to $a < 0.9$. For $r_{\rm ms} < r_g$, $\dot{E}_{\nu\bar{\nu}}$ has a somewhat stronger dependence on $r_{\rm ms}$. The standard relation between $r_{\rm ms}$ and a (e.g. Page & Thorne 1974) is shown in Figure 3.5. For non-rotating black holes $r_{\rm ms} = 6GM/c^2$ and for maximally rotating black holes $r_{\rm ms} = GM/c^2$.

3.3.2 Energy deposition from $\nu \to \nu e^+ e^-$ in a strong magnetic field

The four-momentum deposition due to reaction $\nu \to \nu e^+ e^-$ is given by equation (3.11). It depends on the magnetic field. We will assume the strongest field that could be expected,

$$\frac{B^2}{8\pi} = P_{\rm max}, \tag{3.17}$$

where $P_{\rm max}$ is the maximum pressure in the disc; we find this pressure using the numerical disc model of CB07. For illustration, consider a toy model where the magnetic field is perpendicular to the disc, uniform in the region $r < 25 r_h$ and zero outside this region. The model overestimates a realistic magnetic field around an

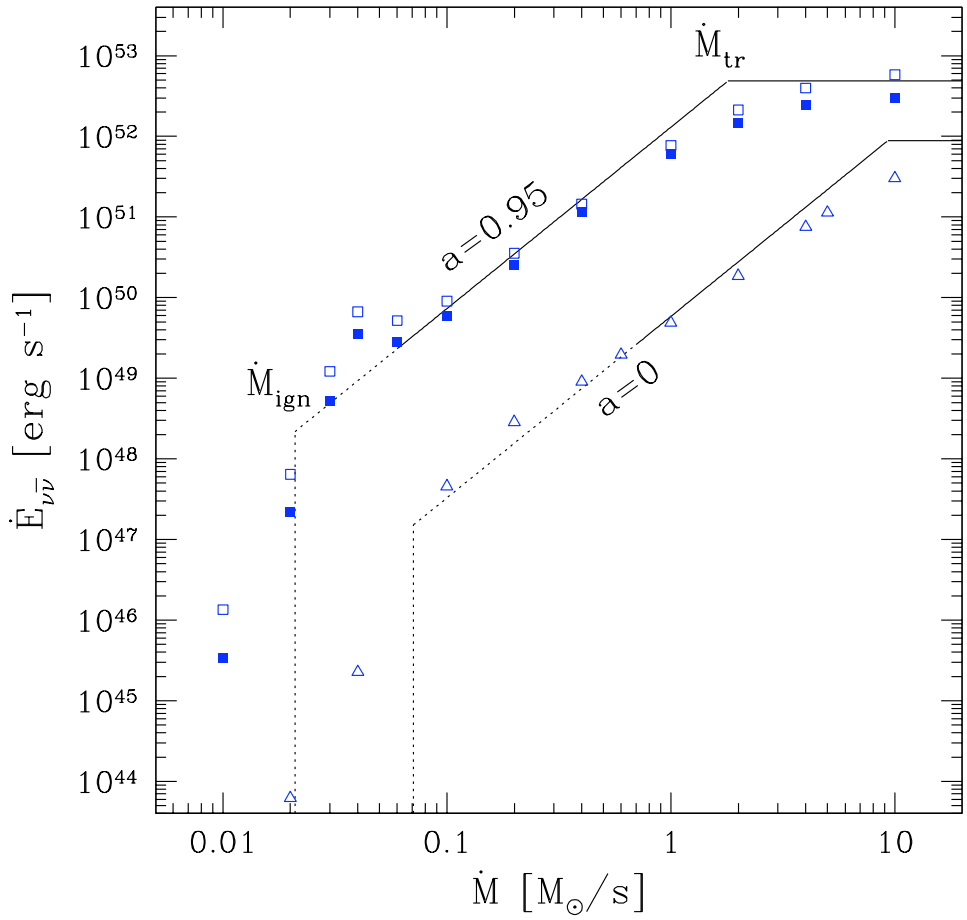

Figure 3.4: $\dot{E}_{\nu\bar{\nu}}$ as a function of $\dot{M}$ for a non-rotating black hole ($a = 0$) and for a rotating black hole ($a = 0.95$) of mass $M = 3M_\odot$. Open symbols show Model A and filled symbols show Model B (Section 2.1). The results of both models are well approximated by simple Model C, which is shown in the figure by lines; the line is dotted at low $\dot{M}$ where the disc is transparent to neutrinos.

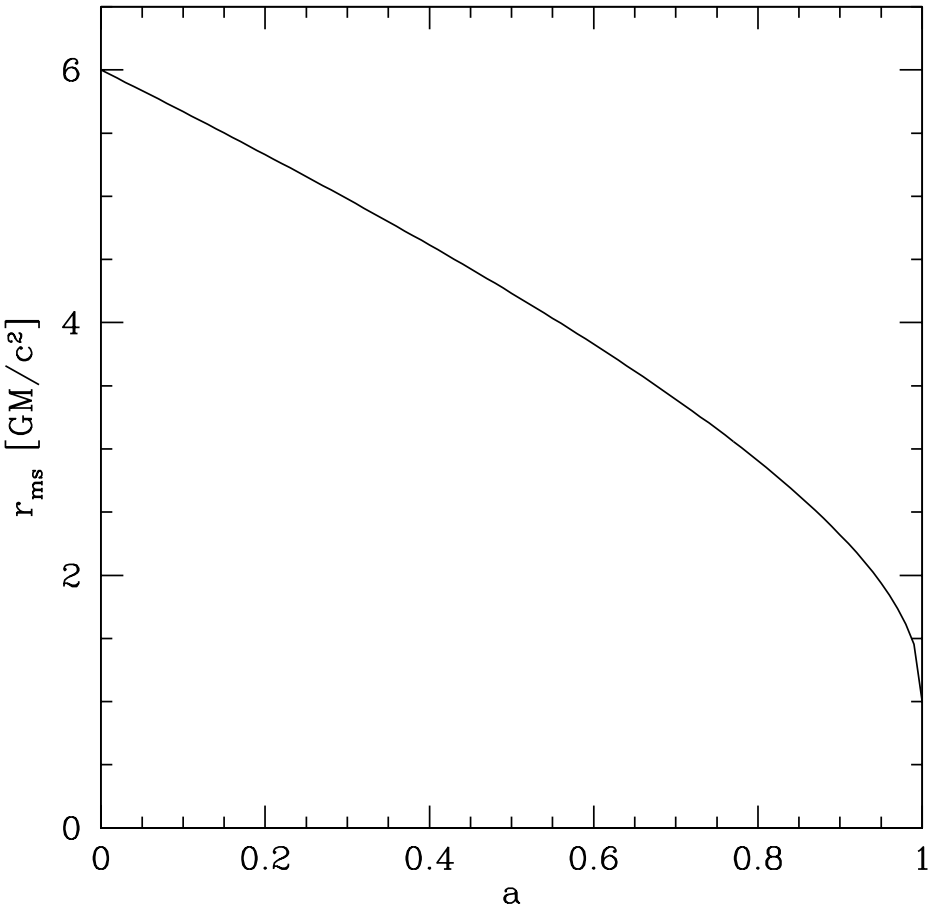

Figure 3.5: Radius of the marginally stable orbit, $r_{\rm ms}$, as a function of the black-hole spin parameter a.

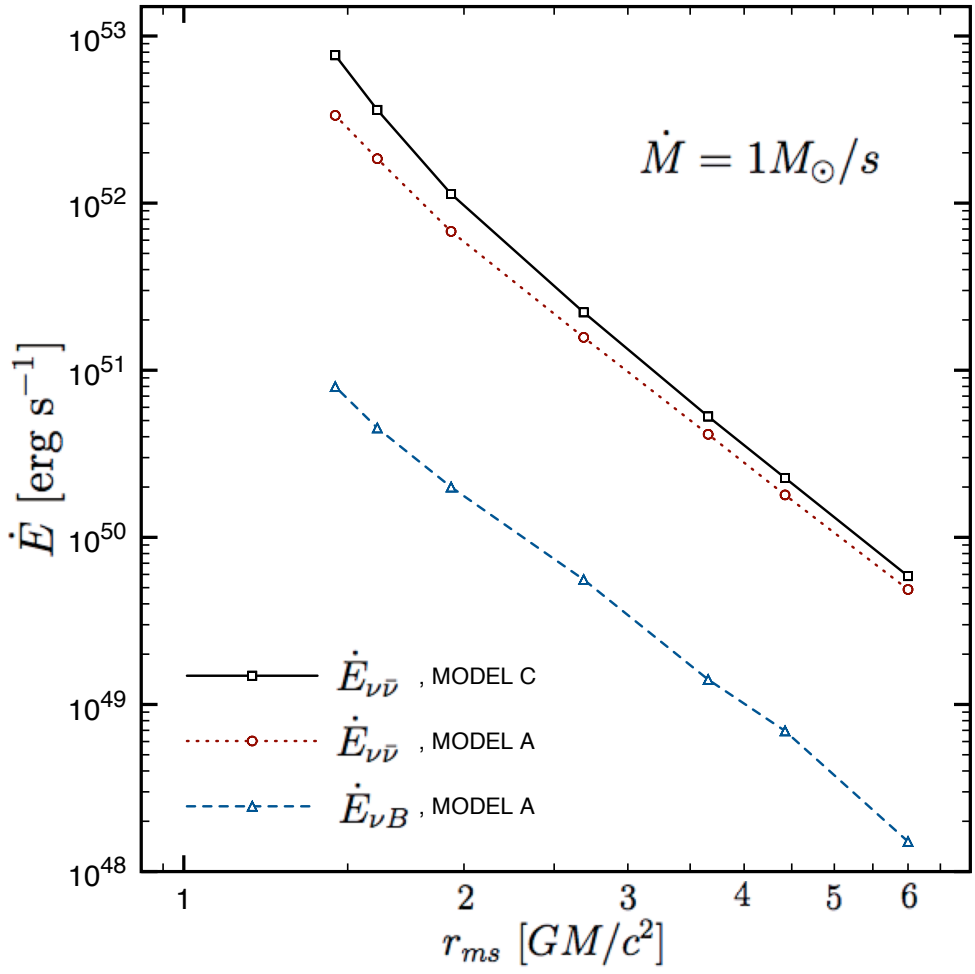

Figure 3.6: $\dot{E}_{\nu\bar{\nu}}$ and $\dot{E}_{\nu B}$ as functions of $r_{\rm ms}$ for fixed accretion rate, $\dot{M} = 1M_{\odot}/s$.

accretion disc. We will show that even such a strong field gives a modest $\dot{E}_{\nu B}$. The maximum pressure $P_{\max}$ and $B = (8\pi P_{\max})^{1/2}$ depend on $\dot{M}$ and a. The magnetic field ranges in our models from $\sim 6 \times 10^{13}$ G to $\sim 8 \times 10^{15}$ G, increasing with $\dot{M}$ and a.

Figure 3.6 shows $\dot{E}_{\nu B}$ as a function of $r_{\rm ms}$ for fixed $\dot{M} = 1 M_{\odot}/s$. It approximately follows the same scaling relation as we found for $\dot{E}_{\nu\bar{\nu}}(r_{\rm ms})$, $\dot{E}_{\nu B} \propto r_{ms}^{-4.8}$.

Figure 3.7 shows the ratio $\dot{E}_{\nu B}/\dot{E}_{\nu\bar{\nu}}$ as a function of $\dot{M}$. This ratio is small for accretion rates above $\dot{M}_{\rm ign}$ and varies slowly with $\dot{M}$ or a. Thus, we find that $\dot{E}_{\nu B}$ makes a small contribution to the total $\dot{E}$. This conclusion is valid for the most interesting range of accretion rates $\dot{M} > \dot{M}_{\rm ign}$. For $\dot{M} < \dot{M}_{\rm ign}$, the neutrino flux quickly decreases, which strongly suppresses the $\nu\bar{\nu}$ annihilation above the disc. The reduction in reaction $\nu \rightarrow \nu e^{+} e^{-}$ is less severe and $\dot{E}_{\nu B}$ exceeds $\dot{E}_{\nu\bar{\nu}}$. As a result, $\dot{E}_{\nu B}$ dominates the energy deposition rate $\dot{E}$ when $\dot{M}$ is below $\dot{M}_{\rm ign}$.

The dependence of the energy deposition rate on $\dot{M}$ is summarized in Figure 3.8, a modified version of Figure 3.4. It approximately represents the total $\dot{E}$ by showing $\dot{E}_{\nu\bar{\nu}}$ at $\dot{M} > \dot{M}_{\rm ign}$ and $\dot{E}_{\nu B}$ at $\dot{M} < \dot{M}_{\rm ign}$.

3.3.3 Scaling of $\dot{E}_{\nu\bar{\nu}}$ and $\dot{E}_{\nu B}$ with $\dot{M}$, M and $r_{\rm ms}$

The $\dot{E}_{\nu\bar{\nu}}$ dependence on $\dot{M}$, M and a may be estimated using simple analytical arguments [Beloborodov, 2008]. The total rate of $\nu\bar{\nu}$ annihilation around the disc $\dot{N}_{\nu\bar{\nu}}$ [$\rm s^{-1}$] is proportional to the volume of the main annihilation region r^3, which scales as $r_{\rm ms}^3$, and to the typical local annihilation rate in this region, $\dot{n}_{\nu\bar{\nu}} \sim \sigma c n_{\nu} n_{\bar{\nu}}$. Here n_{ν} and $n_{\bar{\nu}}$ are the number densities of neutrinos and anti-neutrinos and σ is the annihilation cross-section. The cross-section scales with the energies of the annihilating ν and $\bar{\nu}$ approximately as $\sigma \propto E_{\nu} E_{\bar{\nu}}$, which leads to

$$\dot{n}_{\nu\bar{\nu}} \propto F_{\nu} F_{\bar{\nu}}. \tag{3.18}$$

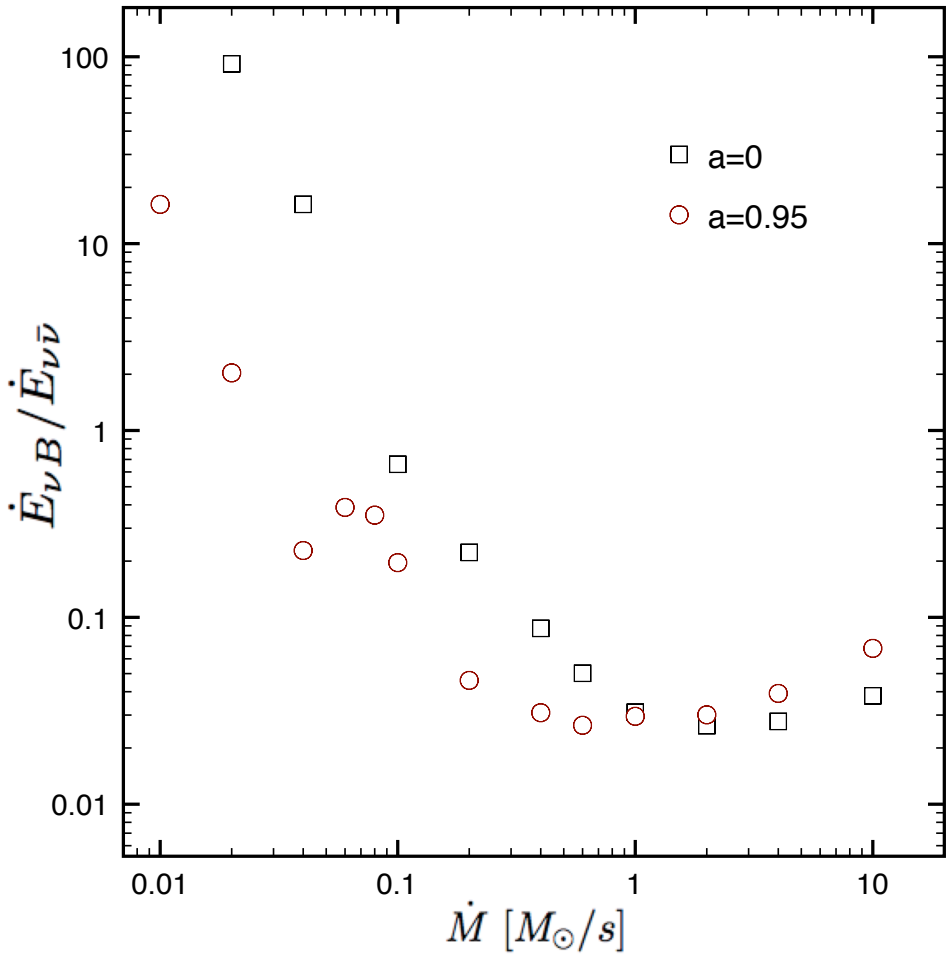

Figure 3.7: Ratio $\dot{E}_{\nu B}/\dot{E}_{\nu\bar{\nu}}$ as a function of $\dot{M}$ for $a = 0$ and $a = 0.95$. The accretion disc is assumed to have viscosity parameter $\alpha = 0.1$.

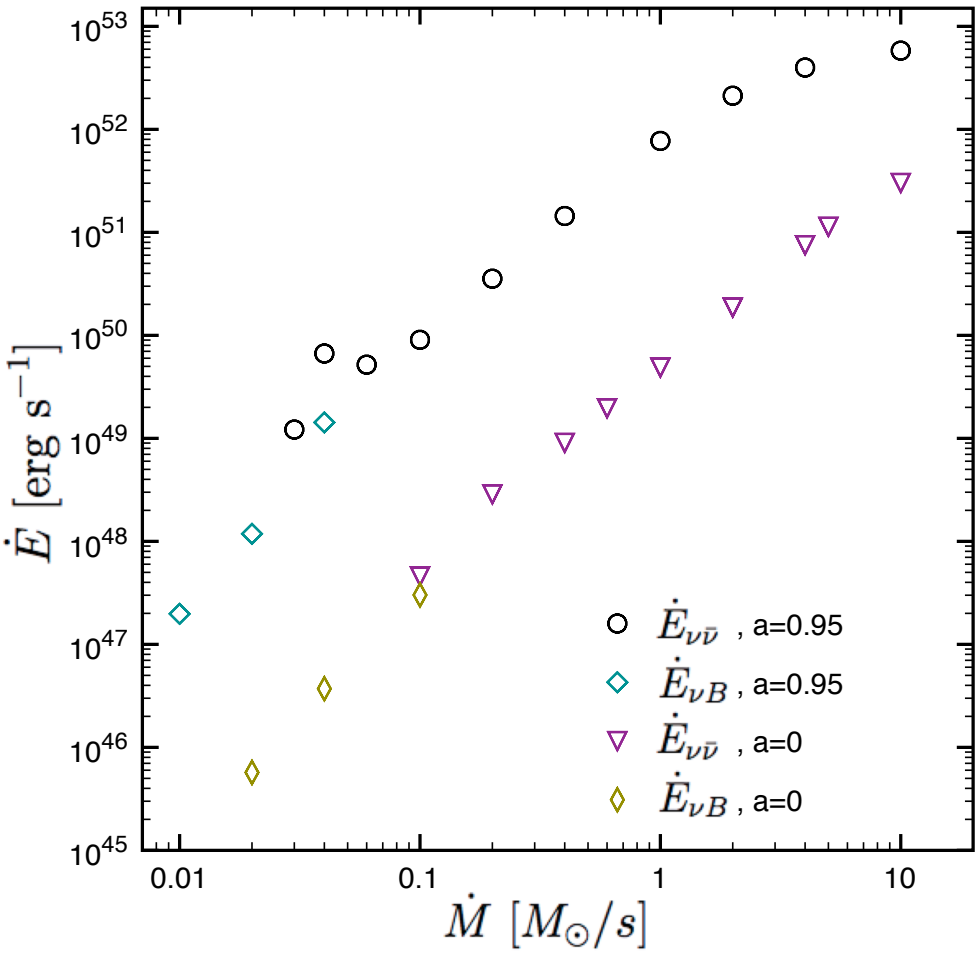

Figure 3.8: Same as Fig. 3.4 but now including the contribution of reaction $\nu \to \nu e^+ e^-$. This contribution $\dot{E}_{\nu B}$ is shown only at $\dot{M} < \dot{M}_{\rm ign}$, where it is important; $\dot{E}_{\nu B}$ is small compared with $\dot{E}_{\nu\bar{\nu}}$ at $\dot{M} > \dot{M}_{\rm ign}$ (cf. Fig. 3.7).

The energy fluxes F_ν and $F_{\bar\nu}$ from an efficiently cooled disc ($\dot M_{\rm ign} < \dot M < \dot M_{\rm trap}$) carry the released gravitational energy and do not depend on details of the disc structure. The fluxes scale with M, $\dot M$, and r as $F_\nu \sim F_{\bar\nu} \propto M\dot M/r^3$. This gives

$$\dot N_{\nu\bar\nu} \propto r^3 \dot n_{\nu\bar\nu} \propto \frac{\dot M^2}{x_{\rm ms}^3 M}. \tag{3.19}$$

Here we assumed that the size of the main annihilation region r is proportional to $r_{\rm ms} = x_{\rm ms} r_g$, where $x_{\rm ms}$ is determined by the black-hole spin parameter a (see Fig. 3.5).

The net heating rate $\dot E_{\nu\bar\nu}$ may be estimated as $\dot E_{\nu\bar\nu} \sim (E_\nu + E_{\bar\nu})\dot N_{\nu\bar\nu}$, where $E_{\bar\nu} \sim E_\nu \propto F_\nu^{1/4}$ is roughly estimated using Model C (Section 2.1). This gives

$$\dot E_{\nu\bar\nu} \propto r_{\rm ms}^3 F_\nu^{9/4} \propto x_{\rm ms}^{-15/4}\, \dot M^{9/4} M^{-3/2}. \tag{3.20}$$

Our numerical results confirm the scaling $\dot E_{\nu\bar\nu} \propto \dot M^{9/4}$ and give a somewhat steeper dependence on $x_{\rm ms}$, $\dot E_{\nu\bar\nu} \propto x_{\rm ms}^{-4.8}$ (Section 3.1). The relation $x_{\rm ms}(a)$ can be substituted here to get the dependence $\dot E_{\nu\bar\nu}(\dot M, M, a)$.

It is instructive to compare $\dot E_{\nu B}$ with $\dot E_{\nu\bar\nu}$. From equations (3.8) and (3.11) one can derive the following estimate,

$$\frac{\dot E_{\nu B}}{\dot E_{\nu\bar\nu}} \sim \frac{Q^t_{\nu B}}{Q^t_{\nu\bar\nu}} \sim 0.1\alpha_f \frac{U_B}{U_\nu} \ln\left(\frac{B}{B_Q} E\right), \tag{3.21}$$

where $\alpha_f = e^2/\hbar c = 1/137$, $B_Q = m_e^2 c^3/e\hbar \approx 4.4\times10^{13}$ G, E is the average energy of neutrinos in units of $m_e c^2$, $U_\nu \sim F_\nu/c$ is the neutrino energy density and $U_B = B^2/8\pi$. One may expect that U_B is proportional to the pressure in the disc P, which depends on viscosity parameter α. Our numerical calculations gave $\dot E_{\nu B}/\dot E_{\nu\bar\nu} \lesssim 0.1$ for discs with $\alpha = 0.1$ and $\dot M > \dot M_{\rm ign}$ (Fig. 3.7). Since $P \propto \alpha^{-1}$, models with smaller α would give a higher $\dot E_{\nu B} \propto \alpha^{-1}$. However, for discs with $\dot M > \dot M_{\rm ign}$, it will not dominate over $\dot E_{\nu\bar\nu}$ in the plausible range of $\alpha > 0.01$.

For small accretion rates $\dot M < \dot M_{\rm ign}$, F_ν is strongly suppressed and $\dot E_{\nu\bar\nu}$ is suppressed as $F_\nu^{9/4}$. Since $\dot E_{\nu B} \propto F_\nu$ its suppression is less severe. As a result $\dot E_{\nu B}$ dominates over $\dot E_{\nu\bar\nu}$ when $\dot M < \dot M_{\rm ign}$ as we found numerically in Section 3.2.

3.4 Conclusions

We have performed detailed numerical calculations of $e^{\pm}$ creation around hyper-accreting spinning black holes. We studied two reactions: $\nu\bar{\nu} \to e^+e^-$ and $\nu \to \nu e^+e^-$ (in a strong magnetic field). The reaction of $\nu\bar{\nu}$ annihilation dominates the energy deposition rate around discs with $\dot{M} > \dot{M}_{\rm ign}$, which are strong emitters of ν and $\bar{\nu}$. We found that the net energy deposition rate due to this process, $\dot{E}_{\nu\bar{\nu}}$, is well approximated by a simple formula (see Fig. 3.4),

$$\begin{aligned} \dot{E}_{\nu\bar{\nu}} &\approx 1.1\times 10^{52}\, x_{\rm ms}^{-4.8} \left(\frac{M}{3M_\odot}\right)^{-3/2} \\ &\times \left\{ \begin{array}{ll} 0 & \dot{M} < \dot{M}_{\rm ign} \\ \dot{m}^{9/4} & \dot{M}_{\rm ign} < \dot{M} < \dot{M}_{\rm trap} \\ \dot{m}_{\rm trap}^{9/4} & \dot{M} > \dot{M}_{\rm trap} \end{array} \right\} \text{erg s}^{-1}, \end{aligned} \tag{3.22}$$

where $\dot{m} = \dot{M}/M_\odot$ s^{-1}, $x_{\rm ms} = r_{\rm ms}(a)/r_g$, $r_g = 2GM/c^2$, and $\dot{M}_{\rm trap}$, $\dot{M}_{\rm ign}$ are given in equation (3.5). The dependence of $\dot{E}_{\nu\bar{\nu}}$ on the black hole spin is huge: $x_{\rm ms}^{-4.8}$ varies by a factor of 200 for $0 < a < 0.95$. Note that α (viscosity parameter of the disc) enters the result only through $\dot{M}_{\rm ign}$ and $\dot{M}_{\rm trap}$. Our numerical simulations in this paper are limited to black holes with mass $M = 3M_\odot$, and the $\dot{E}_{\nu\bar{\nu}}$ dependence on M is evaluated analytically.

The efficiency of $\nu\bar{\nu}$ annihilation can be defined as $\epsilon = \dot{E}_{\nu\bar{\nu}}/L$ where L is the total neutrino luminosity of the disc. For example, $a = 0.95$ (which corresponds to $x_{\rm ms} = 0.97$) gives $L \approx 0.15\dot{M}c^2$ (CB07) and $\epsilon \approx 0.05\dot{m}^{5/4}$ for $\dot{M}_{\rm ign} < \dot{M} < \dot{M}_{\rm trap}$. Note that $\dot{E}_{\nu\bar{\nu}}$ is defined in this paper as the total energy deposition rate outside the event horizon. A fraction of the created $e^{\pm}$ plasma falls into the black hole and does not contribute to the observed explosion (Fig. 3.2). The corresponding refinement of ϵ depends on the plasma dynamics outside the disc, which is affected by magnetic fields and hard to calculate without additional assumptions.

The obtained $\dot{E}_{\nu\bar{\nu}}$ may be comparable to GRB luminosities $L_{\rm obs}$. A plausible typical value for $L_{\rm obs}$ is $\sim 10^{51}$ erg/s (it depends on the beaming angle of the observed

explosion, which is usually hard to estimate from available data). This power is easily supplied by neutrino heating if the black hole has a large spin, e.g. $a = 0.95$, for a moderate accretion rate $\dot{M} \gtrsim 0.3 M_\odot$ s^{-1}. For a non-rotating black hole, this mechanism of GRB explosion requires ~ 10 times higher accretion rates.

Chapter 4

White dwarfs stripped by massive black holes

Ivan Zalamea, Kristen Menou, Andrei M. Beloborodov

[Published in MNRAS, 409:L25–L29, November 2010]

White dwarfs inspiraling into black holes of mass $M_{\rm BH} \gtrsim 10^5 M_\odot$ are detectable sources of gravitational waves in the LISA band. In many of these events, the white dwarf begins to lose mass during the main observational phase of the inspiral. The mass loss starts gently and can last for thousands of orbits. The white dwarf matter overflows the Roche lobe through the L_1 point at each pericenter passage and the mass loss repeats periodically. The process occurs very close to the black hole and the released gas can accrete, creating a bright source of radiation with luminosity close to the Eddington limit, $L \sim 10^{43}$ erg s^{-1}. This class of inspirals offers a promising scenario for dual detections of gravitational waves and electromagnetic radiation.

4.1 Introduction

One of the goals of the Laser Interferometer Space Antenna (LISA) mission is to detect gravitational waves from compact stellar objects spiraling into massive black

holes, a class of events called extreme-mass-ratio inspirals (EMRIs) (e.g., [Hils and Bender, 1995]; [**?**]; [Barack and Cutler, 2004]; see [Hughes, 2009] and [Sathyaprakash and Schutz, 2009] for recent reviews). Of particular interest are sources of coincident gravitational and electromagnetic radiation. Besides providing unique information on the nature of the event, such dual detections will lead to a new version of Hubble diagram that is based on the gravitational distance measurements (e.g. [Bloom *et al.*, 2009]; [Phinney, 2009]).

Inspirals into black holes of masses $M_{\rm BH} \sim (10^5 - 10^6) M_\odot$ produce gravitational waves in the frequency band where LISA is most sensitive. Normal stars are tidally disrupted well before they approach such black holes, and therefore discounted as possible LISA sources (however, see [Freitag, 2003]). Inspirals of compact objects are guaranteed sources of gravitational waves, however most of them are not promising for dual detections. In particular, stellar-mass black hole or neutron star inspirals are not expected to generate bright electromagnetic signals. Only inspiraling white dwarfs (WDs) offer a possibility for dual detection ([Menou *et al.*, 2008]; [Sesana *et al.*, 2008]). WDs can be tidally disrupted very close to the black hole and then could create a transient accretion disc with Eddington luminosity.

Estimated EMRI rates are high enough for observations with LISA (e.g. [Phinney, 2009]). The expected fraction of WD inpirals among all EMRIs depends on the degree of mass segregation in galactic nuclei, which favors stellar-mass black holes over white dwarfs in the central cluster. The abundance of white dwarfs also depends on the details of stellar evolution, which are not completely understood. A fraction of WD inpirals as large as $\sim 10\%$ has been suggested (e.g. [Hopman and Alexander, 2006b]).

The orbital parameters of WD inspirals are also uncertain. EMRIs form when a compact object is captured onto a tight orbit whose evolution is controlled by gravitational radiation rather than random interactions with other stars in the central cluster around the massive black hole. Two main channels exist for EMRI formation: capture of single stars and capture of binary systems (e.g., [Hils and Bender, 1995]

; [Sigurdsson and Rees, 1997]; [Ivanov, 2002]; [Hopman and Alexander, 2005], [Hopman and Alexander, 2006b], [Hopman and Alexander, 2006a]; [Miller *et al.*, 2005]; [Hopman, 2009]). In the single-capture scenario, the shrinking orbit can retain a significant eccentricity until the end of inspiral. In contrast, the binary-capture scenario leads to nearly circular orbits [Miller *et al.*, 2005].

In this paper, we focus on WD inspirals that are not completed because the star is tidally disrupted before its orbit becomes unstable. We argue that the WD begins to lose mass very gently and, for thousands of orbital periods, this process resembles accretion through the L_1 point in a binary system rather than a catastrophic disruption. This offers a possibility of *simultaneous* observation of the inspiral by LISA and traditional, optical and X-ray telescopes. Previous work on tidal deformation of a WD orbiting a massive black hole focused on two extreme regimes: (i) weak deformation was studied analytically using perturbation theory (e.g., [Rathore *et al.*, 2005]; [Ivanov and Papaloizou, 2007]), and (ii) strong deformation leading to immediate disruption was simulated numerically (e.g. [Kobayashi *et al.*, 2004]; [Rosswog *et al.*, 2009]). The regime considered in the present paper is different from both cases explored previously. It involves an extended phase of strong deformation with small mass loss, which we call 'tidal stripping' below. The mass of the WD remains almost unchanged during this phase and continues to emit gravitational waves. Even a small orbital eccentricity, e.g. $e = 0.01$, implies that tidal stripping occurs only near the pericenter of the orbit, during a small fraction of each orbital period. Thus, the mass loss is expected to be *periodic*, possibly leading to a periodic electromagnetic signal from the inspiral.

4.2 Tidal stripping

4.2.1 Onset of mass loss

Consider a WD orbit with semi-major axis a and eccentricity e. The orbital parameters gradually evolve as a result of gravitational radiation [Peters and Mathews, 1963]

$$\dot{a} = -\frac{64}{5}\frac{G^3 M M_{\rm BH}^2}{c^5 a^3 (1-e^2)^{7/2}}\left(1+\frac{73}{24}e^2+\frac{37}{96}e^4\right), \quad (4.1)$$

$$\dot{e} = -\frac{304}{15}\frac{G^3 M M_{\rm BH}^2}{c^5 a^4 (1-e^2)^{5/2}}\left(1+\frac{121}{304}e^2\right)e, \quad (4.2)$$

where dot denotes the time derivative of the secular evolution (averaged over the orbit). Both a and e slowly decrease with time. The fractional change of the pericenter radius $r_p = a(1-e)$ in one orbital period $P = 2\pi(a^3/GM_{\rm BH})^{1/2}$ is

$$\alpha \equiv \frac{-\dot{r}_p P}{r_p} = \frac{128\pi G^{5/2} M_{\rm BH}^{3/2} M}{5c^2\, r_p^{5/2}}\frac{\left(1-\frac{7}{12}e+\frac{7}{8}e^2+\frac{47}{192}e^3\right)}{(1+e)^{7/2}}. \quad (4.3)$$

For the typical parameters of the problem considered in this paper, $\alpha \sim 10^{-5}$. Two inaccuracies in the above formulas should be noted: (i) Equations (4.1)-(4.3) are valid only if $r_p \gg GM_{\rm BH}/c^2$. They become approximate during the most interesting phase of the inspiral when r_p is only a few $r_g = 2GM_{\rm BH}/c^2$. (ii) The equations neglect the effects of mass loss on the evolution of the orbit.[1]

The mass loss begins when the tidal acceleration created by the black hole at the WD surface, $(GM_{\rm BH}/r_p^3)R$, becomes comparable to GM/R^2, where R is the radius of the WD. A similar condition for the onset of mass transfer in synchronous binary systems is that the donor star fills its Roche lobe. In the more complicated case of eccentric non-synchronous binary systems, mass transfer may be approximately described using an instantaneous effective Roche lobe [Sepinsky *et al.*, 2007], neglecting

[1] Let δM be the mass lost in one orbit. The maximum correction to α is $\sim \delta M/M$, and it is significant only when δM exceeds αM. Section 2.3 suggests that the value of α is unimportant at this stage, as the evolution becomes controlled by the mass loss itself, not the drift of the pericenter.

all the effects beyond the quasi-static limit (e.g. [Ritter, 1988]). We will use the following approximate condition for the mass-loss onset,

$$R > R_t \equiv \gamma\, r_p \left(\frac{M}{M_{\rm BH}}\right)^{1/3}, \tag{4.4}$$

where R is the radius of the *unperturbed* star, before it experiences any tidal deformation, and γ is a numerical constant. The exact value of γ depends on the mass ratio $M/M_{\rm BH}$ and the orbital parameters a and e. Even more importantly, it also depends on the rotation of the WD and the history of its tidal heating, none of which is known. If R_t is interpreted as the effective Roche-lobe studied by [Sepinsky *et al.*, 2007], their results give $0.39 \leqslant \gamma \leqslant 0.59$, with $\gamma = 0.49$ for synchronous binary systems. Our conclusions are independent of the exact value for γ. In numerical examples where it needs to be specified, we assume $\gamma \approx 0.5$.

The orbit slowly shrinks due to gravitational radiation and condition (4.4) will be first met when the pericenter radius r_p reaches the value r_0 estimated below. We adopt a simple model for the unperturbed WD star: a non-rotating cold sphere of uniform chemical composition, supported by the pressure of degenerate electrons. It is straightforward to obtain numerically the mass-radius relation for such a star. We find that it is well approximated by the following formula (with less than 2 per cent error for $0.2M_\odot < M < 1.4M_\odot$. See appendix C.),

$$R = R_\star \left(\frac{M_{\rm Ch}}{M}\right)^{1/3} \left(1 - \frac{M}{M_{\rm Ch}}\right)^{\beta}, \tag{4.5}$$

where $M_{\rm Ch} = 1.43M_\odot$ is the Chandrasekhar mass, $\beta = 0.447$ and $R_\star = 0.013R_\odot$. Substituting $R(M)$ in equation (4.4), one obtains the pericenter radius at which mass loss begins

$$r_0 = \frac{R_\star}{\gamma} \left(\frac{M_{\rm Ch} M_{\rm BH}}{M^2}\right)^{1/3} \left(1 - \frac{M}{M_{\rm Ch}}\right)^{\beta}. \tag{4.6}$$

Figure 4.1 shows r_0/r_g as a function of WD mass for different $M_{\rm BH}$.

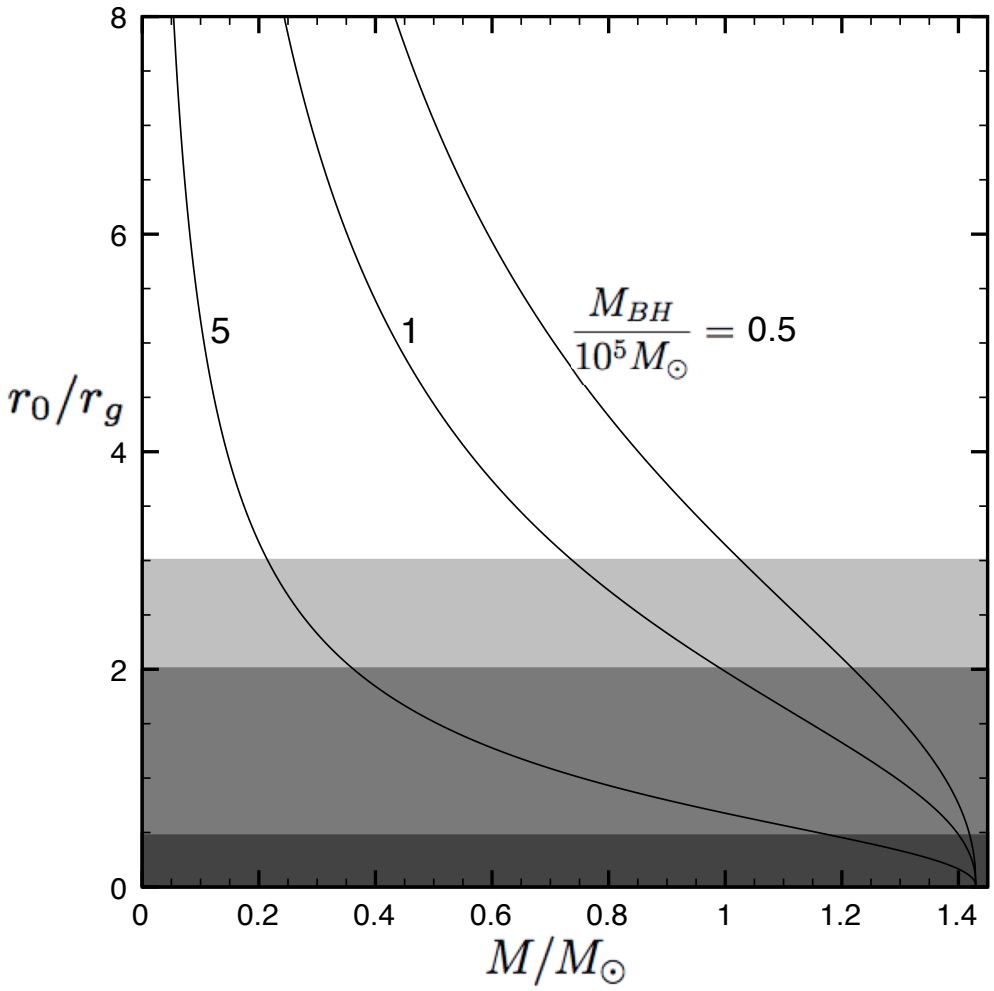

Figure 4.1: Radius r_0 where tidal stripping begins, in units of the Schwarzschild radius $r_g \equiv 2GM_{\rm BH}/c^2 \approx 3 \times 10^{10}(M_{\rm BH}/10^5 M_\odot)$ cm, is shown as a function of the WD mass. The three curves correspond to $M_{\rm BH}/10^5 M_\odot = 0.5$, 1 and 5. The value of r_0 was estimated using the simplified equation (4.6), which is non-relativistic and neglects the effect of the black-hole spin a_s on the tidal force. The shaded region shows radii $r < r_{\rm min}$ where no stable bound orbits exist. $r_{\rm min}$ depends on a_s and orbital eccentricity e, in particular $r_{\rm min} = 3r_g$ for $\{a_s = 0, e = 0\}$, $r_{\rm min} = 2r_g$ for $\{a_s = 0, e = 1\}$ and $r_{\rm min} = r_g/2$ for $\{a_s = 1, e = 1\}$.

4.2.2 Estimate for mass loss in one orbital period

As the star begins to lose mass, it continues to do so repeatedly: at each pericenter passage the star overflows the Roche lobe for a short time. The hydrodynamics of the surface layers of the tidally stripped star is complicated. It is clear however that the mass lost in one pericenter passage, δM, will be tiny for the initial mass loss episodes when the star surface barely touches the Roche lobe. The natural small parameter in the problem is $\Delta/R = (R - R_t)/R$. The onset of mass loss is defined by $\Delta = 0$ and we assume that the dependence of δM on $\Delta/R \ll 1$ can be expanded in series whose leading term has the form,

$$\frac{\delta M}{M} = A \left(\frac{\Delta}{R}\right)^{\psi}, \qquad \Delta \equiv R - R_t \ll R, \tag{4.7}$$

where A is a numerical factor.

For illustration, consider a toy model. Suppose that after the pericenter passage the star loses the surface shell $\Delta \ll R$ whose mass is estimated using the structure of the unperturbed star,

$$\delta M = 4\pi R^2 \int_0^{\Delta} \rho(z)\, dz. \tag{4.8}$$

Here z is the depth measured inward from the surface, and $\rho(z)$ is the mass density of the unperturbed star at depth z. For simplicity, let us assume the polytropic equation of state in the surface layer $P = K\rho^{\gamma}$ with $\gamma = 5/3$, the same as in the deeper region where electrons become degenerate. P and ρ change continuously between the degenerate and non-degenerate regions, and therefore K in the surface layers must be the same as for non-relativistic degenerate electron gas,

$$K \equiv \frac{1}{20}\left(\frac{3}{\pi}\right)^{2/3} \frac{h^2}{m_e(\mu_e m_p)^{5/3}}, \tag{4.9}$$

where $\mu_e \approx 2$ is the mean molecular weight per electron. The hydrostatic balance $dP/dz = \rho GM/R^2$ gives

$$\rho(z) = \left(\frac{2GM}{5KR}\right)^{3/2} \left(\frac{z}{R}\right)^{3/2}, \tag{4.10}$$

and evaluating the integral in equation (4.8) one finds $\delta M/M = A(\Delta/R)^{\psi}$ with

$$\psi = \frac{5}{2}, \qquad A \approx 6.1 \left(1 - \frac{M}{M_{\rm Ch}}\right)^{3\beta/2}. \tag{4.11}$$

In this toy model, $\delta M = (6/5)[\rho(\Delta)/\bar{\rho}](\Delta/R)$ where $\bar{\rho} = 3M/4\pi R^3$. The small factor $(\Delta/R)^{\psi} \ll 1$ in δM results from the small thickness of the surface layer Δ and the small density of this layer, $\rho(\Delta)/\bar{\rho} \sim (\Delta/R)^{3/2}$.

Additional factors may enter a more realistic model. The duration of the mass-loss episode δt may be so short that only a fraction of the Δ-layer is lost. δt likely scales with some power of Δ/R. One could formulate a time-dependent model for the mass-loss episode by evaluating R_t along the orbit around the pericenter (instead of just one point r_p). If one assumes that the mass-loss episode occurs where $R_t < R$, then $\delta t \sim (\Delta/R)^{1/2}\tau$ where τ is the sound-crossing time of the star. A complete hydrodynamical model is three-dimensional as the mass loss is asymmetric: gas will flow through the L_1 point, as happens in close binary systems. The flow velocity may be comparable to the sound speed in the outer layers of the star (which is smaller than the sound speed in its interior). Perhaps future hydrodynamical calculations will give the duration of the mass loss episode and the resulting ψ, A and δM. We do not know the exact values of ψ and A and keep them as parameters. The illustrative numerical example shown below assumes ψ and A given in equation (4.11).

From equations (4.4) and (4.6) one finds

$$\frac{\Delta}{R} = 1 - \frac{R_t}{R} = 1 - \frac{r_p}{r_0}\left(\frac{M}{M_0}\right)^{2/3}\left(\frac{M_{\rm Ch} - M_0}{M_{\rm Ch} - M}\right)^{\beta}. \tag{4.12}$$

For the first mass loss episode, $M = M_0$ and $r_p/r_0 \sim 1 - \alpha$, which implies $\Delta/R \sim \alpha \sim 10^{-5}$. Equation (4.12) shows that Δ grows with each passage of the pericenter as r_p decreases (due to gravitational radiation) and M decreases (due to mass loss).

4.2.3 Evolution of mass loss over many orbits

N orbits after the star reached r_0, the pericenter radius is given by

$$\frac{r_p}{r_0} \approx 1 - \alpha N, \qquad \alpha N \ll 1, \tag{4.13}$$

where α is given by equation (4.3). Here we assumed that r_p decreases by αr_p in each orbit, neglecting the effect of mass loss on the orbit (which is likely to be a poor approximation at late stages of mass loss, e.g. Bildsten & Cutler 1992).

Let x be the mass fraction of the star that has been lost over N orbits,

$$x = \frac{M_0 - M}{M_0}. \tag{4.14}$$

As long as $x \ll 1$, one can expand Δ in x and αN and keep only the leading linear terms,

$$\frac{\Delta}{R} \approx \frac{\Delta}{R_0} \approx \alpha\, N + B\, x, \qquad B = \frac{2}{3} + \frac{\beta M_0}{M_{\rm Ch} - M_0}. \tag{4.15}$$

The term αN describes the change in R_t/R_0 due to the decreasing r_p while the small changes in M and R are neglected. The term Bx describes the effect of decreasing M on R_t and R while the small drift of the pericenter is neglected.

It is convenient to treat $N \gg 1$ as a continuous variable and describe the mass loss by the differential equation $dM/dN = -\delta M$. Then substitution of equation (4.15) to equation (4.7) gives the differential equation for $x(N)$,

$$\frac{dx}{dN} = A\,(\alpha N + Bx)^{\psi}\,. \tag{4.16}$$

One can see from this equation that there are two stages of mass loss: (a) $Bx \ll \alpha N$ and (b) $Bx \gg \alpha N$. Assuming $\psi > 1$, we find the solutions for the two regimes,

$$x \approx \frac{A}{\psi + 1}\,\alpha^{\psi} N^{\psi+1}, \qquad N < N_1, \tag{4.17}$$

$$x \approx \left[(\psi - 1) A B^{\psi} (N_\star - N)\right]^{1/(1-\psi)}, \qquad N > N_1. \tag{4.18}$$

Equation (4.18) applies only as long as $x \ll 1$, however it gives an estimate for the number of orbits to complete disruption $N_\star$. The values of N_1 and $N_\star$ can be

evaluated by matching x and dx/dN for the two solutions at $N = N_1$,

$$N_1 = \left(\frac{\psi+1}{AB}\right)^{1/\psi} \alpha^{(1-\psi)/\psi}, \tag{4.19}$$

$$\frac{N_\star - N_1}{N_1} = \frac{1}{\psi^2 - 1}. \tag{4.20}$$

At $N < N_1$ the growth of x is caused by the decrease in r_p at practically unchanged mass and radius of the star. After N_1 orbits, the growth of x accelerates as it is now controlled by the decreasing M (and increasing R) while the change in r_p has a negligible effect. Equations (4.17) and (4.18) imply that $\delta M \propto N^\psi$ for $N < N_1$ and $\delta M \propto (N_\star - N)^{\psi/(1-\psi)}$ for $N > N_1$.

For example, consider the toy model described by equation (4.11). In this case, $N_1 \sim \alpha^{-3/5} \sim 10^3$ and $N_\star - N_1 = (4/21)N_1$. The mass fraction lost after N_1 orbits is $x(N_1) \sim \alpha N_1/B \sim \alpha^{2/5} \sim 10^{-2}$. The detailed behavior of $x(N)$ in the toy model is shown in Figure 2 for a WD with initial mass $M_0 = 0.6M_\odot$. The figure shows the solution of equation $dx/dN = A(\Delta/R)^\psi$ with Δ given by equation (4.12).

4.2.4 Periodic mass-loss rate

The mass-loss rate dM/dt is nearly periodic with the orbital period P. It is zero throughout most of the orbit and has a strong peak near the pericenter. To illustrate this behavior, we calculated the following, greatly simplified model,

$$\frac{dM}{dt} = \begin{cases} -\delta M/\tau(M) & R_t < R \\ 0 & R_t > R \end{cases} \tag{4.21}$$

where $R(M)$ is the radius of the unperturbed star of mass M, R_t is calculated everywhere along the orbit according to equation (4.4). $\delta M(t)$ is given by equation (4.7) (it is evaluated using the local value of R_t); $\tau = (G\bar{\rho})^{-1/2}$ is the sound-crossing time-scale of the star.

Figure 4.3 shows the numerical solution of equation (4.21) for the last 35 orbits before disruption. The WD is assumed to have an initial mass $M_0 = 0.6M_\odot$ and

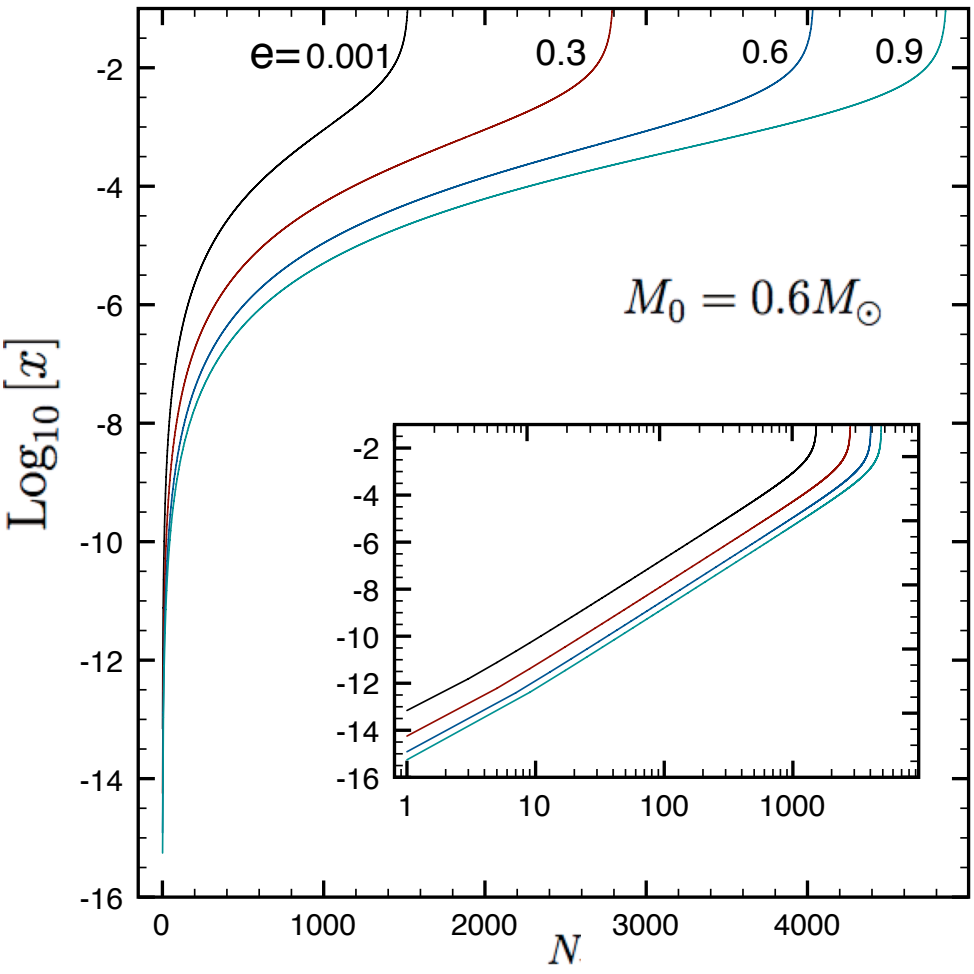

Figure 4.2: Lost mass fraction $x = (M_0 - M)/M_0$ after N orbits since the onset of tidal stripping. The WD has initial mass $M_0 = 0.6M_\odot$. Different curves correspond to different eccentricities of the orbit; $M_{\rm BH} = 10^5 M_\odot$ is assumed for all cases. The insert shows $\log x$ plotted against $\log N$.

orbital eccentricity $e = 0.9$; the orbital period is $P \approx 2 \times 10^3$ s. We plot the instantaneous mass-loss rate $|dM/dt|$ versus time $t_{\rm loss}$ shown by a clock that ticks only when $dM/dt \neq 0$. The periodic peaks in $|dM/dt|$ coincide with the pericenter passages.

4.3 Discussion: electromagnetic counterpart

The standard picture of EMRI envisions an orbit that gradually shrinks due to gravitational radiation until its pericenter r_p reaches $r_{\rm min}$ where the orbit becomes unstable and plunges into the black hole. The main observational phase of the inspiral is when r_p decreases from $\sim 2r_{\rm min}$ to $r_{\rm min}$. For WDs with mass $M \sim M_\odot$ inspiraling into a black hole with $M_{\rm BH} \sim 10^5 M_\odot$ the main observational phase lasts $\sim 10^5$ orbital periods, which may be comparable to one year, depending on the orbital eccentricity. We argued in Section 2 that the inspiraling WDs can experience an extended period of slow mass loss during observations by LISA.

To summarize, the tidal stripping begins very gently because the pericenter of the orbit drifts inward slowly, by a tiny fraction $\alpha \sim 10^{-5}$ in one orbital period. This leads to many repeated episodes of small mass loss. The process occurs at radius r_0 (eq. 4.6), comparable to $r_{\rm min}$. The star is strongly deformed by the tidal forces near r_0 but it barely touches its Roche lobe for a small fraction of the orbital period. As a result, the star loses a small amount of mass through the L_1 point at each pericenter passage. To our knowledge, this regime of tidal stripping was not explored by direct hydrodynamical simulations. Our crude estimates suggest two phases of stripping: the first phase lasts $N_1 \sim 10^3$ orbits until the star loses ~ 1 per cent of its mass. Then the mass loss accelerates: the decrease in M (and the corresponding increase in the WD radius) implies that the star overfills the Roche lobe more and more with every pericenter passage. As a result, the star loses the remaining 99 per cent of its mass in a few hundreds of additional orbits. The mass lost in each individual episode during these last hundreds of orbits behaves as $\delta M \propto (N_\star - N)^{-\xi}$ where $N_\star - N \ll N_\star$ is

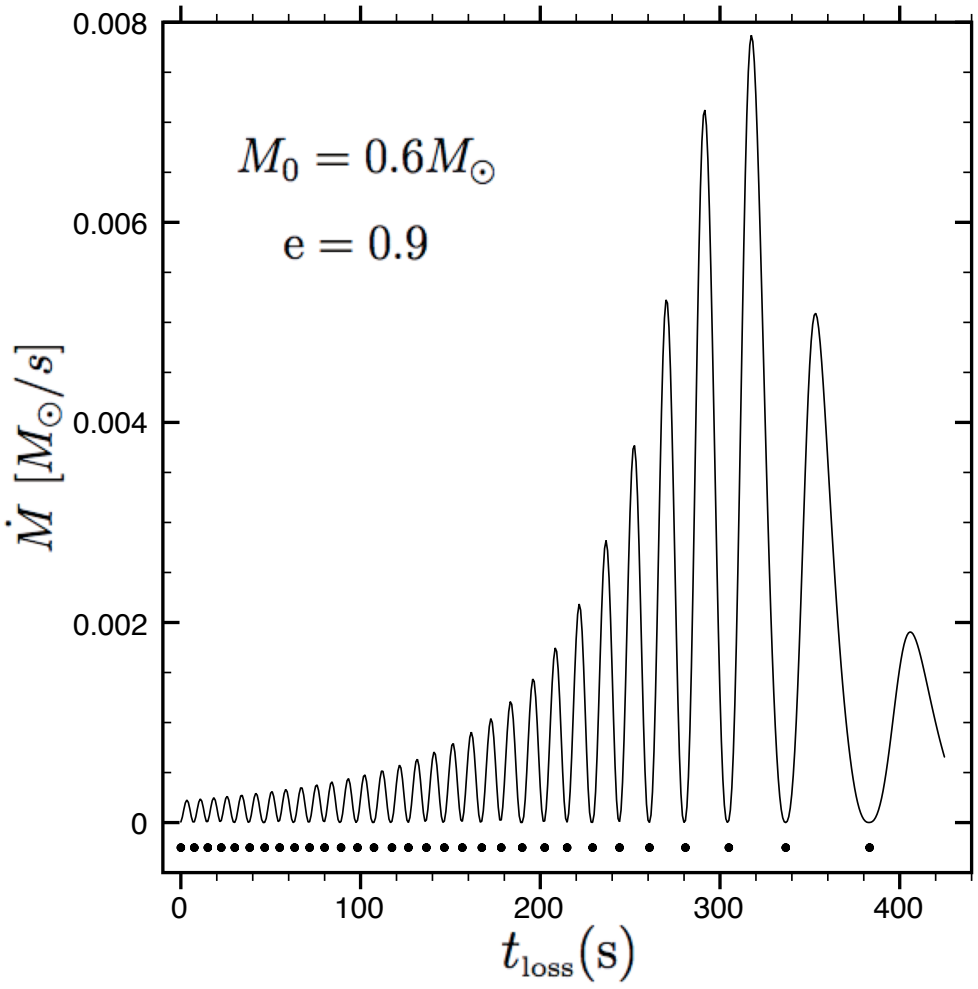

Figure 4.3: Instantaneous mass-loss rate $\dot{M} = |dM/dt|$ during the last 35 orbits before disruption. The WD with initial mass $M_0 = 0.6M_\odot$ is orbiting a black hole with $M_{\rm BH} = 10^5 M_\odot$; the orbit has eccentricity $e = 0.9$. The horizontal axis shows 'time during mass transfer', which increases only when $\dot{M} \neq 0$. The area under each peak is the mass lost per pericenter passage; it follows a power law with the number of orbits left to complete disruption, $\delta M \propto (N_\star - N)^{-1.8}$, close to the results of Section 2.3.

the number of orbits remaining to complete disruption and $\xi \sim \psi/(\psi - 1)$.

According to our estimates, tidal stripping operates for days or weeks, creating a relatively long-lived source of gas. The gas can accrete onto the black hole and produce significant electromagnetic radiation together with the gravitational waves observed by LISA. The radiation source may become bright before the mass loss spoils the standard EMRI template for the gravitational-wave signal.

The gas produced by tidal stripping moves on nearly Keplerian orbits that are initially close to the WD orbit. The gas probably leaves the star with relative velocity $\sim v_{\rm esc} = (2GM/R)^{1/2}$ and its orbital energy differs from that of the star by a small fraction $\sim v_{\rm esc}/v \sim (Mr_0/M_{\rm BH}R)^{1/2} \sim \gamma^{-1/2}(M/M_{\rm BH})^{1/3} \sim 1/30$. After ~ 30 orbital periods, the differential rotation of the gas has stretched it into a ring around the black hole. A non-zero eccentricity of the donor orbit will create an eccentric ring. It should viscously spread and accrete onto the black hole. A small mass-loss fraction x can be a huge source of gas for accretion. If most of the stripped matter is accreted by the black hole, the accretion rate is $\dot{M} \sim \delta M/P$. It exceeds the Eddington value $\dot{M}_{\rm Edd} \sim 10^{23}(M_{\rm BH}/10^5 M_\odot)$ g s^{-1} after $N \sim 10$ orbits since the beginning of tidal stripping, well before the final disruption of the WD. The accretion timescale in the viscous ring can be estimated as $t_{\rm acc} \sim \alpha_v^{-1}(H/r)^{-2}P$ where P is the WD orbital period, $\alpha_v = 0.01 - 0.1$ is the viscosity parameter and H is the thickness of the ring (e.g. [Shakura and Sunyaev, 1973]). $H/r \sim 1$ is expected for super-Eddington accretion, which leads to $t_{\rm acc} \sim (10 - 100)P$.

This suggests that a bright source with Eddington luminosity $L_{\rm Edd} \sim 10^{43}$ erg s^{-1} is created quickly, in less than 1 day after the beginning of tidal stripping. For a typical distance to such LISA sources, $d \sim 100$ Mpc, the accretion ring should be detectable with optical and X-ray telescopes provided its approximate location on the sky is known. LISA is expected to localize EMRIs within ~ 10 deg^2 [Barack and Cutler, 2004]. For massive black-hole mergers, the localization information will be available weeks to months prior to the final coalescence ([Kocsis *et al.*, 2007], [Kocsis *et al.*,

2008]; [Lang and Hughes, 2008]), and the localization expectations for WD EMRIs are similar (S. Drasco, J. Gair, I. Mandel, E. Porter, private communications), giving sufficient time for simultaneous optical and X-ray observations during inspiral.

Mass transfer in WD inspirals is special as it creates a long-lived source of gas very close to the black hole horizon, $r_0 - r_g \sim r_g$. As a result, the donor orbit is generally not confined to a plane, if the black hole rotation is significant. Besides, the orbit will experience fast precession. Therefore, the freshly stripped gas may collide with the previously released gas and generate shocks (e.g. [Evans and Kochanek, 1989]). The resulting pattern of accretion may be complicated and needs careful study.

An intriguing feature of tidal stripping is the periodic supply of gas. It may leave a fingerprint on the observed luminosity, modulating it with the WD orbital period P. The modulation of $\dot{M}$ may create a detectable oscillation in the luminosity from the accreting ring, even though the accretion timescale $t_{\rm acc} \sim (10-100)P \gg P$, tends to reduce the amplitude of modulation. The shock emission from collisions between the periodic flow from the L_1 point and the gas accumulated around the black hole may be strongly modulated.

The description of mass transfer in this paper is greatly simplified. The possibility of many repeated mass-transfer episodes is robust, but the exact rate of tidal stripping and the dynamics of accretion need to be explored with dedicated numerical simulations. The great potential that such events hold for joint detections of gravitational and electromagnetic radiation provides motivation for the effort. The joint detection would let us witness, in real-time and unprecedented detail, the slow tidal stripping of a WD followed by its complete disruption. Note that LISA observations are expected to provide the mass and spin of the black hole, as well as the details of the inspiral orbit. This can be used to model in detail the hydrodynamics of accretion.

The scenario discussed in this paper assumes $r_0 > r_{\rm min}$ and uses a semi-Newtonian description for the WD orbit. A fully relativistic model will be needed to accurately evaluate the parameter space for such events. The relativistic effects are especially

important if the black hole is rapidly rotating – then r_0 and $r_{\rm min}$ will depend on the black hole mass $M_{\rm BH}$, its spin parameter a_s, the eccentricity of the orbit, and the angle between the orbital angular momentum and the angular momentum of the black hole. The competition between tidal disruption and gravitational capture by rotating black holes was investigated for parabolic orbits in [Beloborodov *et al.*, 1992]. In a broad range of $M_{\rm BH}$, the fate of a star approaching the black hole depends on the orbit orientation and can be either disruption or capture. For inspirals with $r_g < r_0 < r_{\rm min}$, tidal stripping does not occur. Instead, r_p reaches $r_{\rm min}$ and the orbit loses stability before any mass is lost by the WD. Then the star is crushed by tidal forces as it falls into the black hole. This strong and immediate disruption is different from the gentle stripping considered here, suggesting rich phenomenology of WD inspirals.

Acknowledgements

This work was supported in part by NASA ATFP grant NNXO8AH35G and by the National Science Foundation under Grant No. PHY05-51164.

Bibliography

[Abramowicz and Zurek, 1981] M. A. Abramowicz and W. H. Zurek. Rotation-induced bistability of transonic accretion onto a black hole. ApJ, 246:314–320, May 1981.

[Abramowicz *et al.*, 1988] M. A. Abramowicz, B. Czerny, J. P. Lasota, and E. Szuszkiewicz. Slim accretion disks. ApJ, 332:646–658, September 1988.

[Abramowicz, 2005] M. A. Abramowicz. QPO as the Rosetta Stone for understanding black hole accretion. *Astronomische Nachrichten*, 326:782–786, November 2005.

[Afshordi and Paczyński, 2003] N. Afshordi and B. Paczyński. Geometrically Thin Disk Accreting into a Black Hole. ApJ, 592:354–367, July 2003.

[Agol and Krolik, 2000] E. Agol and J. H. Krolik. Magnetic Stress at the Marginally Stable Orbit: Altered Disk Structure, Radiation, and Black Hole Spin Evolution. ApJ, 528:161–170, January 2000.

[Armitage, 2010] P. J. Armitage. *Astrophysics of Planet Formation*. 2010.

[Asano and Fukuyama, 2001] K. Asano and T. Fukuyama. Relativistic Effects on Neutrino Pair Annihilation above a Kerr Black Hole with the Accretion Disk. ApJ, 546:1019–1026, January 2001.

[Bachetti *et al.*, 2010] M. Bachetti, M. M. Romanova, A. Kulkarni, L. Burderi, and T. di Salvo. QPO emission from moving hot spots on the surface of neutron stars: a model. MNRAS, 403:1193–1205, April 2010.

[Balbus and Hawley, 1991] S. A. Balbus and J. F. Hawley. A powerful local shear instability in weakly magnetized disks. I - Linear analysis. II - Nonlinear evolution. ApJ, 376:214–233, July 1991.

[Balbus and Hawley, 1998] S. A. Balbus and J. F. Hawley. Instability, turbulence, and enhanced transport in accretion disks. *Reviews of Modern Physics*, 70:1–53, January 1998.

[Band *et al.*, 1993] D. Band, J. Matteson, L. Ford, B. Schaefer, D. Palmer, B. Teegarden, T. Cline, M. Briggs, W. Paciesas, G. Pendleton, G. Fishman, C. Kouveliotou, C. Meegan, R. Wilson, and P. Lestrade. BATSE observations of gamma-ray burst spectra. I - Spectral diversity. ApJ, 413:281–292, August 1993.

[Barack and Cutler, 2004] L. Barack and C. Cutler. LISA capture sources: Approximate waveforms, signal-to-noise ratios, and parameter estimation accuracy. Phys. Rev. D, 69(8):082005–+, April 2004.

[Begelman *et al.*, 1984] M. C. Begelman, R. D. Blandford, and M. J. Rees. Theory of extragalactic radio sources. *Reviews of Modern Physics*, 56:255–351, April 1984.

[Belloni, 2010] T. Belloni, editor. *The Jet Paradigm*, volume 794 of *Lecture Notes in Physics, Berlin Springer Verlag*, March 2010.

[Beloborodov and Illarionov, 2001] A. M. Beloborodov and A. F. Illarionov. Small-scale inviscid accretion discs around black holes. MNRAS, 323:167–176, May 2001.

[Beloborodov *et al.*, 1992] A. M. Beloborodov, A. F. Illarionov, P. B. Ivanov, and A. G. Polnarev. Angular momentum of a supermassive black hole in a dense star cluster. MNRAS, 259:209–217, November 1992.

[Beloborodov, 1999] A. M. Beloborodov. Accretion Disk Models. In J. Poutanen & R. Svensson, editor, *High Energy Processes in Accreting Black Holes*, volume 161 of *Astronomical Society of the Pacific Conference Series*, pages 295–+, 1999.

[Beloborodov, 2003] A. M. Beloborodov. Nuclear Composition of Gamma-Ray Burst Fireballs. ApJ, 588:931–944, May 2003.

[Beloborodov, 2008] A. M. Beloborodov. Hyper-accreting black holes. In M. Axelsson, editor, *American Institute of Physics Conference Series*, volume 1054 of *American Institute of Physics Conference Series*, pages 51–70, September 2008.

[Beloborodov, 2010] A. M. Beloborodov. Collisional mechanism for gamma-ray burst emission. MNRAS, 407:1033–1047, September 2010.

[Birkl *et al.*, 2007] R. Birkl, M. A. Aloy, H.-T. Janka, and E. Müller. Neutrino pair annihilation near accreting, stellar-mass black holes. A&A, 463:51–67, February 2007.

[Blandford and Payne, 1982] R. D. Blandford and D. G. Payne. Hydromagnetic flows from accretion discs and the production of radio jets. MNRAS, 199:883–903, June 1982.

[Blandford and Znajek, 1977] R. D. Blandford and R. L. Znajek. Electromagnetic extraction of energy from Kerr black holes. MNRAS, 179:433–456, May 1977.

[Blondin and Pope, 2009] J. M. Blondin and T. C. Pope. Revisiting the "Flip-Flop" Instability of Hoyle-Lyttleton Accretion. ApJ, 700:95–102, July 2009.

[Bloom *et al.*, 2009] J. S. Bloom, D. E. Holz, S. A. Hughes, K. Menou, A. Adams, S. F. Anderson, A. Becker, G. C. Bower, N. Brandt, B. Cobb, K. Cook, A. Corsi, S. Covino, D. Fox, A. Fruchter, C. Fryer, J. Grindlay, D. Hartmann, Z. Haiman, B. Kocsis, L. Jones, A. Loeb, S. Marka, B. Metzger, E. Nakar, S. Nissanke, D. A. Perley, T. Piran, D. Poznanski, T. Prince, J. Schnittman, A. Soderberg, M. Strauss,

P. S. Shawhan, D. H. Shoemaker, J. Sievers, C. Stubbs, G. Tagliaferri, P. Ubertini, and P. Wozniak. Astro2010 Decadal Survey Whitepaper: Coordinated Science in the Gravitational and Electromagnetic Skies. *ArXiv e-prints*, February 2009.

[Bondi, 1952] H. Bondi. On spherically symmetrical accretion. MNRAS, 112:195–+, 1952.

[Bridle and Perley, 1984] A. H. Bridle and R. A. Perley. Extragalactic Radio Jets. ARA&A, 22:319–358, 1984.

[Briggs *et al.*, 1999] M. S. Briggs, D. L. Band, R. M. Kippen, R. D. Preece, C. Kouveliotou, J. van Paradijs, G. H. Share, R. J. Murphy, S. M. Matz, A. Connors, C. Winkler, M. L. McConnell, J. M. Ryan, O. R. Williams, C. A. Young, B. Dingus, J. R. Catelli, and R. A. M. J. Wijers. Observations of GRB 990123 by the Compton Gamma Ray Observatory. ApJ, 524:82–91, October 1999.

[Burrows and Thompson, 2002] A. Burrows and T. A. Thompson. Neutrino-Matter Interaction Rates in Supernovae: The Essential Microphysics of Core Collapse. *ArXiv Astrophysics e-prints*, November 2002.

[Cenko *et al.*, 2010] S. B. Cenko, D. A. Frail, F. A. Harrison, S. R. Kulkarni, E. Nakar, P. C. Chandra, N. R. Butler, D. B. Fox, A. Gal-Yam, M. M. Kasliwal, J. Kelemen, D.-S. Moon, E. O. Ofek, P. A. Price, A. Rau, A. M. Soderberg, H. I. Teplitz, M. W. Werner, D. C.-J. Bock, J. S. Bloom, D. A. Starr, A. V. Filippenko, R. A. Chevalier, N. Gehrels, J. N. Nousek, and T. Piran. The Collimation and Energetics of the Brightest Swift Gamma-ray Bursts. ApJ, 711:641–654, March 2010.

[Chandrasekhar, 1992] S. Chandrasekhar. *The mathematical theory of black holes*. 1992.

[Chen and Beloborodov, 2007] W.-X. Chen and A. M. Beloborodov. Neutrino-cooled Accretion Disks around Spinning Black Holes. ApJ, 657:383–399, March 2007.

[Davis and Hubeny, 2006] S. W. Davis and I. Hubeny. A Grid of Relativistic, Non-LTE Accretion Disk Models for Spectral Fitting of Black Hole Binaries. ApJS, 164:530–535, June 2006.

[Done *et al.*, 2007] C. Done, M. Gierliński, and A. Kubota. Modelling the behaviour of accretion flows in X-ray binaries. Everything you always wanted to know about accretion but were afraid to ask. A&A Rev., 15:1–66, December 2007.

[Eichler *et al.*, 1989] D. Eichler, M. Livio, T. Piran, and D. N. Schramm. Nucleosynthesis, neutrino bursts and gamma-rays from coalescing neutron stars. Nature, 340:126–128, July 1989.

[Esin *et al.*, 1998] A. A. Esin, R. Narayan, W. Cui, J. E. Grove, and S.-N. Zhang. Spectral Transitions in Cygnus X-1 and Other Black Hole X-Ray Binaries. ApJ, 505:854–868, October 1998.

[Evans and Kochanek, 1989] C. R. Evans and C. S. Kochanek. The tidal disruption of a star by a massive black hole. ApJ, 346:L13–L16, November 1989.

[Fender *et al.*, 2004] R. P. Fender, T. M. Belloni, and E. Gallo. Towards a unified model for black hole X-ray binary jets. MNRAS, 355:1105–1118, December 2004.

[Fleming *et al.*, 2000] T. P. Fleming, J. M. Stone, and J. F. Hawley. The Effect of Resistivity on the Nonlinear Stage of the Magnetorotational Instability in Accretion Disks. ApJ, 530:464–477, February 2000.

[Frank *et al.*, 1992] J. Frank, A. King, and D. Raine. *Accretion power in astrophysics.* 1992.

[Freitag, 2003] M. Freitag. Gravitational Waves from Stars Orbiting the Sagittarius A* Black Hole. ApJ, 583:L21–L24, January 2003.

[Giannios, 2008] D. Giannios. Prompt GRB emission from gradual energy dissipation. A&A, 480:305–312, March 2008.

[Gvozdev and Ognev, 2001] A. A. Gvozdev and I. S. Ognev. Efficiency of Electron-Positron Pair Production by Neutrino Flux from Accretion Disk of a Kerr Black Hole. *Soviet Journal of Experimental and Theoretical Physics Letters*, 74:298–301, September 2001.

[Hils and Bender, 1995] D. Hils and P. L. Bender. Gradual approach to coalescence for compact stars orbiting massive black holes. ApJ, 445:L7–L10, May 1995.

[Hopman and Alexander, 2005] C. Hopman and T. Alexander. The Orbital Statistics of Stellar Inspiral and Relaxation near a Massive Black Hole: Characterizing Gravitational Wave Sources. ApJ, 629:362–372, August 2005.

[Hopman and Alexander, 2006a] C. Hopman and T. Alexander. Resonant Relaxation near a Massive Black Hole: The Stellar Distribution and Gravitational Wave Sources. ApJ, 645:1152–1163, July 2006.

[Hopman and Alexander, 2006b] C. Hopman and T. Alexander. The Effect of Mass Segregation on Gravitational Wave Sources near Massive Black Holes. ApJ, 645:L133–L136, July 2006.

[Hopman, 2009] C. Hopman. Extreme mass ratio inspiral rates: dependence on the massive black hole mass. *Classical and Quantum Gravity*, 26(9):094028–+, May 2009.

[Hughes, 2009] S. A. Hughes. Gravitational Waves from Merging Compact Binaries. ARA&A, 47:107–157, September 2009.

[Hulse and Taylor, 1975] R. A. Hulse and J. H. Taylor. Discovery of a pulsar in a binary system. ApJ, 195:L51–L53, January 1975.

[Illarionov and Beloborodov, 2001] A. F. Illarionov and A. M. Beloborodov. Free-fall accretion and emitting caustics in wind-fed X-ray sources. MNRAS, 323:159–166, May 2001.

[Illarionov and Sunyaev, 1975] A. F. Illarionov and R. A. Sunyaev. Why the Number of Galactic X-ray Stars Is so Small? A&A, 39:185–+, February 1975.

[Imshennik *et al.*, 1967] V. S. Imshennik, D. K. Nadezhin, and V. S. Pinaev. Kinetic Equilibrium of β-Processes in Stellar Interiors. Soviet Ast., 10:970–+, June 1967.

[Ishii *et al.*, 1993] T. Ishii, T. Matsuda, E. Shima, M. Livio, U. Anzer, and G. Boerner. Numerical simulations of two-dimensional and three-dimensional wind accretion flows of an isothermal gas. ApJ, 404:706–716, February 1993.

[Ivanov and Papaloizou, 2007] P. B. Ivanov and J. C. B. Papaloizou. Orbital circularisation of white dwarfs and the formation of gravitational radiation sources in star clusters containing an intermediate mass black hole. A&A, 476:121–135, December 2007.

[Ivanov, 2002] P. B. Ivanov. On the formation rate of close binaries consisting of a super-massive black hole and a white dwarf. MNRAS, 336:373–381, October 2002.

[Kato *et al.*, 2008] S. Kato, J. Fukue, and S. Mineshige. *Black-Hole Accretion Disks — Towards a New Paradigm —*. March 2008.

[Kato, 2001] S. Kato. Basic Properties of Thin-Disk Oscillations. PASJ, 53:1–24, February 2001.

[Kippenhahn and Weigert, A. , 1990] R. Kippenhahn and Weigert, A. . *Stellar structure and evolution*. 1990.

[Klebesadel *et al.*, 1973] R. W. Klebesadel, I. B. Strong, and R. A. Olson. Observations of Gamma-Ray Bursts of Cosmic Origin. ApJ, 182:L85+, June 1973.

[Kobayashi *et al.*, 2004] S. Kobayashi, P. Laguna, E. S. Phinney, and P. Mészáros. Gravitational Waves and X-Ray Signals from Stellar Disruption by a Massive Black Hole. ApJ, 615:855–865, November 2004.

[Kocsis *et al.*, 2007] B. Kocsis, Z. Haiman, K. Menou, and Z. Frei. Premerger localization of gravitational-wave standard sirens with LISA: Harmonic mode decomposition. Phys. Rev. D, 76(2):022003–+, July 2007.

[Kocsis *et al.*, 2008] B. Kocsis, Z. Haiman, and K. Menou. Premerger Localization of Gravitational Wave Standard Sirens with LISA: Triggered Search for an Electromagnetic Counterpart. ApJ, 684:870–887, September 2008.

[Krolik, 1999] J. H. Krolik. *Active galactic nuclei : from the central black hole to the galactic environment*. 1999.

[Kuznetsov and Mikheev, 1997] A. V. Kuznetsov and N. V. Mikheev. Production of electron-positron pairs by a neutrino propagating in a magnetic field. *Physics of Atomic Nuclei*, 60:1865–1874, November 1997.

[Landau and Lifshitz, 1971] L. D. Landau and E. M. Lifshitz. *The classical theory of fields*. 1971.

[Lang and Hughes, 2008] R. N. Lang and S. A. Hughes. Localizing Coalescing Massive Black Hole Binaries with Gravitational Waves. ApJ, 677:1184–1200, April 2008.

[Lee and Ramirez-Ruiz, 2006] W. H. Lee and E. Ramirez-Ruiz. Accretion Modes in Collapsars: Prospects for Gamma-Ray Burst Production. ApJ, 641:961–971, April 2006.

[Liang and Thompson, 1980] E. P. T. Liang and K. A. Thompson. Transonic disk accretion onto black holes. ApJ, 240:271–274, August 1980.

[Lightman and Eardley, 1974] A. P. Lightman and D. M. Eardley. Black Holes in Binary Systems: Instability of Disk Accretion. ApJ, 187:L1+, January 1974.

[Lithwick and Sari, 2001] Y. Lithwick and R. Sari. Lower Limits on Lorentz Factors in Gamma-Ray Bursts. ApJ, 555:540–545, July 2001.

[Livio *et al.*, 1991] M. Livio, N. Soker, T. Matsuda, and U. Anzer. On the 'flip-flop' instability of Bondi-Hoyle accretion flows. MNRAS, 253:633–636, December 1991.

[Manmoto *et al.*, 1997] T. Manmoto, S. Mineshige, and M. Kusunose. Spectrum of Optically Thin Advection-dominated Accretion Flow around a Black Hole: Application to Sagittarius A *. ApJ, 489:791–+, November 1997.

[Martel, 2004] K. Martel. Gravitational waveforms from a point particle orbiting a Schwarzschild black hole. Phys. Rev. D, 69(4):044025–+, February 2004.

[McKinney and Blandford, 2009] J. C. McKinney and R. D. Blandford. Stability of relativistic jets from rotating, accreting black holes via fully three-dimensional magnetohydrodynamic simulations. MNRAS, 394:L126–L130, March 2009.

[Meegan *et al.*, 1996] C. A. Meegan, G. N. Pendleton, M. S. Briggs, C. Kouveliotou, T. M. Koshut, J. P. Lestrade, W. S. Paciesas, M. L. McCollough, J. J. Brainerd, J. M. Horack, J. Hakkila, W. Henze, R. D. Preece, R. S. Mallozzi, and G. J. Fishman. The Third BATSE Gamma-Ray Burst Catalog. ApJS, 106:65–+, September 1996.

[Menou *et al.*, 2008] K. Menou, Z. Haiman, and B. Kocsis. Cosmological physics with black holes (and possibly white dwarfs). New A Rev., 51:884–890, May 2008.

[Mészáros, 2006] P. Mészáros. Gamma-ray bursts. *Reports on Progress in Physics*, 69:2259–2321, August 2006.

[Metzger *et al.*, 1997] M. R. Metzger, S. G. Djorgovski, S. R. Kulkarni, C. C. Steidel, K. L. Adelberger, D. A. Frail, E. Costa, and F. Frontera. Spectral constraints on the redshift of the optical counterpart to the γ-ray burst of 8 May 1997. Nature, 387:878–880, June 1997.

[Metzger *et al.*, 2011] B. D. Metzger, D. Giannios, T. A. Thompson, N. Bucciantini, and E. Quataert. The protomagnetar model for gamma-ray bursts. MNRAS, 413:2031–2056, May 2011.

[Middleditch and Priedhorsky, 1986] J. Middleditch and W. C. Priedhorsky. Discovery of rapid quasi-periodic oscillations in Scorpius X-1. ApJ, 306:230–237, July 1986.

[Miller *et al.*, 2005] M. C. Miller, M. Freitag, D. P. Hamilton, and V. M. Lauburg. Binary Encounters with Supermassive Black Holes: Zero-Eccentricity LISA Events. ApJ, 631:L117–L120, October 2005.

[Mirabel and Rodríguez, 1999] I. F. Mirabel and L. F. Rodríguez. Sources of Relativistic Jets in the Galaxy. ARA&A, 37:409–443, 1999.

[Misner *et al.*, 1973] C. W. Misner, K. S. Thorne, and J. A. Wheeler. *Gravitation*. 1973.

[Nakamura *et al.*, 1996] K. E. Nakamura, R. Matsumoto, M. Kusunose, and S. Kato. Global Structures of Advection-Dominated Two-Temperature Accretion Disks. PASJ, 48:761–769, October 1996.

[Nakamura *et al.*, 1997] K. E. Nakamura, M. Kusunose, R. Matsumoto, and S. Kato. Optically Thin, Advection-Dominated Two-Temperature Disks. PASJ, 49:503–512, August 1997.

[Narayan and McClintock, 2008] R. Narayan and J. E. McClintock. Advection-dominated accretion and the black hole event horizon. New A Rev., 51:733–751, May 2008.

[Narayan and Yi, 1994] R. Narayan and I. Yi. Advection-dominated accretion: A self-similar solution. ApJ, 428:L13–L16, June 1994.

[Narayan and Yi, 1995] R. Narayan and I. Yi. Advection-dominated Accretion: Underfed Black Holes and Neutron Stars. ApJ, 452:710–+, October 1995.

[Narayan *et al.*, 1992] R. Narayan, B. Paczynski, and T. Piran. Gamma-ray bursts as the death throes of massive binary stars. ApJ, 395:L83–L86, August 1992.

[Narayan *et al.*, 1995] R. Narayan, I. Yi, and R. Mahadevan. Explaining the spectrum of Sagittarius A* with a model of an accreting black hole. Nature, 374:623–625, April 1995.

[Narayan *et al.*, 1996] R. Narayan, J. E. McClintock, and I. Yi. A New Model for Black Hole Soft X-Ray Transients in Quiescence. ApJ, 457:821–+, February 1996.

[Narayan *et al.*, 1998] R. Narayan, R. Mahadevan, and E. Quataert. Advection-dominated accretion around black holess. In M. A. Abramowicz, G. Bjornsson, & J. E. Pringle, editor, *Theory of Black Hole Accretion Disks*, pages 148–+, 1998.

[Narayan *et al.*, 2001] R. Narayan, T. Piran, and P. Kumar. Accretion Models of Gamma-Ray Bursts. ApJ, 557:949–957, August 2001.

[Page and Thorne, 1974] D. N. Page and K. S. Thorne. Disk-Accretion onto a Black Hole. Time-Averaged Structure of Accretion Disk. ApJ, 191:499–506, July 1974.

[Panaitescu, 2006] A. Panaitescu. Phases of Swift X-ray afterglows. *Nuovo Cimento B Serie*, 121:1099–1104, October 2006.

[Peebles, 1993] P. J. E. Peebles. *Principles of Physical Cosmology*. 1993.

[Peters and Mathews, 1963] P. C. Peters and J. Mathews. Gravitational Radiation from Point Masses in a Keplerian Orbit. *Physical Review*, 131:435–440, July 1963.

[Peters, 1964] P. C. Peters. Gravitational Radiation and the Motion of Two Point Masses. *Physical Review*, 136:1224–1232, November 1964.

[Phinney, 2009] E. S. Phinney. Finding and Using Electromagnetic Counterparts of Gravitational Wave Sources. In *astro2010: The Astronomy and Astrophysics Decadal Survey*, volume 2010 of *Astronomy*, pages 235–+, 2009.

[Piran, 1978] T. Piran. The role of viscosity and cooling mechanisms in the stability of accretion disks. ApJ, 221:652–660, April 1978.

[Piran, 1999] T. Piran. Gamma-ray bursts and the fireball model. Phys. Rep., 314:575–667, June 1999.

[Piran, 2004] T. Piran. The physics of gamma-ray bursts. *Reviews of Modern Physics*, 76:1143–1210, October 2004.

[Popham *et al.*, 1999] R. Popham, S. E. Woosley, and C. Fryer. Hyperaccreting Black Holes and Gamma-Ray Bursts. ApJ, 518:356–374, June 1999.

[Pringle, 1976] J. E. Pringle. Thermal instabilities in accretion discs. MNRAS, 177:65–71, October 1976.

[Pringle, 1981] J. E. Pringle. Accretion discs in astrophysics. ARA&A, 19:137–162, 1981.

[Rathore *et al.*, 2005] Y. Rathore, R. D. Blandford, and A. E. Broderick. Resonant excitation of white dwarf oscillations in compact object binaries - I. The no back reaction approximation. MNRAS, 357:834–846, March 2005.

[Rees and Meszaros, 1994] M. J. Rees and P. Meszaros. Unsteady outflow models for cosmological gamma-ray bursts. ApJ, 430:L93–L96, August 1994.

[Ritter, 1988] H. Ritter. Turning on and off mass transfer in cataclysmic binaries. A&A, 202:93–100, August 1988.

[Rosswog *et al.*, 2009] S. Rosswog, E. Ramirez-Ruiz, and W. R. Hix. Tidal Disruption and Ignition of White Dwarfs by Moderately Massive Black Holes. ApJ, 695:404–419, April 2009.

[Sari *et al.*, 1999] R. Sari, T. Piran, and J. P. Halpern. Jets in Gamma-Ray Bursts. ApJ, 519:L17–L20, July 1999.

[Sathyaprakash and Schutz, 2009] B. S. Sathyaprakash and B. F. Schutz. Physics, Astrophysics and Cosmology with Gravitational Waves. *Living Reviews in Relativity*, 12:2–+, March 2009.

[Sepinsky *et al.*, 2007] J. F. Sepinsky, B. Willems, and V. Kalogera. Equipotential Surfaces and Lagrangian Points in Nonsynchronous, Eccentric Binary and Planetary Systems. ApJ, 660:1624–1635, May 2007.

[Sesana *et al.*, 2008] A. Sesana, A. Vecchio, M. Eracleous, and S. Sigurdsson. Observing white dwarfs orbiting massive black holes in the gravitational wave and electro-magnetic window. MNRAS, 391:718–726, December 2008.

[Shafee *et al.*, 2008] R. Shafee, J. C. McKinney, R. Narayan, A. Tchekhovskoy, C. F. Gammie, and J. E. McClintock. Three-Dimensional Simulations of Magnetized Thin Accretion Disks around Black Holes: Stress in the Plunging Region. ApJ, 687:L25–L28, November 2008.

[Shakura and Sunyaev, 1973] N. I. Shakura and R. A. Sunyaev. Black holes in binary systems. Observational appearance. A&A, 24:337–355, 1973.

[Shakura and Sunyaev, 1976] N. I. Shakura and R. A. Sunyaev. A theory of the instability of disk accretion on to black holes and the variability of binary X-ray sources, galactic nuclei and quasars. MNRAS, 175:613–632, June 1976.

[Shapiro and Lightman, 1976] S. L. Shapiro and A. P. Lightman. Black holes in X-ray binaries - Marginal existence and rotation reversals of accretion disks. ApJ, 204:555–560, March 1976.

[Shapiro *et al.*, 1976] S. L. Shapiro, A. P. Lightman, and D. M. Eardley. A two-temperature accretion disk model for Cygnus X-1 - Structure and spectrum. ApJ, 204:187–199, February 1976.

[Shimura and Takahara, 1993] T. Shimura and F. Takahara. Vertical Structure and Emission Spectrum of an Accretion Disk around a Massive Black Hole. ApJ, 419:78–+, December 1993.

[Sigurdsson and Rees, 1997] S. Sigurdsson and M. J. Rees. Capture of stellar mass compact objects by massive black holes in galactic cusps. MNRAS, 284:318–326, January 1997.

[Spruit *et al.*, 2001] H. C. Spruit, F. Daigne, and G. Drenkhahn. Large scale magnetic fields and their dissipation in GRB fireballs. A&A, 369:694–705, April 2001.

[Taylor and Weisberg, 1989] J. H. Taylor and J. M. Weisberg. Further experimental tests of relativistic gravity using the binary pulsar PSR 1913 + 16. ApJ, 345:434–450, October 1989.

[Thompson, 1994] C. Thompson. A Model of Gamma-Ray Bursts. MNRAS, 270:480–+, October 1994.

[Thorne and Price, 1975] K. S. Thorne and R. H. Price. Cygnus X-1 - an interpretation of the spectrum and its variability. ApJ, 195:L101–L105, February 1975.

[van der Klis *et al.*, 1985] M. van der Klis, F. Jansen, J. van Paradijs, W. H. G. Lewin, E. P. J. van den Heuvel, J. E. Trumper, and M. Szatjno. Intensity-dependent quasi-periodic oscillations in the X-ray flux of GX5 - 1. Nature, 316:225–230, July 1985.

[van der Klis *et al.*, 1996] M. van der Klis, J. H. Swank, W. Zhang, K. Jahoda, E. H. Morgan, W. H. G. Lewin, B. Vaughan, and J. van Paradijs. Discovery of Sub-

millisecond Quasi-periodic Oscillations in the X-Ray Flux of Scorpius X-1. ApJ, 469:L1+, September 1996.

[Weisberg *et al.*, 2010] J. M. Weisberg, D. J. Nice, and J. H. Taylor. Timing Measurements of the Relativistic Binary Pulsar PSR B1913+16. ApJ, 722:1030–1034, October 2010.

[Woosley and Heger, 2006] S. E. Woosley and A. Heger. The Progenitor Stars of Gamma-Ray Bursts. ApJ, 637:914–921, February 2006.

[Woosley, 1993] S. E. Woosley. Gamma-ray bursts from stellar mass accretion disks around black holes. ApJ, 405:273–277, March 1993.

[Zalamea and Beloborodov, 2009] I. Zalamea and A. M. Beloborodov. Mini-discs around spinning black holes. MNRAS, 398:2005–2011, October 2009.

[Zalamea and Beloborodov, 2011] I. Zalamea and A. M. Beloborodov. Neutrino heating near hyper-accreting black holes. MNRAS, 410:2302–2308, February 2011.

[Zalamea *et al.*, 2010] I. Zalamea, K. Menou, and A. M. Beloborodov. White dwarfs stripped by massive black holes: sources of coincident gravitational and electromagnetic radiation. MNRAS, 409:L25–L29, November 2010.

Appendix A

Kerr metric and some useful expressions

A.1 Kerr metric

For Kerr geometry we have the following metric:

$$\begin{aligned} g_{ij}dx^i dx^j &= -(1-\frac{2GMr}{\rho^2})dt^2 - \frac{2GMar}{\rho^2}\sin^2(\theta)(dtd\phi + d\phi dt) + \frac{\rho^2}{\Delta}dr^2 + \\ &\quad \rho^2 d\theta^2 + \frac{\sin^2(\theta)}{\rho^2}[(r^2+a^2)^2 - a^2\Delta\sin^2(\theta)]d\phi^2, \end{aligned} \tag{A.1}$$

where

$$\rho^2 = r^2 + a^2\cos^2\theta, \tag{A.2}$$

$$\Delta = r^2 - 2GMr + a^2. \tag{A.3}$$

The inverse of Kerr metric is

$$\begin{aligned} g^{ij}\partial_i\partial_j &= -\frac{(r^2+a^2)^2 - a^2\sin^2\theta}{\Delta\rho^2}(\partial_t)^2 - \frac{2GMar}{\Delta\rho^2}(\partial_t\partial_\phi + \partial_\phi\partial_t) + \\ &\quad \frac{\Delta}{\rho^2}(\partial_r)^2 + \frac{1}{\rho^2}(\partial_\theta)^2 + \frac{\rho^2 - 2GMr}{\Delta\rho^2\sin^2\theta}(\partial_\phi)^2. \end{aligned} \tag{A.4}$$

A.2 Radial equation of motion for the mini-disc

Here we calculate the right-hand side of eq 2.32,

$$\frac{\partial g_{kl}}{\partial x^i}u^k u^l = \frac{\partial g_{tt}}{\partial r}(u^t)^2 + \frac{\partial g_{rr}}{\partial r}(u^r)^2 + \frac{\partial g_{\phi\phi}}{\partial r}(u^\phi)^2 + 2\frac{\partial g_{t\phi}}{\partial r}u^t u^\phi. \tag{A.5}$$

It is desirable to work with the "constant" of motion u_ϕ instead of u^ϕ, we can use

$$u_\phi = g_{t\phi}u^t + g_{\phi\phi}u^\phi \quad \Rightarrow \quad u^\phi = \frac{u_\phi - g_{t\phi}u^t}{g_{\phi\phi}}, \tag{A.6}$$

replacing this into eq A.5 we have

$$\begin{aligned}\frac{\partial g_{kl}}{\partial x^i}u^k u^l &= \Big(\partial_r g_{tt} + \frac{g_{t\phi}^2}{g_\phi^2}\partial_r g_{\phi\phi} - 2\frac{g_{t\phi}}{g_\phi}\partial_r g_{t\phi}\Big)(u^t)^2 + \partial_r g_{rr}(u^r)^2 + \\ &\quad \frac{\partial_r g_{\phi\phi}}{g_{\phi\phi}^2}u_\phi^2 + 2\Big(\frac{\partial_r g_{t\phi}}{g_{\phi\phi}} - \frac{g_{t\phi}}{g_{\phi\phi}^2}\partial_r g_{\phi\phi}\Big)u_\phi u^t.\end{aligned} \tag{A.7}$$

u^t is not independent of the other components of the velocity, since $u^\alpha u_\alpha = -1$ we have

$$0 = \Big(g_{tt} - \frac{g_{t\phi}^2}{g_{\phi\phi}}\Big)(u^t)^2 + g_{rr}(u^r)^2 + \frac{1}{g_{\phi\phi}}u_\phi^2 + 1. \tag{A.8}$$

Replacing u^t from eq.A.8 into eq.A.7 we get an equation of the form

$$\frac{\partial g_{kl}}{\partial r}u^k u^l = A + B(u^r)^2 + Cu_\phi^2 + Du_\phi u^t, \tag{A.9}$$

where A, B, C and D are functions of r only and u^t is supposed to be expressed in term of u^r and u_ϕ. The coefficients are

$$A = \frac{g_{\phi\phi}}{g_{t\phi}^2 - g_{tt}g_\phi}\Big(\partial_r g_{tt} + \frac{g_{t\phi}^2}{g_\phi^2}\partial_r g_{\phi\phi} - 2\frac{g_{t\phi}}{g_\phi}\partial_r g_{t\phi}\Big), \tag{A.10}$$

$$B = \partial_r g_{rr} + \frac{g_{\phi\phi}g_{rr}}{g_{t\phi}^2 - g_{tt}g_\phi}\Big(\partial_r g_{tt} + \frac{g_{t\phi}^2}{g_\phi^2}\partial_r g_{\phi\phi} - 2\frac{g_{t\phi}}{g_\phi}\partial_r g_{t\phi}\Big) = \partial_r g_{rr} + g_{rr}A, \tag{A.11}$$

$$C = \frac{\partial_r g_{\phi\phi}}{g_{\phi\phi}^2} + \frac{1}{g_{t\phi}^2 - g_{tt}g_\phi}\Big(\partial_r g_{tt} + \frac{g_{t\phi}^2}{g_\phi^2}\partial_r g_{\phi\phi} - 2\frac{g_{t\phi}}{g_\phi}\partial_r g_{t\phi}\Big) = \frac{\partial_r g_{\phi\phi}}{g_{\phi\phi}^2} + \frac{A}{g_{\phi\phi}}, \tag{A.12}$$

$$D = 2\frac{\partial_r g_{t\phi}}{g_{\phi\phi}} - 2\frac{g_{t\phi}}{g_{\phi\phi}^2}\partial_r g_{\phi\phi}. \tag{A.13}$$

To calculate the previous coefficients we have the following identities satisfied on the equatorial plane,

$$g_{t\phi}^2 - g_{tt}g_{\phi} = r(r - r_g) + a^2 \tag{A.14}$$

$$\partial_r g_{tt} = -\frac{r_g}{r^2} \tag{A.15}$$

$$\frac{g_{t\phi}^2}{g_{\phi}^2}\partial_r g_{\phi\phi} = -\frac{r_g^2 a^2(r_g a^2 - 2r^3)}{r^2(r^3 + a^2(r + r_g))^2} \tag{A.16}$$

$$\frac{g_{t\phi}}{g_{\phi}}\partial_r g_{t\phi} = -\frac{r_g^2 a^2}{r^2(r^3 + a^2(r + r_g))} \tag{A.17}$$

The coefficients A, B, C and D simplify to

$$A = -\frac{r_g(r^4 + a^4 + 2a^2 r(r - r_g))}{r(a^2 + r(r - r_g))(r^3 + a^2(r + r_g))}, \tag{A.18}$$

$$B - 2\partial_r g_{rr} = -\frac{a^2 r(2r - 3r_g)}{(a^2 + r(r - r_g))(r^3 + a^2(r + r_g))}, \tag{A.19}$$

$$C = -\frac{r^4(2r - 3r_g) - 2a^4 r_g + a^2 r(2r^2 - 3r_g r + 3r_g^2)}{(a^2 + r(r - r_g))(r^3 + a^2(r + r_g))^2}, \tag{A.20}$$

$$D = -\frac{2ar_g(3r^2 + a^2)}{(r^3 + a^2(r + r_g))^2} \tag{A.21}$$

Appendix B

Calculation of the escaping luminosity

B.1 Angular distribution of emission in the local ZAMO frame

Consider an infinitesimal element of the disc, a ring of radius r and thickness δr. It produces luminosity

$$\delta L = \frac{dL}{dr}\,\delta r = \frac{d}{dr}\left[(c^2 + cu_t)\dot{M}\right]\,\delta r. \tag{B.1}$$

The ring emits photons in all directions, which will be parameterized by unit 3D vector $\bar{\mathbf{\Omega}}$ in the local frame of ZAMO (zero-angular-momentum observer at fixed r, see e.g. Misner et al. 1973). Then δL may be written as

$$\delta L = \int_{4\pi} \frac{d(\delta L)}{d\bar{\Omega}}\, d\bar{\Omega} = \int \frac{d\bar{t}}{dt}\frac{E}{\bar{E}}\frac{d(\delta \bar{L})}{d\bar{\Omega}}\, d\bar{\Omega}. \tag{B.2}$$

Here $\delta\bar{L}$ is the luminosity of the ring measured by ZAMO and $\bar{t}$ is the proper time of ZAMO. $E/\bar{E}$ is the ratio of photon energy measured at infinity, $E = -cv_t$, and measured by ZAMO, $\bar{E} = -c\bar{v}_t = c\bar{v}^t$; this ratio depends on the emission direction $\bar{\mathbf{\Omega}}$. It is found from the Lorentz transformation of the photon 4-velocity from the

coordinate basis to the (orthonormal) ZAMO basis,

$$\begin{pmatrix} \bar{v}^t \\ \bar{v}^\phi \end{pmatrix} = \begin{pmatrix} \sqrt{-\tilde{g}_{tt}} & 0 \\ g_{t\phi}/\sqrt{g_{\phi\phi}} & \sqrt{g_{\phi\phi}} \end{pmatrix} \begin{pmatrix} v^t \\ v^\phi \end{pmatrix}, \tag{B.3}$$

$$\bar{v}^r = \sqrt{g_{rr}} v^r, \qquad \bar{v}^\theta = \sqrt{g_{\theta\theta}} v^\theta, \tag{B.4}$$

where $\tilde{g}_{tt} = g_{tt} - g_{t\phi}^2/g_{\phi\phi}$. Then one finds,

$$\frac{E}{\bar{E}} = \frac{v_t}{\bar{v}_t} = \sqrt{-\tilde{g}_{tt}} - \frac{g_{t\phi}}{\sqrt{g_{\phi\phi}}} \bar{\Omega}^\phi. \tag{B.5}$$

The ratio $d\bar{t}/dt$ appearing in equation (B.2) equals $(-\tilde{g}_{tt})^{1/2}$.

The angular distribution of luminosity measured by ZAMO, $d(\delta\bar{L})/d\bar{\Omega}$, is related to the angular distribution of luminosity in the rest frame of the accreting gas of the disc, $d(\delta L_c)/d\Omega_c$, by the Doppler transformation (see e.g. Rybicki & Lightman 1979),

$$\frac{d(\delta\bar{L})}{d\bar{\Omega}} = \frac{1}{\gamma^4(1-\beta\cdot\bar{\mathbf{\Omega}})^3} \frac{d(\delta L_c)}{d\Omega_c}, \tag{B.6}$$

where β is the disc velocity (in units of c) measured by ZAMO. We assume that emission is approximately isotropic in the gas frame, i.e. $d(\delta L_c)/d\Omega_c = \delta L_c/4\pi$. Substitution of equations (B.5) and (B.6) to equation (B.2) gives,

$$\delta L = \frac{\delta L_c}{4\pi} (-\tilde{g}_{tt})^{1/2} \int_{4\pi} \frac{[\sqrt{-\tilde{g}_{tt}} - (g_{t\phi}/\sqrt{g_{\phi\phi}})\bar{\Omega}^\phi]}{\gamma^4(1-\beta\cdot\bar{\mathbf{\Omega}})^3} \, d\bar{\Omega}. \tag{B.7}$$

The expression for escaping luminosity $\delta L_{\rm esc}$ is similar except that the integral is taken over the escape cone $S_{\rm esc}$ rather than 4π. Therefore, the escaping fraction is given by

$$f_{\rm esc} \equiv \frac{\delta L_{\rm esc}}{\delta L} = \left(\int_{4\pi} \frac{[\sqrt{-\tilde{g}_{tt}} - (g_{t\phi}/\sqrt{g_{\phi\phi}})\bar{\Omega}^\phi]}{\gamma^4(1-\beta\cdot\bar{\mathbf{\Omega}})^3} \, d\bar{\Omega} \right)^{-1} \times \int_{S_{\rm esc}} \frac{[\sqrt{-\tilde{g}_{tt}} - (g_{t\phi}/\sqrt{g_{\phi\phi}})\bar{\Omega}^\phi]}{\gamma^4(1-\beta\cdot\bar{\mathbf{\Omega}})^3} \, d\bar{\Omega}.$$

Evaluating the integral over 4π we obtain equation (2.40).

B.2 Escape cones

The photon direction in the ZAMO frame, $\bar{\mathbf{\Omega}}$, can be described by two angles α and φ,

$$\bar{\Omega}^r = \frac{\bar{v}^r}{\bar{v}^t} = \cos\alpha, \tag{B.8}$$

$$\bar{\Omega}^\theta = \frac{\bar{v}^\theta}{\bar{v}^t} = \sin\alpha\sin\varphi, \tag{B.9}$$

$$\bar{\Omega}^\phi = \frac{\bar{v}^\phi}{\bar{v}^t} = \sin\alpha\cos\varphi. \tag{B.10}$$

Using the relations between $\bar{v}^i$ and v^i (eqs. B.3 and B.4), we express $\bar{\mathbf{\Omega}}$ in terms of v^i,

$$\cos\alpha = \sqrt{-\frac{g_{rr}}{\tilde{g}_{tt}}}\frac{v^r}{v^t} = \frac{\sqrt{r^4 + a^2 r(r+r_g)}}{a^2 + r(r-r_g)}\frac{v^r}{v^t}, \tag{B.11}$$

$$\sin\alpha\sin\varphi = \sqrt{-\frac{g_{\theta\theta}}{\tilde{g}_{tt}}}\frac{v^\theta}{v^t} = \sqrt{\frac{r^4 + a^2 r(r+r_g)}{a^2 + r(r-r_g)}}\frac{v^\theta}{v^t}, \tag{B.12}$$

where all metric coefficients have been evaluated at the equatorial plane at the emission radius r.

The photon 4-velocity v^i is expressible in terms of four integrals of motion in Kerr metric: energy E, total angular momentum L, its projection L_z, and Carter integral Γ. Using these expressions (see e.g. Chandrasekar 1982) and choosing the affine parameter along the photon worldline so that $E = c^2$, we find v^r/v^t and v^θ/v^t as functions of r, Γ and L_z, and obtain

$$\begin{aligned}\cos^2\alpha &= \frac{r^4 + a^2 r(r+r_g)}{\left[r^4 + a^2 r(r+r_g) - r_g a L_z r\right]^2} \\ &\times \left[r^4 + r^2\left(\Gamma + a^2\right) + r r_g\left(a^2 - \Gamma - 2aL_z\right)\right. \\ &\left. + a^2\left(\Gamma + L_z^2\right)\right],\end{aligned} \tag{B.13}$$

$$\begin{aligned}\sin^2\alpha\,\sin^2\varphi &= -\left(\Gamma + L_z^2\right)\left(r^2 + a^2 - r_g r\right) \\ &\times \frac{\left[r^4 + a^2 r(r+r_g)\right]}{\left[r^4 + a^2 r(r+r_g) - r_g a L_z r\right]^2}.\end{aligned} \tag{B.14}$$

Equations (B.13) and (B.14) can be solved for L_z and Γ for given r, α and φ.

The fate of a photon is determined by the equation of radial motion for null geodesics (e.g. Chandrasekar 1982),

$$\left(r^2 + a^2\cos^2\theta\right)^2 (v^r)^2 = \left(r^2 + a^2 - r_g r\right)\left(\Gamma - a^2E^2\right) + \left(r^2 + a^2\right)^2 E^2 - 2r_g aEL_z r + a^2L_z^2, \tag{B.15}$$

where $E = c^2$ with our choice of affine parameter along photon worldline. The possible turning points $r_{\rm turn}$ are found from the condition $v^r = 0$. Let r_0 be the initial radial position of the photon. Two cases are possible: (i) $v(r_0) > 0$, the photon escapes if there are no $r_{\rm turn} > r_0$. (ii) $v(r_0) < 0$, the photon escapes if there is at least one turning point such that $r_h < r_{\rm turn} < r_0$ and no $r_{\rm turn} > r_0$.

For any given direction $\bar{\mathbf{\Omega}}$, we find L_z and Γ from equations (B.13) and (B.14), then determine the roots $r_{\rm turn}$ of equation $v^r(r) = 0$ and check the escape conditions. All escaping directions form the "cone" $S_{\rm esc}$ on the sky of ZAMO, which is found numerically. Figure B.1 shows the escape cones for five emission radii r_0 and four values of $a_\star$.

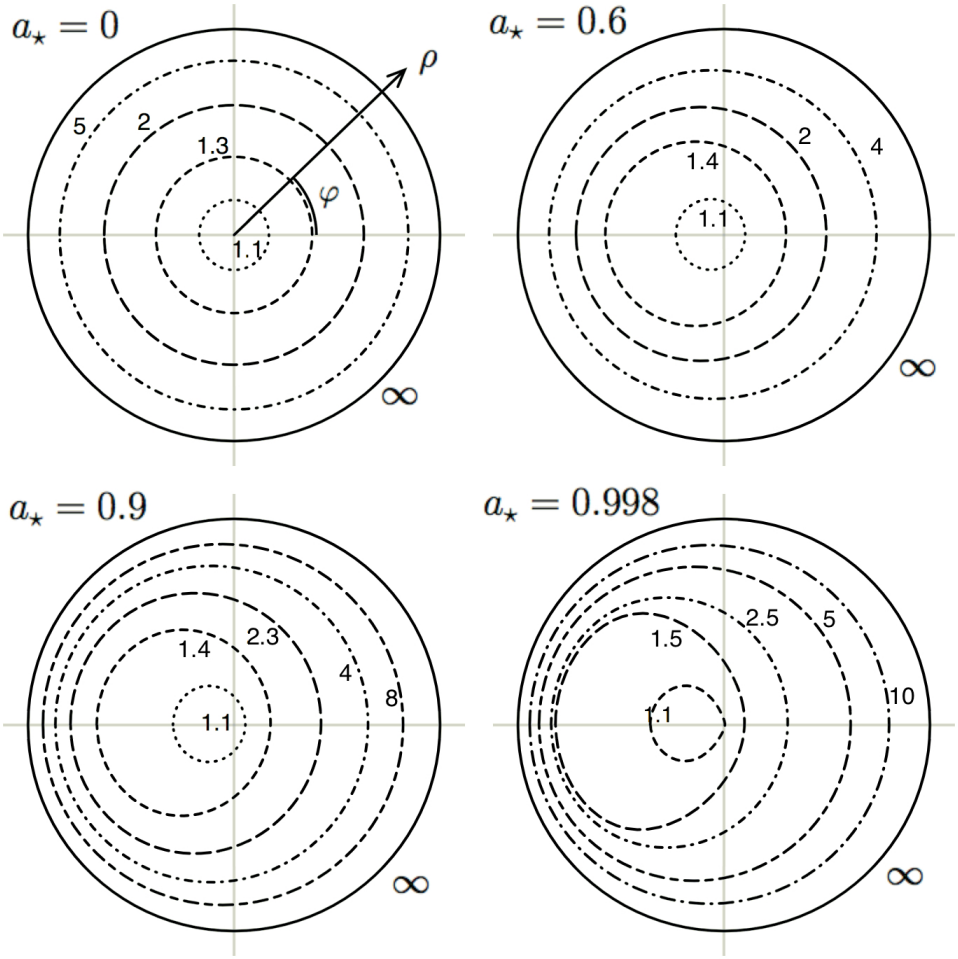

Figure B.1: Escape cones $S_{\rm esc}$ on the ZAMO sky. The photon direction $\bar{\mathbf{\Omega}}$ is specified by two angles α and φ (eqs. B.8-B.10). The figure uses polar coordinates (ρ, ϕ) with $\rho = \alpha/\pi$ to represent all possible photon directions. The origin of the diagram $\rho = 0$ corresponds to the radial direction away from the black hole (such photons always escape) and the unit circle $\rho = 1$ (thick black curve) corresponds to the radial direction into the black hole (such photons are captured). The colour curves show the boundary of the escape cone for five emission radii; the emission radius is indicated next to the curves, in units of the horizon radius r_h. The figure presents four such diagrams calculated for black holes with spin parameter $a_\star = 0$, 0.6, 0.9, and 0.998.

Appendix C

Structure of a cold and non-rotating white dwarf

In chapter 4 we consider spherically symmetric (non-rotating) cold ($kT << E_F$, thermal energy much smaller than the electron's Fermi energy) white dwarfs of uniform chemical composition supported by electron's degeneracy pressure. The equation of state is given by (e.g. [Kippenhahn and Weigert, A. , 1990]):

$$P = \frac{\pi m_e^4 c^5}{3h^3} f(x) \qquad , \qquad \rho = m_{\rm u}\mu_e \frac{8\pi m_e^3 c^3}{3h^3} x^3 \tag{C.1}$$
$$\text{where} \quad f(x) = x(2x^2-3)(1+x^2)^{1/2} + 3\ln\left(x+(1+x^2)^{1/2}\right),$$

and $x = p_F/m_e c$ is the "normalized" Fermi momentum. The hydrostatic equilibrium equation reads

$$\frac{C_1}{C_2}\frac{1}{r^2}\frac{d}{dr}\left(\frac{r^2}{x^3}\frac{df(x)}{dr}\right) = -4\pi G C_1 x^3, \tag{C.2}$$

where $C_1 = \pi m_e^4 c^5/(3h^3)$ and $C_2 = 8\pi\mu_e m_{\rm u} m_e^3 c^3/(3h^3)$. Changing variables as $\varphi = \sqrt{1+x^2}/z_c$, $\xi = r/\alpha$, with z_c a constant such that $\varphi(0) = 1$ and $\alpha = \sqrt{(2C_1/\pi G)}/(z_c C_2)$, the hydrostatic equation reduces to

$$\frac{d^2\varphi}{d\xi^2} + \frac{2}{\xi}\frac{d\varphi}{d\xi} + \left(\varphi^2 - \frac{1}{z_c^2}\right)^{3/2} = 0. \tag{C.3}$$

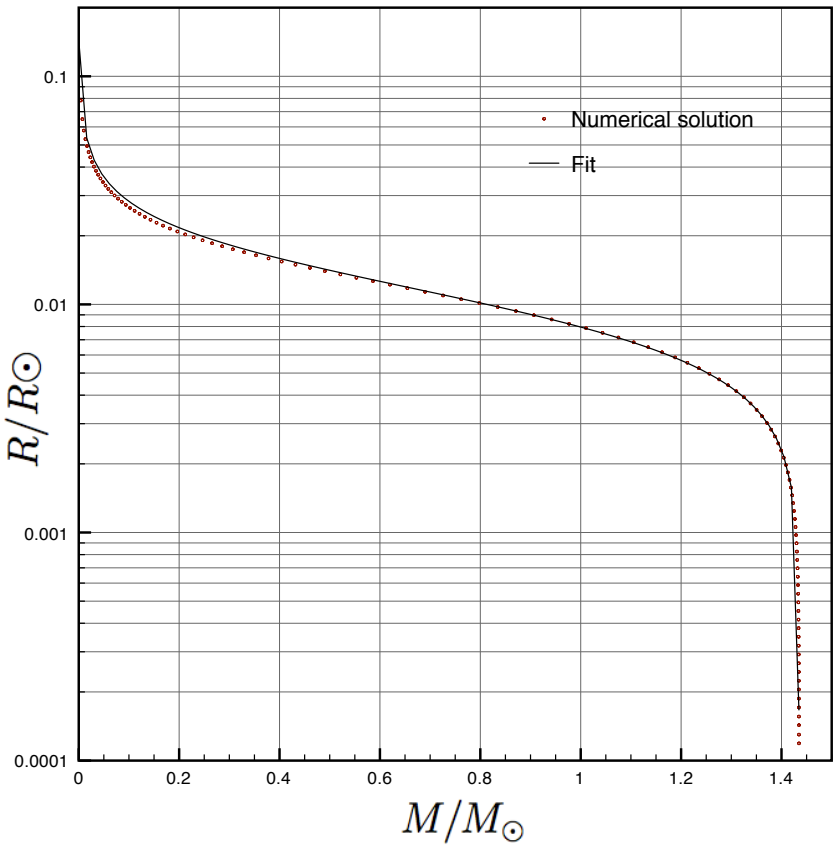

Figure C.1: Mass-radius relationship for cold white dwarf.

At $\xi = 0$ we must have $\varphi = 1$ and $\varphi' = 0$ (this guarantees a continuos first derivative of ρ at the center).

The numerical constants are

$$C_1 = 6.014 \times 10^{22} \text{ erg cm}^{-3}, \tag{C.4}$$

$$C_2 = \frac{\mu_e}{2} 1.96 \times 10^6 \text{g cm}^{-3}, \tag{C.5}$$

$$\alpha = \frac{2}{z_c \mu_e} 3.866 \times 10^8 \text{ cm}. \tag{C.6}$$

For a cold white dwarf the function

$$R = R_* \left(\frac{M_c}{M}\right)^{1/3} \left(1 - \frac{M}{M_c}\right)^{\beta}, \tag{C.7}$$

where $R_* = 0.01356 R_\odot$, $M_c = 1.4384 M_\odot$ and $\beta = 0.477$, is a good fit for the mass-radius relation.